Title
Scalable Manufacturing of Superhydrophobic Micro- and Nanostructured Condensation Accelerating and Droplet Shedding Surfaces for Air Conditioning Performance Enhancement

Author
Kadala, Kristyn

Publication Date
2019

Peer reviewed|Thesis/dissertation

Scalable Manufacturing of Superhydrophobic Micro- and Nanostructured Condensation Accelerating and Droplet Shedding Surfaces for Air Conditioning Performance Enhancement

By

Kristyn Kadala

A dissertation submitted in partial satisfaction of the

requirements for the degree of

Doctor of Philosophy

in

Engineering - Mechanical Engineering

in the

Graduate Division

of the

University of California, Berkeley

Committee in charge:

Professor Hayden K. Taylor, Chair
Professor Ömer Savaş
Professor Robert Leachman

Fall 2019

Scalable Manufacturing of Superhydrophobic Micro- and Nanostructured Condensation Accelerating and Droplet Shedding Surfaces for Air Conditioning Performance Enhancement

Abstract

Scalable Manufacturing of Superhydrophobic Micro- and Nanostructured Condensation Accelerating and Droplet Shedding Surfaces for Air Conditioning Performance Enhancement

By

Kristyn Kadala

Doctor of Philosophy in Engineering - Mechanical Engineering

University of California, Berkeley

Professor Hayden K. Taylor, Chair

One solution currently being explored for reducing the condensation effects of water inside the evaporator coil of an air conditioning system is the use of textured surface morphologies on the evaporator fins that may enable water droplets to both condense and shed more quickly. While multiple pattern scales and geometries have been characterized on metal substrates, including posts, pillars, post arrays, reentrant structures, micro/nano hierarchical patterns, and microchannels, there is a dearth of research associated with microdome patterns, the significance being that nature's most famous superhydrophobic, water-shedding surface, the lotus leaf, utilizes these features. Here, aluminum surfaces have been fabricated with varying micropillar and microdome structures and a hydrothermally grown nanoporous layer of zinc oxide to create a hierarchical morphology that is reminiscent of the lotus leaf geometry. Micropillar and microdome array structures with comparable feature sizes and areal densities were fabricated, and their static and dynamic water contact angles were characterized in order to understand the influence of microstructural geometry on water-shedding performance. These hierarchical surfaces were further characterized in dynamic condensing conditions using a custom-designed wind tunnel setup to simulate an air conditioning inlet environment. Video footage was recorded, and an image analysis algorithm was developed and applied in order to compare surface performance. The entire zinc oxide nanostructure synthesis process was then scaled and applied to a full-scale cooling coil for later evaluation in a simulated building testbed. The results of all surface characterization methods and condensation tests, the wind tunnel test bed design, the image analysis algorithm development, and the scaling process are reported.

I dedicate this work to my mum and dad!

Table of Contents

List of Figures

List of Tables

Acknowledgements

I'd like to thank my advisor, Professor Hayden Taylor, for his unwavering support and guidance through the graduate school process. I have had the pleasure and privilege of diving into a new field of study and embracing the research opportunities and potential. In addition, I also greatly appreciated the support and funding from Singapore-Berkeley Building Efficiency and Sustainability in the Tropics (SinBerBEST). I would also like to thank Professor Savaş for his wonderful classes, support for my Master's degree, and continued support for my dissertation. I wish him the best and hope to remain in touch as I continue professionally. I would also like to thank Professor Zohdi, Professor Lieu, and Professor Leachman all for helping me move forward with my degree as a part of the committee process. And, of course, Yawo, and the administrative office have been a tremendous help throughout my time here.

Many of these experiments would not have been possible without the help and support of Paul Lum in the BNC, the excellent ME Machine Shop staff, the EH&S staff, and my lab partner, Kyle Chung. I'd especially like to thank Paul for being a treasure trove of knowledge and project strategy suggestions and for his sense of fun. Not many labs would let you implode a 55-gallon drum!

I'd like to thank my parents and friends as well for always supporting me and reminding me to stay focused and stay positive. Grad school has had its fair share of ups and downs, reminding me of the same mental journey needed to finish a 100-mile foot race. At some points, the journey is shared with others, and at other points, the journey must be run alone. But for those shared moments, I'm very lucky to have had the support and positivity of John Madura, Mitch Westwood, and Garrett Cullen. In different ways, they've each reminded me to not be afraid to pursue my passions and enjoy every step of the journey toward them. And most importantly, much credit must go to Caffè Strada – the real source of my daily fuel and energy in this 5.5-year ordeal.

1 Chapter: Motivation and Introduction

1.1 Problem Statement: How can we improve air conditioner efficiency?

As the use of air conditioning steadily rises on a global scale, there is an urgent need to improve technologies for energy-efficient dehumidification and cooling of air. In the near future, it has been estimated that over a billion people in India, China, Brazil, Africa and other low-income and developing areas will be able to purchase their own air conditioning systems. China doubled the number of air conditioners sold between 2008 to 2013 to the extent that 64 million units were sold in 2013 alone. In humid climates, and especially in the tropics, the popularity of air conditioning systems in new and existing infrastructure is creating a strain on already limited energy resources. Already 10% of global energy usage is for air conditioning and cooling. As global temperatures continue to rise, the number of days per year that a cooling system is used increases, placing strain on electricity consumption[1–5]. Since an air conditioning user's comfort relies on removing both heat and humidity from the air, the condensation of water vapor inside an air conditioning system's heat exchanger can reduce the efficiency of heat transfer and require more energy input to cool the same amount of air due to the combined sensible and latent cooling loads. This need for further energy thus continues to push up electricity consumption and corresponding CO_2 emissions to the extent that 30% of energy consumption in US commercial and residential buildings can be attributed to HVAC systems[6].

1.2 Background

Most air conditioner and refrigeration systems operate using a cycling evaporator and condenser setup where incoming air is cooled after passing over a set of cooling coils, and refrigerant is recondensed and circulated to cool additional incoming air. An internal fan forces air to travel into the evaporator coil, the primary site of heat transfer in an air conditioning system, where the air travels through a set of tightly spaced aluminum fins and orthogonally positioned copper tubing containing refrigerant. As the air passes over the coils, the refrigerant absorbs heat from the air and vaporizes while the air itself is cooled. Water vapor in the air condenses out of the air as the temperature decreases and forms droplets or films on the aluminum fins. The refrigerant is cycled into a condenser in which excess heat is removed and expelled externally so that the liquid refrigerant can be passed through the evaporator cooling coils once again. The cooled air, depending on the implementation, can pass through building ducts in the case of central air buildings, can be expelled into a room in the case of window units, or can be pumped into a refrigerator in the case of refrigeration systems. The condensed water often is collected in a drip pan once it has shed gravitationally from the fins. This, however, is vastly inefficient for heat transfer to take place. The condensed water not only acts as

a thermal insulator on the fins but also can become a site for microbial fouling. Increased fan power and electricity consumption are necessary to achieve the same cooling effect over the fins.

Many elements of an air conditioner could be considered for improvement, including refrigerant type, fin shape and length, fan efficiency or modifying the existing evaporator coil fins to prevent filmwise condensation. It is desired to find a solution that would be readily adopted by industry, could be applied to existing systems, and would be cost competitive and durable. One such solution is improving the evaporator coil performance, namely, the design of the aluminum fins. While configurations such as louvred fins would offer increased heat transfer surface area, these designs are not currently in as high a production as traditional fin-tube heat exchangers, as shown in Figure 1, due to the added complexity in manufacturing. Keeping in mind the goal for a low-cost, readily adoptable solution, the following research focuses on manipulating sheet aluminum fin stock. The primary concern then is solving the problem of formed condensation on the fins that impedes heat transfer. Accelerated dropwise condensation and droplet shedding can be achieved on surfaces that are hydrophobic, or water repelling, and that have good water roll-off characteristics so that droplets don't get pinned. To enhance a surface's hydrophobicity, mechanical, chemical, or combined means can be used to create additional surface roughness or lower surface energy. The effects of this, described in the following sections, minimize water film formation, accelerate condensation and shedding, and shed droplets at sizes small enough to prevent bridging in fin gaps. As surface roughness is increased, wettability theory predicts that the apparent contact angle of a water droplet on the surface will increase for a hydrophobic surface, potentially leading to better dropwise condensation and shedding characteristics. Extensive research has thus recently been performed to evaluate textured surface morphologies and superhydrophobic surfaces with both chemical and morphological alterations for applications pertaining to condensation, desalination, heat transfer, fog collection, anti-icing, and drag reduction[7–11].

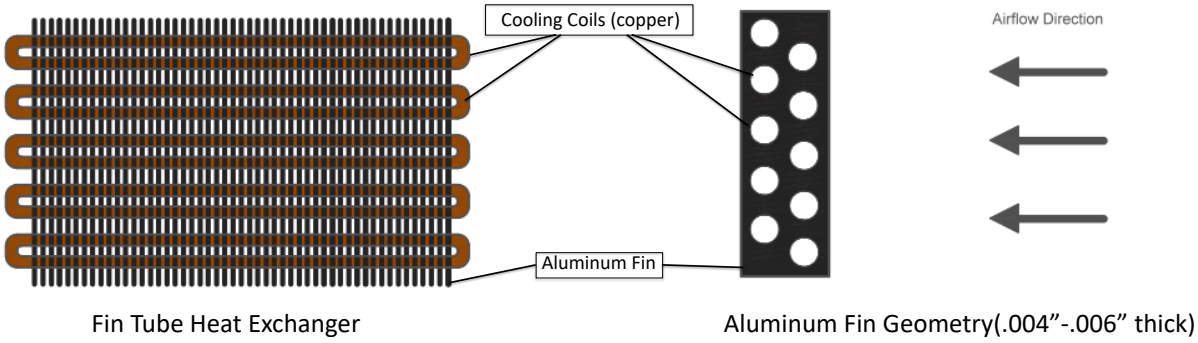

Figure 1: Schematic of an air conditioner fin-tube heat exchanger.

1.3 Potential impact

The successful development of practical condensation-accelerating surface technologies could have enormous potential for reducing electricity consumption worldwide while enabling more people to afford the comfort and higher productivity offered by air conditioning. There is also great potential to integrate dehumidification surfaces with systems to recycle the captured water for later use — with further reductions in energy usage. Promising results in this project would provide a strong basis for more extensive studies of the operation of dehumidification surfaces, and for the development of processes to manufacture them.

In addition to exploring applications specifically related to air conditioner coils, a further aim of this project is to identify other possible sectors that could benefit from a condensation-accelerating technology for increased efficiency. Potential candidates might include cooling systems for electronics, data farms, or even cooling for space habitats.

1.4 Bio-inspired Design

Surfaces exhibiting exceptional water droplet shedding capabilities and superhydrophobicity have been observed in nature[11]. Examples include: the lotus leaf, rice leaf, butterfly wing, water strider leg, gecko foot, mosquito eye, and rose petal, to name a few, and are shown in Figure 2 and Figure 3[12,13]. For instance, the lotus leaf, long held as nature's standard for superhydrophobic surfaces, exhibits a static contact angle of 164° with contact angle hysteresis 3°. Composed of 3–10 μm protrusions and valleys, with 70–100 nm particles, the lotus utilizes a hierarchically micro- and nanostructured surface to facilitate droplet coalescence and shedding[12-13]. Numerous studies have shown that the combination of nano- and microstructures promotes higher contact angles with lower adhesion to improve droplet shedding to a greater extent than a microstructured surface[14–16]. Similarly, the rice leaf has micropapillae structures with nanolength hairs; however, the structures are oriented anisotropically so that wetting properties are directional. In the direction along the edge of the leaf, the droplet roll off angle is between 3° and 5°, and the roll-off angle is between 9° and 15° along the perpendicular direction[17]. The butterfly wing structure is similarly designed to be both superhydrophobic and have directional adhesion properties. The water strider uses needle-shaped hairs with diameters ranging from 3 µm down to several hundred nanometers with hairs oriented in such a way that air is trapped between the leg and water surface[18]. In order to achieve a water static contact angle of 167° for taking advantage of water surface tension to "walk" across pond surfaces, features are 50 µm in length and arranged at an inclined angle of approximately 20° from the surface of the leg[19].

The gecko foot is also designed to be superhydrophobic, have high and reversible adhesion, and have self-cleaning properties. Its structures consist of setae, well-aligned micro-hairs of 5 µm in diameter and 110 µm in length, and smaller nanoscale tips called spatulae. Contact angles with water have been reported as high as 160° along with strong

adhesive forces[20]. The mosquito compound eye is superhydrophobic, has antifogging properties and has reflective and self-cleaning properties[21].

These organisms take advantage of surface roughness and superhydrophobicity to improve droplet coalescence, droplet shedding, and self-cleaning properties. In addition to the lotus and rice leaf structures, the rose petal is another example of a superhydrophobic surface that, instead, exhibits high levels of surface adhesion[22]. Droplets will stick even when the surface is turned upside down. This behavior is due to the difference in microstructure size. On the rose petal, periodic micropapilla arrays of 16 μm diameter and 7 μm height covered on top by nanoscale cuticular folds of about 730 nm width create the hierarchical structure[23]. Although the protrusion curvature is similar to that of the lotus leaf, the hierarchical structure on the rose petal is much larger, allowing water droplets to enter the larger grooves and experience pinning. For applications of droplet shedding, self-cleaning properties, drag reduction, and defrosting, to name a few, the lotus leaf appears to be more attractive[24].

As a results of these wettability characteristics, there are widespread efforts to emulate these biomimetic structures on an industrial scale for broader applications such as surfacing of aircraft or ships, microfluidic devices, and heat transfer enhancement in Heating, Ventilation and Air Conditioning (HVAC) systems.

Figure 2: Lily pads and lotus plants in their natural habitat

.

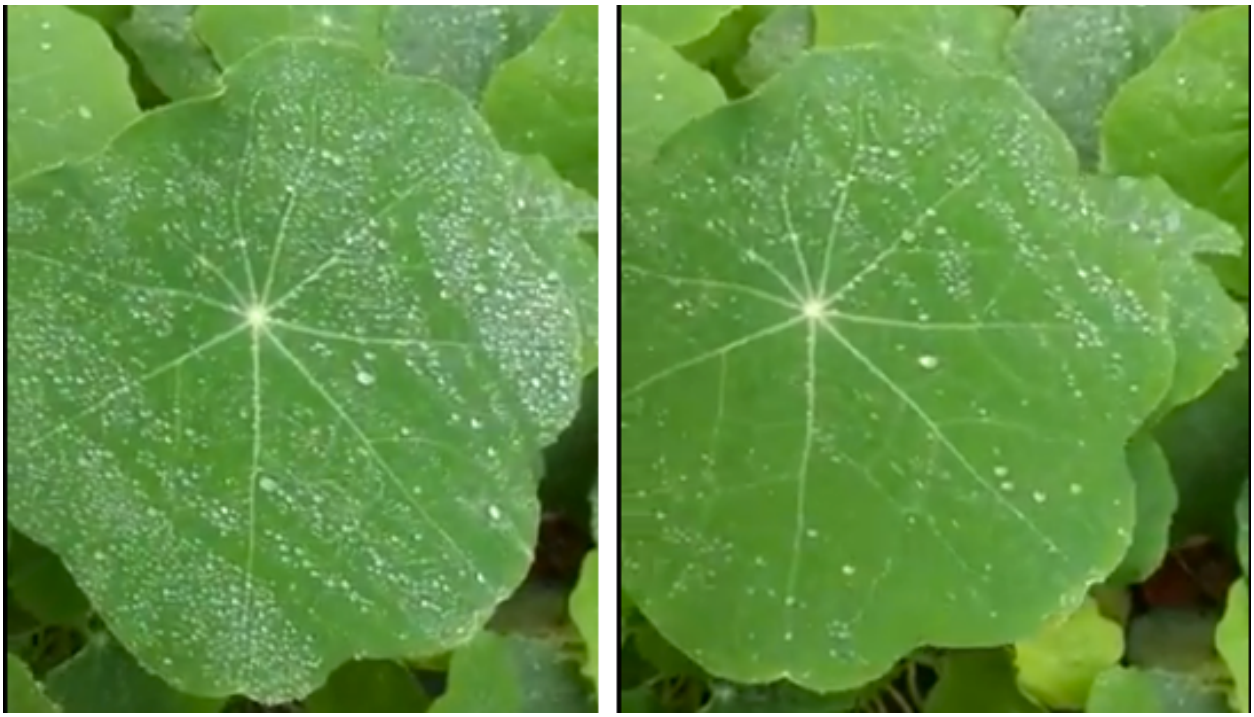

Figure 3: Example of water dropwise condensation and water shedding on a broad-leaf plant.

1.5 Theory of Wetting

1.5.1 Types of Wetting Behavior

In a closer look behind the mechanisms determining hydrophobicity, shedding and adhesion, wettability of a surface is determined by the force balance or interfacial tensions between the solid, liquid and vapor interfaces occurring at the three-phase line of contact shown in Figure 4. This relationship was first postulated by Thomas Young in 1805 and created a means of determining surface energies simply by measuring the contact angle a droplet of known surface energy formed on a given substrate, assuming a completely flat surface[25].

$$\gamma_{LV} cos\theta_y = \gamma_{SV} - \gamma_{SL} \quad (1)$$

where θ is the contact angle, γ_{LV} is the liquid surface free energy, γ_{SV} is the solid surface free energy, and γ_{SL} is the interfacial free energy between solid and liquid.

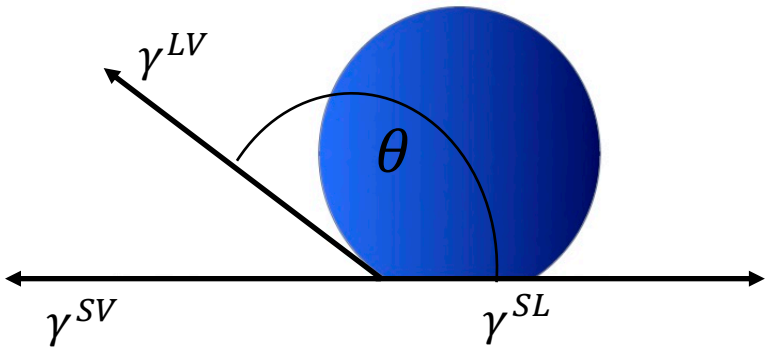

Figure 4: Young's surface energy balance for a planar surface at the three-phase contact line.

Common means of characterizing the wettability of a surface are static and dynamic contact angle measurements and contact angle hysteresis. Some surfaces experience a high amount of wetting due to increased surface interaction between the liquid and substrate and have a contact angle between the liquid and surface less than 90°. Such surfaces are considered hydrophilic. Surfaces with a contact angle greater than 90° are considered to have low wettability and are termed hydrophobic, in the case of water as a liquid. Surfaces with contact angles greater than 150° are considered to be superhydrophobic and have superior droplet shedding capabilities as well as self-cleaning properties due to low surface area contact between the droplet and surface (Figure 5)[26].

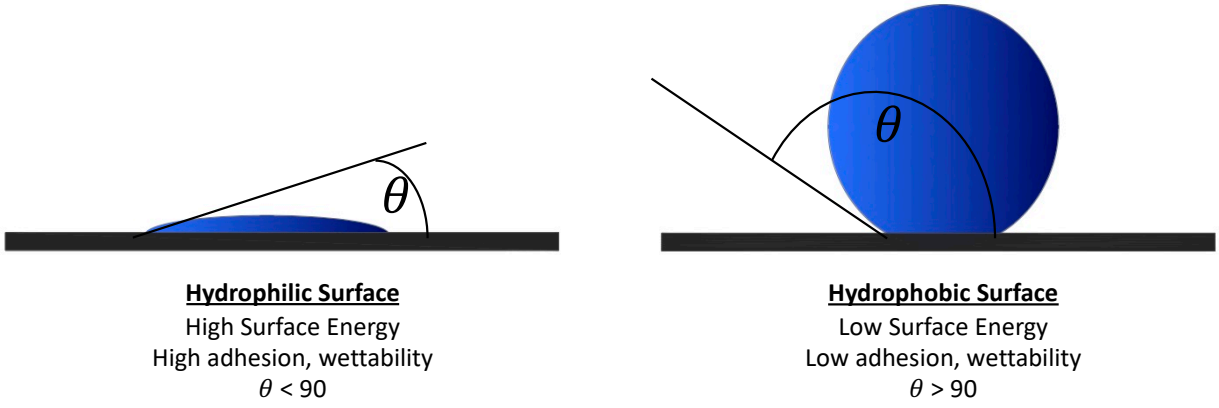

Figure 5: Schematic of a hydrophilic and hydrophobic surface interacting with a water droplet.

For the wetting fluid, fluids dominated by cohesive forces tend to remain more spherical while those dominated by adhesive forces and higher surface energy wet a surface. Both the static contact angle measurement and dynamic contact angle measurements, which are associated with droplet roll-off, also indicate the strength of cohesive and adhesive forces for a droplet on a surface.

Hydrophobicity and hydrophilicity can be achieved through mechanical, chemical, or dual mechanical and chemical means. By altering the surface morphology to create additional surface roughness, a droplet in contact with that surface will experience a perceived contact area greater than the projected surface in the case of hydrophilicity. Depending on the scale of the surface roughness, water will be wicked into surface features via capillarity thus increasing the wettability. For a hydrophobic surface, water droplets are able to perch on top of the features and thus make contact with a smaller area than the projected area of the flat surface. The lower contact area allows for a higher apparent contact angle. In addition to morphological modifications of a surface, chemical functionalization can also be used to increase or decrease surface energy for enhanced water interaction. Chemicals that increase surface energy will create a surface to which water will have a strong affinity. Adhesive forces will be stronger than cohesive forces and water will preferentially spread across the surface as opposed to bonding to itself to minimize droplet surface area. In the case of lower surface energy, water will exhibit stronger cohesive forces than adhesive forces and will bead up with itself rather than bond to the surface.

Often, fluorine-terminated compounds, which are extremely low in surface energy, will be used to create superhydrophobic surfaces. Examples include many variants on the silane molecule. As part of a chemical coating process, it is desired to have a self-assembled monolayer form on the surface to minimize non-uniformities[27]. Such monolayers can be attained through various means of deposition including dip coating, spray coating, and chemical vapor deposition (CVD)[28]. For lab-scale synthesis, CVD is a convenient and easy means of achieving a silane monolayer on a surface to lower surface energy. A vacuum desiccator or bell jar is used as a pressure vessel. A few drops of the chemical compound as well as the sample surface are placed in the jar, and a vacuum pumpdown process is used to achieve pressures low enough for the evaporation of the silane molecule to occur. The vacuum is turned off and the evaporated silane is allowed to deposit onto the substrate surface. In this research, triethoxysilane was used, as opposed to a trichloro-based silane. The motivation for this selection was the zinc oxide coating described later in this paper. Zinc oxide nanostructures are simple to grow in a hydrothermal process and are a convenient means for introducing surface roughness to aluminum[29,30]. However, chlorine gas will dissolve certain metals, including zinc, and cause melting of the surface features as a result of being off-gassed during the chemical vapor deposition process.

1.5.2 Wenzel Wetting

In the case of hierarchical or textured surfaces, the amount of surface area seen by a droplet varies, and a new model, taking surface roughness into account, is required to describe the contact angle. Such surfaces, if manufactured in a controlled process, often utilize channels, pillars or porous structures on the micro- or nanoscale. The first model was proposed by Robert N. Wenzel[31,32]:

$$cos\theta_W = rcos\theta_O \quad (2)$$

where θ_W is the Wenzel contact angle, r is the surface roughness and θ_O is the original contact angle that is predicted by Young's equation. The roughness factor, r, is the ratio of total to projected surface area. The Wenzel model describes a fully wetted surface where the droplet penetrates between any pores on the substrate, thus increasing the contact area seen by the droplet (Figure 6).

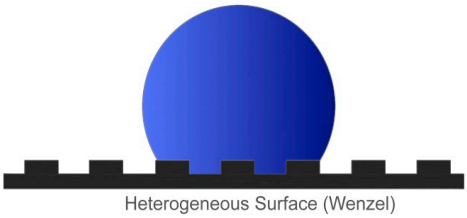

Figure 6: Schematic of Wenzel wetting of a droplet on a roughened surface.

Wenzel surfaces may possess higher contact angles than untreated surfaces; however, due to the surface features impaling the droplet, the droplet becomes highly pinned and will have a correspondingly higher roll off angle. For a hierarchical surface in a Wenzel wetting state, the roughness factor becomes a function with respect to the particular surface.

$$cos\theta_W = r(x,y)cos\theta_O \quad (3)$$

1.5.3 Cassie–Baxter Model

Cassie and Baxter proposed another mechanism for droplet-surface interactions[33]. The Cassie–Baxter model is used for a droplet that is suspended on top of any surface roughness or features and takes into account the surface-air interfacial energy, shown in Figure 7. Air is trapped in the space beneath the droplet, which aids in minimizing the interfacial energy between the droplet and surface and allows for easier roll-off. Surface texture can be manufactured specifically to control the surface energy and encourage a Cassie–Baxter state. Although surface area contact between the droplet and surface is minimized, the droplet has a greater potential energy in this state and will favorably transition to the Wenzel state if the droplet overcomes the Laplace pressure to wet the pore. The Cassie–Baxter model describes a new apparent contact angle.

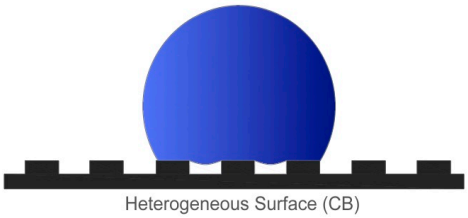

Figure 7: Schematic of Cassie–Baxter wetting of a droplet on a roughened surface.

$$cos\theta_C = \phi(cos\theta_c + 1) - 1 \qquad (4)$$

where ϕ is a Cassie roughness factor defined as the ratio of the total top surface area to the total projected surface area. For hierarchical structures, the Cassie–Baxter model is modified based on interactions with a non-constant surface roughness.

1.5.4 Cassie–Baxter-to-Wenzel Transition

The energy barrier in going from a higher-energy Cassie–Baxter droplet to lower energy Wenzel droplet is achieved primarily through one of three mechanisms[34,35]:

1. Laplace mechanism: For a given droplet, the pressure difference between the inside and outside of the droplet is caused by the surface tension at the interface of the fluid of the droplet and the surrounding fluid or surface. As the droplet shrinks in size and its boundary radius of curvature is reduced, this pressure, known as the Laplace pressure, within the droplet increases. The greater Laplace pressure enables the droplet to overcome the capillary pressure required to force water to wet into the textured surface as shown in Figure 8. The smaller capillary pressure encourages the droplet to wet any asperities in the surface and transition to Wenzel mode[36].

2. Depinning mechanism: The interface of the droplet slowly seeps into the roughness of the textured surface and comes into contact with the bottom of the substrate. Once this occurs, transition has occurred.

3. Sag mechanism: If the pressure within the droplet increases to a particular amount, the interface of the droplet and surface will cause the droplet to bulge and sag into the asperities, primarily if the gravitational force of the droplet is substantial enough to overcome the capillary force. Similar to the depinning mechanism, if the droplet sags enough into the roughened features so that it touches the substrate, the surface will wet and transition to Wenzel mode.

Although Wenzel and Cassie–Baxter are the primary modes considered for surface wetting, there also exists a metastable Cassie–Baxter state or partially-wetted state between droplets sitting on the tips of the texture and those completely filling pores[37,38]. Characteristics of a metastable state include an internal Laplace pressure that is too low to overcome the energy barrier necessary for transition to a fully wetted Wenzel mode or to overcome the capillary pressure. Depending on the texture design with respect to feature spacing, size, and curvature, such a surface should also exhibit superior roll-off properties because the droplets on the surface are still not fully pinned[39,40].

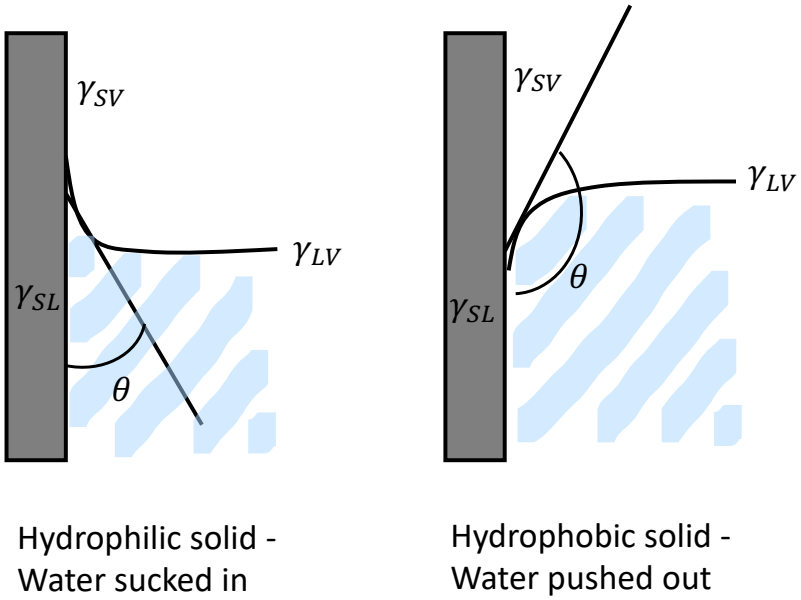

Figure 8: Laplace pressure mechanism acting on water in a capillary tube. In the case of a surface pore, the hydrophilic substrate would suck water into the pore while the hydrophobic substrate would push water out of the pore.

The takeaway from the Wenzel and Cassie–Baxter formulations is that increased roughness makes a hydrophilic surface more hydrophilic and a hydrophobic surface more hydrophobic due to the roughness coefficient. In the case of hydrophobicity, the apparent contact angle is increased. Visualizing this with respect to a surface pore, it can be seen that surface tension and capillary action are the primary forces affecting a droplet at microscopic length scales[41,42].

1.6 Contact Angle Hysteresis

Contact angle hysteresis, the difference between the advancing contact angle and the receding contact angle of a droplet, is a means of surface characterization by measuring the energy dissipated as a droplet flows along the surface of a substrate[43]. Surfaces with low contact angle hysteresis exhibit good self-cleaning capability because the droplet is more likely to roll off the surface rather than simply slide when the surface is tilted. The rolling droplet is able to pick up any residual dust particles and sweep them

off the surface. Contact angle hysteresis below 10° will also typically have low roll-off angles. For highly roughened surfaces, it is possible to reach contact angle hysteresis less than 1°. However, if surface roughness features are large enough in size relative to the droplet length scale, the droplet could potentially pin to the surface and have high roll-off angles and high contact angle hysteresis. Such behavior is not ideal for applications involving droplet shedding. In order to determine contact angle hysteresis, two methods are generally employed: the volume-changing method and the tilting cradle method[44].

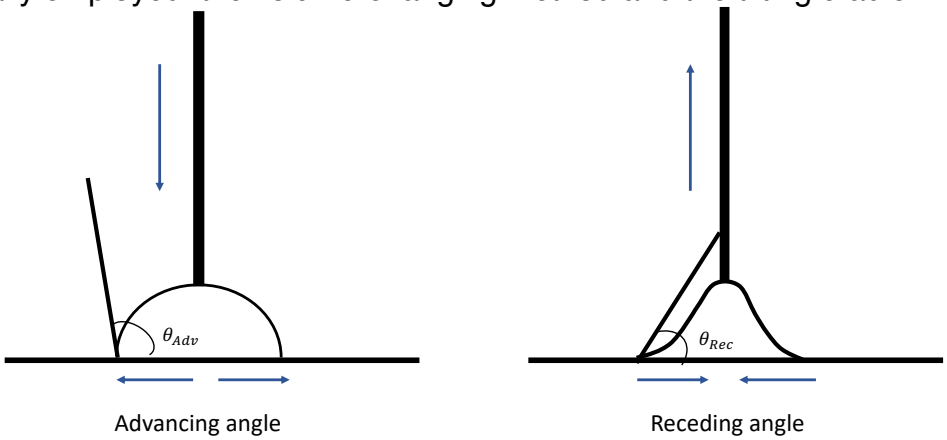

Figure 9: Volume-changing method for determining contact angle hysteresis.

(1) The principle of the volume changing method (Figure 9):
In short, a small droplet is first formed and placed on the surface. The needle is then brought close to the surface and the volume of the droplet is gradually increased while recording at the same time. This gives the advancing contact angle. The receding angle is measured the same way; but this time, the volume of the droplet is gradually decreased.

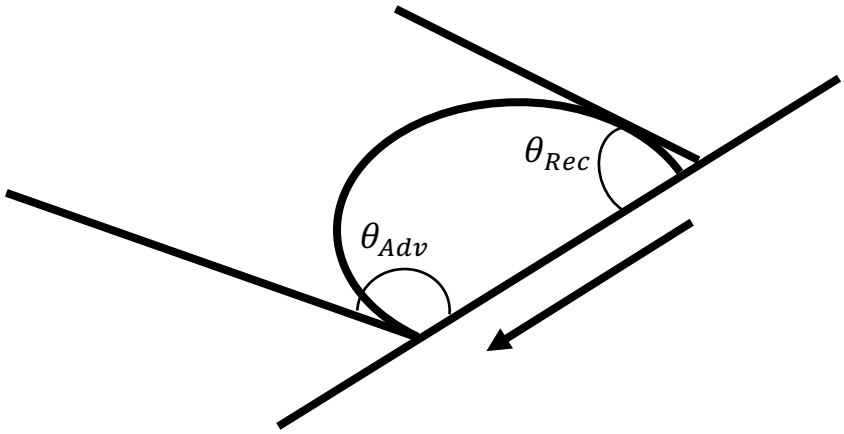

Figure 10: Tilting cradle method for determining contact angle hysteresis.

(2) The principle of the tilting cradle method (Figure 10):

The droplet is placed on the substrate, which is then gradually tilted. The advancing angle is measured at the front of the droplet just before the droplet starts to move. The receding contact angle is measured at the back of the droplet, at the same time point.

1.7 Types of Condensation

Condensation occurs when the surface temperature is less than the saturation temperature of an adjoining vapor phase. Heat is transferred from the vapor to the surface, and in the process of the vapor phase losing temperature, it will experience sensible heat loss and latent heat loss, causing phase-change to liquid. While in dehumidification processes this is the desired result, in air conditioning and refrigeration systems, condensation on the evaporator coil surfaces acts as a thermal barrier for further heat transfer. Water has a low thermal conductivity and impedes convective heat transfer from the inlet air to the evaporator coils.

There are two main modes of condensation associated with phase-change heat transfer at a surface: filmwise condensation and dropwise condensation[26]. Filmwise condensation occurs when droplets coalesce and form a thin layer of water on a surface. Dropwise condensation occurs when droplets form on a surface and retain their individual shape. Droplets may coalesce to form larger droplets but do not completely lose their curvature. In the particular application of air conditioning and heat transfer systems, filmwise condensation of water vapor on evaporator fins is not desired because it can reduce the efficiency of or impede heat transfer — increasing energy consumption. Dropwise condensation allows for improved heat transfer because, while part of the surface is obstructed by the droplets, the remaining surface is free for convective heat transfer[16,45]. However, in the case of evaporator coil fins which are spaced about 2 mm apart, larger droplets can also bridge between adjacent fins, impeding airflow.

1.8 Bio-inspired Design Literature Review

Current research in altering surface morphology to demonstrate certain physical properties has become a highly popular topic. Micro- and nanostructure surface textures on metal and polymer substrates are produced to increase surface roughness for self-cleaning, condensation acceleration, droplet shedding and hydrophobic purposes. Polymer substrates such as PDMS and PTFE already exhibit hydrophobic properties while metal substrates, such as aluminum, are naturally hydrophilic due to their native oxide layer[46,47]. To alter these surfaces, scientists have both mechanically and chemically modified them in order to increase surface roughness and hydrophobicity.

Feng et al. produced superhydrophobic surfaces consisting of nanofibers made of hydrophilic poly(vinyl alcohol). They achieved a contact angle of 171°, where the original, untreated surface had a contact angle of 72°[48]. Cao et al. fabricated porous Si film with micrometer-sized asperities and nanometer-sized pores. Their measured contact angle was about 160°[49]. Wang et al. used T-shape micro-pillar structures coated with diamond-

like carbon for a contact angle of 167°[50]. Koch et al. reported hierarchical structures with mechanical microstructures and nanostructures of hydrophobic wax that increased surface roughness to produce static contact angles of 173° and low contact angle hysteresis of 2°[51,52]. Bhushan et al. studied hierarchical structures produced from carbon nanotube composite with a static contact angle of 170° and a contact angle hysteresis of 2°. The method of fabrication included a micropatterned silicon surface using an epoxy resin and spray deposition of the carbon nanotube composite[53]. The same group also used a hierarchical structure composed of a microstructure with a superimposed nanostructure of hydrophobic waxes. They achieved a contact angle of 173° and contact angle hysteresis of 2°[12,54].

To achieve the metastable Cassie–Baxter phase mentioned previously, Varanasi et al. used pillar-post array formation for microstructure formation and nanopores for nanostructures on the surface of the substrate[39,55]. It was found that for arrays of square posts 15 μm wide and 25 μm high, the dependence on post spacing-to-width ratio, b/a, was as follows: b/a < 1 showed no droplet roll-off; b/a < 1.8 showed that a Cassie–Baxter state was achieved; 1.8 < b/a < 6 exhibited a metastable Cassie–Baxter state and droplet roll-off angles of 17°; and b/a > 6 produced a Wenzel mode where droplets no longer rolled off. The results suggested that the Laplace pressure inside the droplet was still too low to overcome the capillary pressure of the asperities — resembling a standard Cassie–Baxter state. The model developed by Varanasi et al. for contact angle hysteresis in a metastable Cassie–Baxter state is shown below.

$$\theta_{adv} - \theta_{rec} = (1 - f_{LA}) R_f \frac{cos\theta_{aO} - cos\theta_{rO}}{-sin\theta} = \left(\sqrt{1 - f_{LA}}\right) R_f \frac{cos\theta_{aO} - cos\theta_{rO}}{\sqrt{2(R_f cos\theta_O + 1)}} \quad (5)$$

$$r = 1 + \frac{4(\frac{h}{a})}{(1+\frac{b}{a})^2} \quad (6)$$

where *r* is a modified roughness factor showing the interfacial energy between air and liquid and interfacial energy between the solid and liquid droplet based on the spacing and height dimensions of the pillars.

In addition to fabricating hierarchical structures through micropillar arrays and silanization, Jacobi et al. have, in a series of well documented experiments, etched channels ranging from 5 to 40 μm in width and 5 to 27 μm in depth for analyzing contact angle measurements and roll-off angles on anisotropic patterned surfaces. Measurements included an advancing contact angle on the unpolished aluminum baseline of 85° and an advancing contact angle of 70° on the polished baseline surface. Microgroove structures demonstrated advancing contact angles ranging from 35° to 56° with smaller angles associated with the narrower and deeper channels. These were characteristic values for the Wenzel regime. For the Cassie–Baxter regime, contact angles ranged from 104° to 131° purely based on micro-level surface alterations[56–58]. This finding suggests a metastable Cassie–Baxter case for the microchannel surface,

where the walls of the channels serve as an energy barrier for the droplet and allow the droplet to elongate in form along the length of the channel.

Hierarchical structures with the purpose of specifically mimicking the lotus leaf morphology have also been manufactured primarily through mechanical microstructures and chemically deposited or etched nanostructures[59]. Numerous methods, including: electrodeposition and electrochemical deposition of nanoparticles and films followed by treatment with superhydrophobic materials; coating with films of sublimation materials; use of organic and inorganic fillers with multimodal particle size distribution for particles in the matrix of the hydrophobic material; template methods for preparation of rough surface treatment with hydrophobic materials; controllable aggregation of nanoparticles on the surface; photolithographic techniques followed by treatment with hydrophobic materials such as silane; and etching of the surface of materials followed by treatment with hydrophobic materials have been utilized. These surfaces have been characterized primarily through static contact angle measurements, contact angle hysteresis, droplet roll-off angle, or dynamic dip testing. The wetting mechanism for a droplet that nucleates and condenses on a treated hierarchical surface has been demonstrated experimentally but has yet to be fully modeled in the existing literature[60–62].

In the extensive work that has been performed to create artificial, superhydrophobic biomimetic structures with multiscale roughness, some of the more recent insights indicate that the hierarchical nature of the structures can be optimized to both produce a maximum static contact angle and minimum contact angle hysteresis.

As inspiration for the microstructured pattern of a hierarchically structured designed surface, microgrooves and micropillars, commonly fabricated in the literature and having easily tunable dimensions and bulk physical properties, were investigated. For example, Yoshimitsu et al. found improved water shedding behavior on metal microgrooved surfaces compared to surfaces with micropillars due to the presence of a lower energy barrier and a discontinuity in the three-phase contact line due to the pillar array[63]. Chen et al. used laser microfabrication to create a superhydrophobic hierarchical surface with tunable adhesion properties. Microchannels and pillars were used for the larger structures[64]. Sun et al. compared varying micropillar array surfaces for superoleophobic properties. These included 20 μm pitch micropillar arrays, 2.5 μm pitch micropillar arrays, and gecko foot-like hierarchical microstructures. Techniques for fabrication included lithography and transfer via a PDMS mold. Their results showed that high surface roughness correlated with extreme underwater superoleophobicity and adhesion. They also tested for superhydrophobicity and recorded contact angles as high as 163±2°[65]. Wier et al. observed condensation formation on micropillar arrays using an optical microscope. They found that droplets formed initially in the spacing between pillars and then coalesced with neighboring water droplets until they were pushed out of the pores due to capillarity and finally anchored onto the superhydrophobic surface atop the pillar structures. The droplets would then shed[66]. Wang et al. tested contact angle and droplet roll-off on chemically etched aluminum surfaces for ice adhesion. They found that

the multi-scale structures greatly improved surface resistance to ice adhesion and remained intact even after multiple freezing and breaking-off cycles[67,68].

While extensive work has been performed in characterizing roughened surfaces with randomized structures, microchannels or micropillar arrays,[69] there is a dearth in the literature of microdome surfaces or surfaces with an inherent curvature.[70] In addition, the aforementioned patterns and results are predominantly fabricated on polymer substrates or on small-scale samples, leaving further room in the field for techniques that allow for micro- and nanoscale metal patterning for large-scale use. This thesis initially investigates the characterization of micropillar arrays and later compares these results with dimensionally similar microdome arrays.

2 Chapter: Characterization of Micropillar-patterned hierarchically structured surfaces

2.1 Introduction

The objective of the micropillar analysis described in this Chapter was to examine the effects of micro- and nanoscale surface structures on water condensation behavior and droplet shedding from air-side heat transfer surfaces. Specifically, fabrication processes that have the potential to be used to modify aluminum evaporator coil fins at affordable cost were examined. Lithographically defined and plasma-etched periodic microstructures, chemically grown nanoporous zinc oxide (ZnO) films, and hierarchical combinations of these structures were fabricated. The surfaces were characterized with static water contact angle and droplet-shedding tilt angle measurements to determine superhydrophobicity. The microstructures, for ease of prototyping and to test multiple geometries, were produced using photolithography, deep reactive ion etching (DRIE), and aluminum sputtering. Lower surface energy was induced via silanization. A custom-designed and -built wind tunnel test-bed was used to test these surfaces under realistic condensing conditions with controlled relative humidity, air speed, and temperature in later chapters of this thesis.

2.2 Sample fabrication

A variety of manufacturing techniques was originally considered to test multiple microstructure patterns on aluminum; however, most methods were too time consuming, yielded inconsistent results, or were not cost effective for generating multiple patterns. These included micromilling, hot embossing from a mold, roll-to-roll processing, wire electrical discharge machining (EDM), and sand blasting. Although some of these techniques would later be considered for large-scale manufacturing, they were not suitable for multiple-pattern testing. As a result, photolithography was selected as a relatively easy means of generating multiple patterned samples while also allowing for pitch variation and for providing a surface to sputter aluminum for later hierarchical structure generation.

2.3 Fabrication and Testing Procedures

A test pattern consisting of 56 geometrically unique 0.4” × 0.4” squares was designed using AutoCAD. The designs varied pattern density and feature size for microchannel structures, pillar arrays and angled chevron grooves. A 5” chrome and soda lime mask was made (Front Range Photomask) to allow for photolithography to be performed on Silicon <100> wafers. To minimize etching nonuniformity later in the wafer processing, remaining empty space in the mask pattern was covered with a solid chrome

block pattern. For this experiment, patterns 10–25, which are detailed below and consisted of different micropillar arrays, were analyzed.

2.3.1 Mask Design and Detail

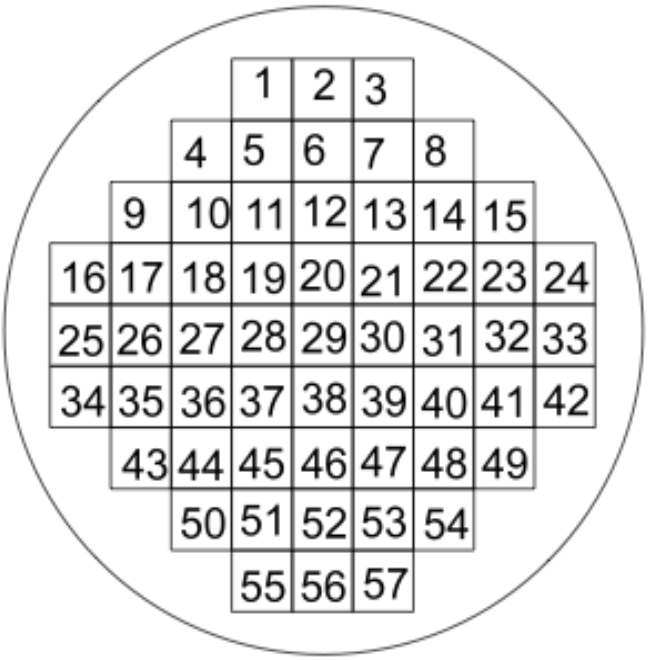

1. 5 µm inverted pillar, 5 µm spacing
2. 5 µm inverted pillar, 10 µm spacing
3. 5 µm inverted pillar, 15 µm spacing
4. 10 µm inverted pillar, 5 µm spacing
5. 10 µm inverted pillar, 10 µm spacing
6. 10 µm inverted pillar, 15 µm spacing
7. 15 µm inverted pillar, 5 µm spacing
8. 15 µm inverted pillar, 10 µm spacing
9. 15 µm inverted pillar, 15 µm spacing
10. 5 µm square pillar, 5 µm spacing
11. 5 µm square pillar, 10 µm spacing
12. 5 µm square pillar, 15 µm spacing
13. 5 µm square pillar, 20 µm spacing
14. 10 µm square pillar, 5 µm spacing
15. 10 µm square pillar, 10 µm spacing
16. 10 µm square pillar, 15 µm spacing
17. 10 µm square pillar, 20 µm spacing
18. 20 µm square pillar, 10 µm spacing
19. 20 µm square pillar, 20 µm spacing

20. 20 µm square pillar, 30 µm spacing
21. 20 µm square pillar, 50 µm spacing
22. 30 µm square pillar, 10 µm spacing
23. 30 µm square pillar, 20 µm spacing
24. 30 µm square pillar, 30 µm spacing
25. 30 µm square pillar, 50 µm spacing
26. Chevron, angled 30
27. Chevron, angled 45
28. Chevron, angled 60
29. Round post pattern
30. Chevron, angled 30
31. Chevron, angled 45
32. Chevron, angled 60
33. 5 µm raised groove, 5 µm spacing
34. 5 µm raised groove, 10 µm spacing
35. 5 µm raised groove, 15 µm spacing
36. 5 µm raised groove, 20 µm spacing
37. 10 µm raised groove, 5 µm spacing
38. 10 µm raised groove, 10 µm spacing
39. 10 µm raised groove, 15 µm spacing
40. 10 µm raised groove, 20 µm spacing
41. 20 µm raised groove, 5 µm spacing
42. 20 µm raised groove, 10 µm spacing
43. 20 µm raised groove, 15 µm spacing
44. 20 µm raised groove, 20 µm spacing
45. 30 µm raised groove, 10 µm spacing
46. 30 µm raised groove, 30 µm spacing
47. 30 µm raised groove, 50 µm spacing
48. 30 µm raised groove, 100 µm spacing
49. 50 µm raised groove, 10 µm spacing
50. 50 µm raised groove, 30 µm spacing
51. 50 µm raised groove, 50 µm spacing
52. 50 µm raised groove, 100 µm spacing
53. 100 µm raised groove, 50 µm spacing
54. 100 µm raised groove, 100 µm spacing
55. 100 µm raised groove, 150 µm spacing
56. 100 µm raised groove, 200 µm spacing
57. Blank

Since the project aim was to characterize varied microstructure pattern density, geometry and feature depth for aluminum fins used in evaporator coils, it was desired to transfer these patterns onto aluminum in a repeatable and quick process. A few options were available based on current equipment and material access.

2.3.2 Si Lithography, Etch, Deposition, Nanostructure Growth and Processing

A 6" wafer was used to fabricate the test samples. The wafer was coated in an oven with HMDS at 90 ˚C for 11 minutes in order to induce better adhesion with the photoresist. After, a 1.2 μm layer of i-line resist was used to coat the wafer following a procedure detailed in Table 1. The wafer was then taken to a mask aligner for a hard contact exposure with a 50 μm alignment gap for 6 seconds. After, the wafer was removed and developed with i-line developer with a 60 s hard bake post exposure step. In order to etch the patterns, an STS Deep Reactive Ion Etch (DRIE) tool was used. The wafer was cleaned, and any backside debris was removed. A 3-minute TDS clean oxygen plasma cleaning step was used before loading the wafer. A standard Deep Etch procedure was used to etch the wafer. The number of etch and passivation cycles was set to 50 (10–minute total run time) and run. The etch depths left vertical profile sidewalls and achieved 12–13 μm depths. This depth was measured using an optical interferometer.

Table 1: Si Lithography, Etch, Deposition, Nanostructure growth and Processing. Starting substrate: 6"-diameter Si wafer <100> n-type.

Step	Description	Lab	Machine/tool	Recipe
1.	**Coat: OiR 906-12 (i-line) 1.2*μ*m layer** HMDS coating Spin Soft Bake Exposure Develop Post Bake	NanoLab	 Primeoven Svgcoat1 Karl Suss MA6 Mask Aligner Svgdev2	 11min ramp run Program 1 Coat 90 ºC for 60 s, Cool 6 s Hard Contact 14 mW/cm^2 for 6 s 50 μm alignment gap Program 1 dev Program 1 oven
2.	**Etching Silicon** Cycle Times (s) C4F8 Flow (sccm) SF6 Flow (sccm) O2 Flow (sccm) Coil Power (W) Bias Power (W) Bias Frequency (MHz) Platen Chiller (°C) Etch Rate (nm/cycle) Total Cycle Time (min)	NanoLab	STS2	Passivation (P), Etch (E) 7 (P), 10 (E) 80 (P), 0 (E) 0 (P), 130 (E) 0 (P), 13 (E) 600 (P), 600 (E) 0 (P), 20 (E) 13.56 25 750 10
3.	**Al Deposition (×2 for 290 nm layer)** Composition Passes Power Pressure Thickness Reflectance	NanoLab	MRC944 Sputterer	 Aluminum/Silicon (98%/2%) 50 cm/min × 2 4 kW 8 mTorr 145 nm @780 nm: 257%

4.	**Dice Wafer**	Etcheverry Hall 1176B	Diamond Scribe	0.4" × 0.4" squares
5.	**Nanostructure growth, silanization**			
	Ultrasonicate in Acetone	1176B	Fume hood	
	Preheat aqueous equimolar chemical bath	1176B	Fume hood	25 mM zinc nitrate and hexamine, 70°C for 1 hr
	Dip Aluminum	1176B		70°C for 90 min
	Remove, Deionized Water (DI) Rinse, Air Dry	1176B		
	Remove residual organics	BNC	PETS RIE	Low power O_2 plasma ~60 W, 200 mTorr, 2 min
	Vacuum-deposit perfluorosilane	BNC	Desiccator	20 min pump down, 40 min settling time
	Immediate rinse with DI water	BNC		
	Air Dry	BNC		
	Anneal	BNC	Hotplate	120°C for 1 hour
6.	**Contact Angle Measurement**	1176B		5 μL water droplet

To prepare the different samples for contact angle and droplet roll-off angle testing, the surface energy of the wafer was lowered through deposition of a layer of Trichloro-1H, 1H, 2H, 2H-perfluorooctylsilane, creating a hydrophobic coating. The wafer was cleaned for 2 minutes in oxygen plasma with 12% RF power and a 10 sccm oxygen flow rate. It was then removed and taken directly to a vacuum desiccator. A few drops of silane were placed on a slide and the wafer was positioned so that the features were facing downward, and the samples were in between the vacuum pump and silane. The chamber was then pumped down for 20 minutes and the wafer was left in the vacuum environment for 40 minutes. Immediately upon removal from the vacuum chamber, the wafer was rinsed with ethanol and DI water and baked for an hour at 120 ˚C. The wafer was then sliced into smaller squares in order to perform static contact angle measurements.

A second wafer, following the above etching procedure, was then sputtered with a 150 nm layer of 99% aluminum using an MRC944 sputtering device. Both evaporation and sputtering of aluminum as a means of deposition were considered for this step of the process. Evaporation allows for a smooth aluminum layer on the feature surfaces; however, since evaporation is directional, the sidewalls of the features would not be coated. Due to the importance of a complete aluminum surface for characterizing water/aluminum interactions and for later ZnO growth, this would not meet the requirements of the experiment. Sputtering, with the procedure and protocol in the Table 1, would fully coat the features; however, more aluminum would be deposited on corners due to larger surface area, creating a minor key-hole effect. Due to the thin nature of the sputtered layer relative to the feature size, a significant key-hole effect was not observed in subsequent imaging. And the feature height, shown topographically in Figure 11, was able to be determined.

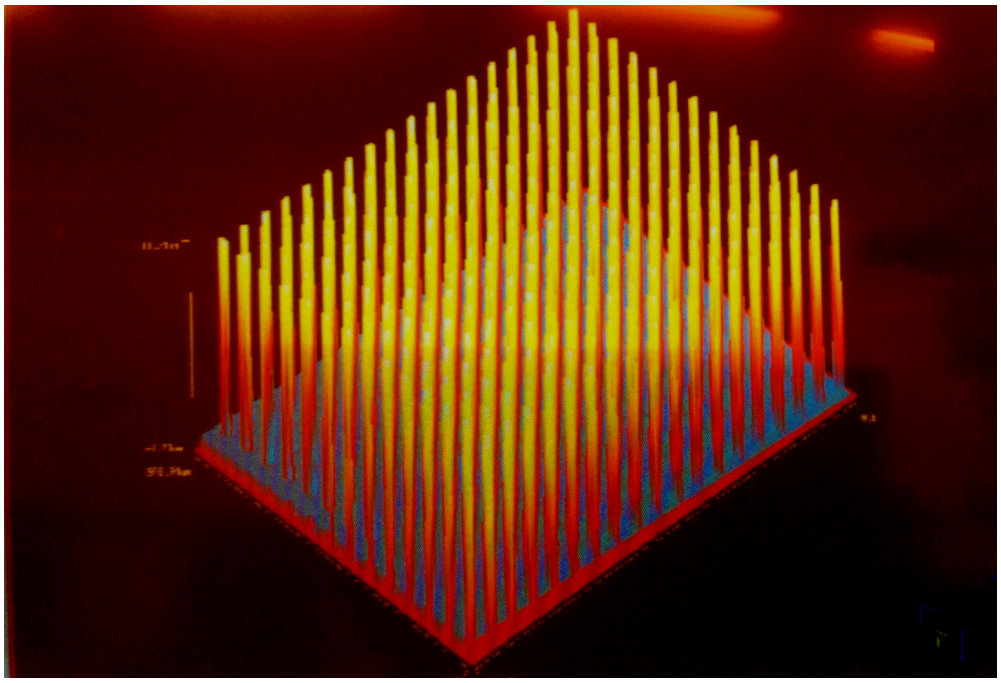

Figure 11: Interferometer topographical surface map of micropillar array; feature depth of 12 μm.

An unpatterned section of the wafer was diced and functionalized via the silane deposition process. The static contact angle for the baseline sputtered aluminum was measured to be ~105˚. The patterned sections of the wafer were chemically treated in a ZnO growth procedure to form nanopillar structures by reacting with the aluminum surface. The baseline nanopillar surface, with no microstructures present, had low roll-off angles and static contact angles ranging from 168˚ – 174˚. An aqueous, equimolar chemical bath of 25 mM zinc nitrate and hexamine was preheated at 70 ˚C for 1 hour. The aluminum coated wafer was placed into the solution and the temperature was maintained at 70 ˚C for 90 minutes.

The wafer samples were removed and rinsed with DI water and dried. The nanostructure growth was verified through SEM imaging, shown in Figure 12.

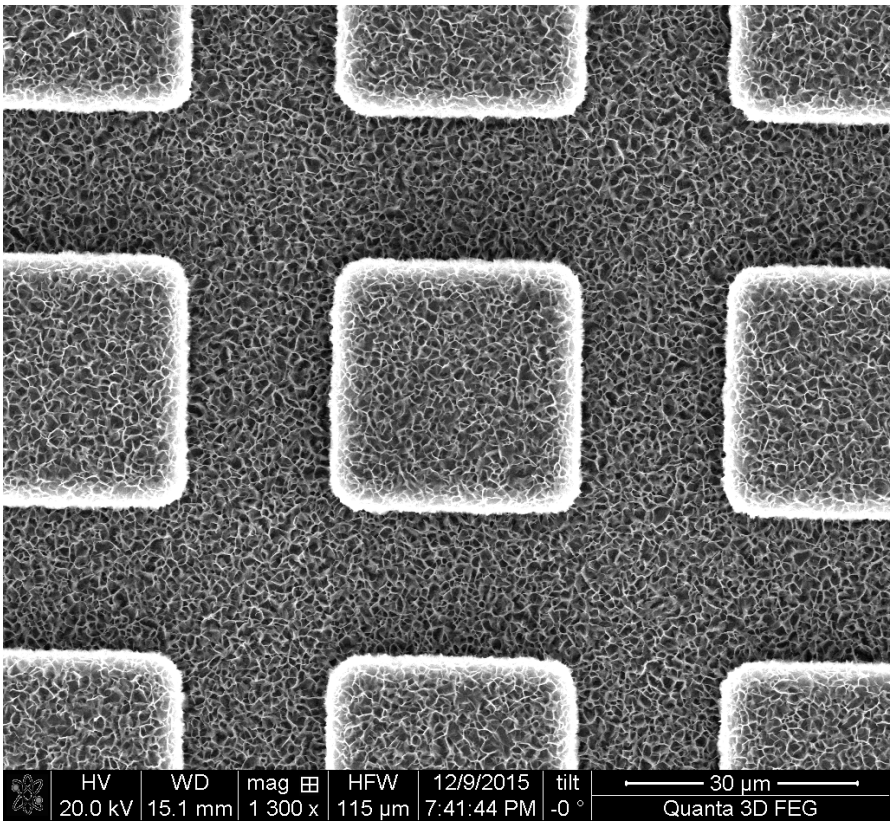

Figure 12: Scanning electron microscope (SEM) image of micropillar array micro- and nanostructure morphology.

Once processed and measured for feature depth, the individual square patterns were diced to create samples sufficiently small for the goniometer stage. In order to characterize the patterns, static contact angle measurements were performed using 5 μL droplets of water deposited statically onto the sample surface to eliminate any impact energy and negate effects of water hammer pressure. Five drops were measured per sample to determine an average static contact angle for a given surface morphology.

2.4 Results and Discussion

The goal of this experiment was to determine the effect of pillar microstructures and hierarchical structures on the superhydrophobicity and water shedding ability of the sample surfaces through static contact angle measurements. Sample data were taken for silanized samples of bare silicon, bare aluminum sputtered onto silicon, nanostructures grown onto the aluminum sputtered surface, a purely microstructure patterned surface, and a hierarchically patterned surface with micro- and nanoscale roughness. Static contact angles were measured for square micropillar arrays of varying pitch (the ratio of pillar spacing to width). Average contact angle values were compared between the functionalized microstructured surface and the hierarchical surface morphology in order to determine the contribution that the nanostructures had with respect to contact angle and droplet roll-off. The patterned samples were tilted until the droplet slid off in order to

determine the roll-off angle. For the purely microstructured patterns, droplet roll-off angle was impossible to determine due to the highly pinned nature of the droplet on the surface. Even rotating the sample so that the surface was upside-down did not remove the droplet. Thus, droplet angle variation was not able to be determined due to the pinning effect experienced by every pattern except for 12, 13, and 17 for both the microstructured and hierarchically structured surfaces.

In order to determine the wettability characteristics of the microstructured and nanostructured surfaces, baseline contact angle values were determined for silanized wafers. An unpatterned wafer had an average static contact angle of 105˚ and an Al/Si wafer with only the ZnO nanostructures grown had an average static contact angle ranging from 168˚–174˚. Both baseline surfaces had low roll-off angles.

Both the microstructured and hierarchically structured wafer samples had improved contact angle measurements over the unpatterned baseline value as shown in Table 2. Highlighted rows showed the greatest improvement.

Table 2: Microstructured and hierarchically structured sample contact angle measurements (five droplets/sample) relative to pitch.

Sample #	Pillar Dimension (µm)	Spacing (µm)	Avg drop CA Microstructured Wafer (˚)	Avg drop CA Hierarchical Wafer (˚)	Spacing:Width
10	5	5	156	154	1
11	5	10	164	165	2
12	5	15	171	175	3
13	5	20	136	175	4
14	10	5	155	152	0.5
15	10	10	156	154	1
16	10	15	161	168	1.5
17	10	20		173	2
18	20	10	154	153	0.5
19	20	20	155	162	1
20	20	30	156	165	1.5
21	20	50	167	174	2.5
22	30	10	151	153	0.333
23	30	20	156	157	0.666
24	30	30	154	169	1
25	30	50	166	160	1.666

Using the average contact angles determined from five measurements per sample, the effect of different parameters such as pitch (spacing:width) and surface roughness were compared. In addition, samples were compared to each other from both the microstructured and hierarchically structured surfaces.

In the above table, a value for pattern 17 was not included because there were two mechanisms at work. Half of the tested droplets did not pin and exhibited an average contact angle of ~163˚. The other half pinned and showed an average contact angle of ~113˚. A similar effect occurred with the droplet distribution of pattern 13. In addition, visualization through several of the photographed droplets demonstrated Cassie–Baxter modes of condensation for particular dimensions as can be seen in Figure 13.

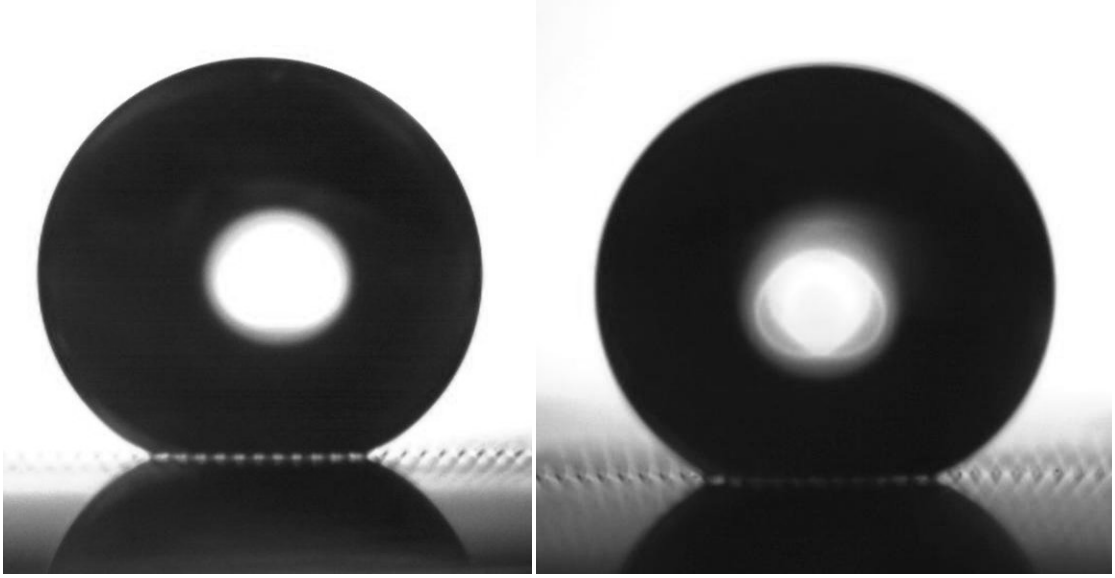

Figure 13: Pattern 25: (a) Microstructured surface with 164° CA (b) Hierarchically structured surface with CA of 164°.

Patterns 12 and 13 experienced roll-off angles less than 10˚ when tilted and were the only samples that did not experience pinning for both the microstructured and hierarchically structured surfaces. The other measured samples all experienced pinning. Pattern 13 was particularly interesting due to the distribution of contact angles on the microstructured surface. Three measured droplets pinned and began wetting the surface with an average of 112° (Figure 14) while droplets that did not pin or exhibited pinning in only a few features averaged a contact angle of 171° (Figure 15).

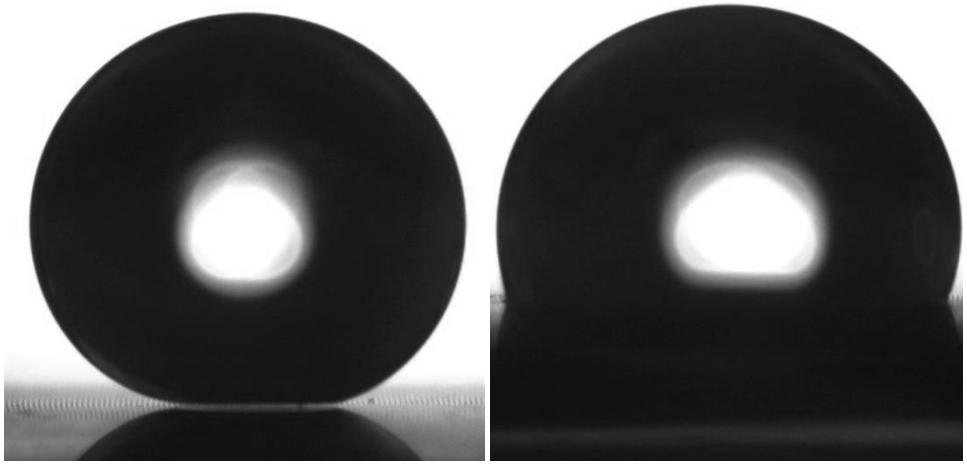

Figure 14: Pattern 13 (microstructured surface only): (a) Measured CA of 178° with no wetting; (b) Fully wetted droplet with measured CA of 109°.

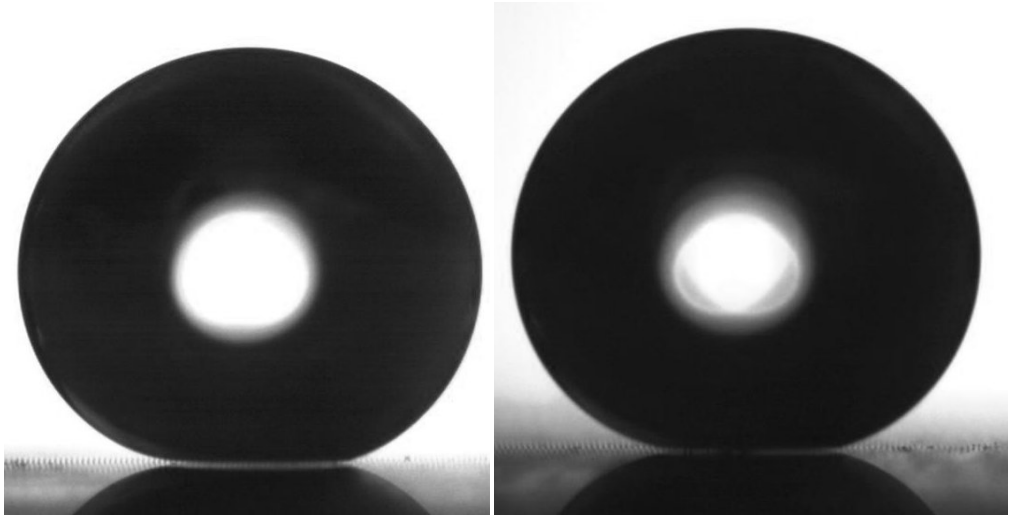

Figure 15: Pattern 13: (a) Microstructured surface in Cassie–Baxter mode (b) Hierarchical surface with some pinning observed in partial wetting state.

For the hierarchical pattern of #13, no pinning was experienced (Figure 15a), suggesting that the nanostructures affected the energy transition favoring Wenzel over Cassie–Baxter. Pattern 12 exhibited the greatest superhydrophobicity in both sets of data through high contact angle and low roll-off angle and never experienced pinning, suggesting that a Cassie–Baxter wetting state was the most favorable wetting state regardless of structural hierarchy (Figure 16).

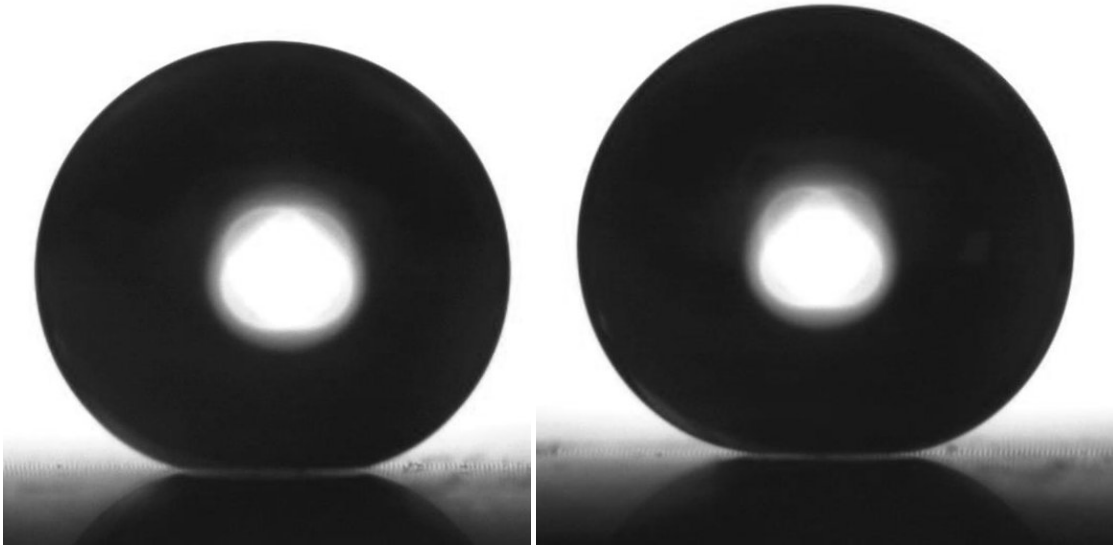

Figure 16: Pattern 12: (a) Microstructure surface with CA of 174°; (b) Hierarchically structured surface with CA of 178°.

Patterns 12 and 13 also had high surface roughness relative to other samples with the smallest-scale features and largest spacing.

A positive trend was observed as pitch increased for all samples as shown in Figure 12. The measured values for both the microstructured and hierarchically structured samples did not vary significantly; however, as the pitch increased for both, contact angle increased (Figure 17). The notable exception was pattern 13, where, due to the large spacing-to-width ratio of 4, the droplet was able to sag between the pillars and transition from the Cassie–Baxter to Wenzel mode. The remaining droplets experienced some pinning but did not transition fully, remaining in a metastable Cassie–Baxter state.

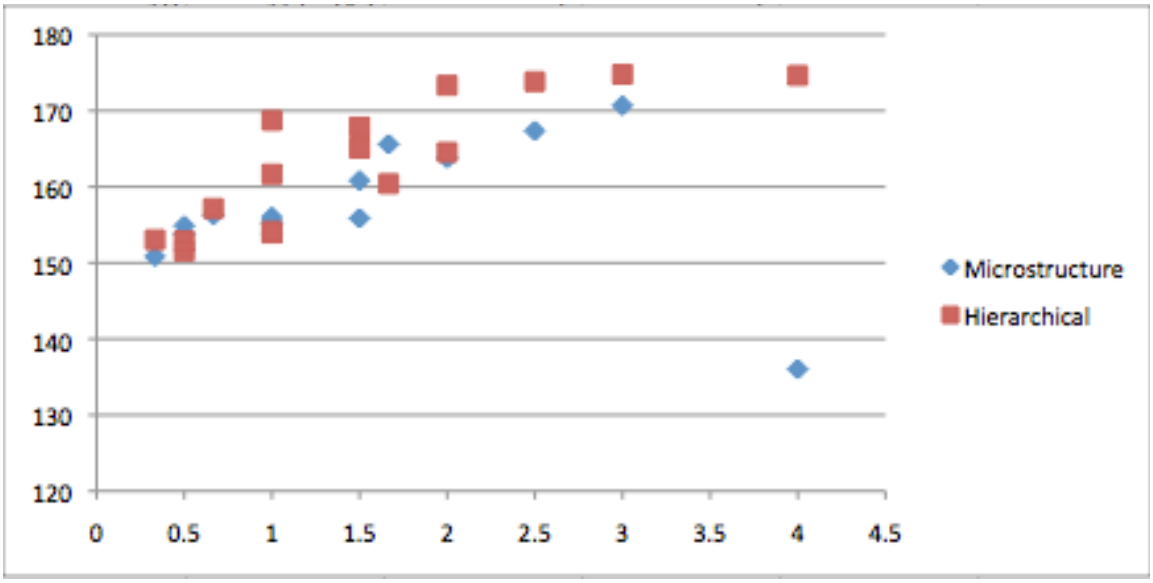

Figure 17: Spacing:Width (Pitch) vs. Measured Static Contact Angle.

Positive trends were also found between contact angle and pillar spacing with respect to a given post size. As the pillar spacing increased for a given post size, a linear trend could be observed for the average values (Figure 13) for each varying size. Error bars are shown with the mean contact angle to give a sense of the variability of the contact angle measurement results. The full range of tested droplets also demonstrated the same trend (Figure 14).

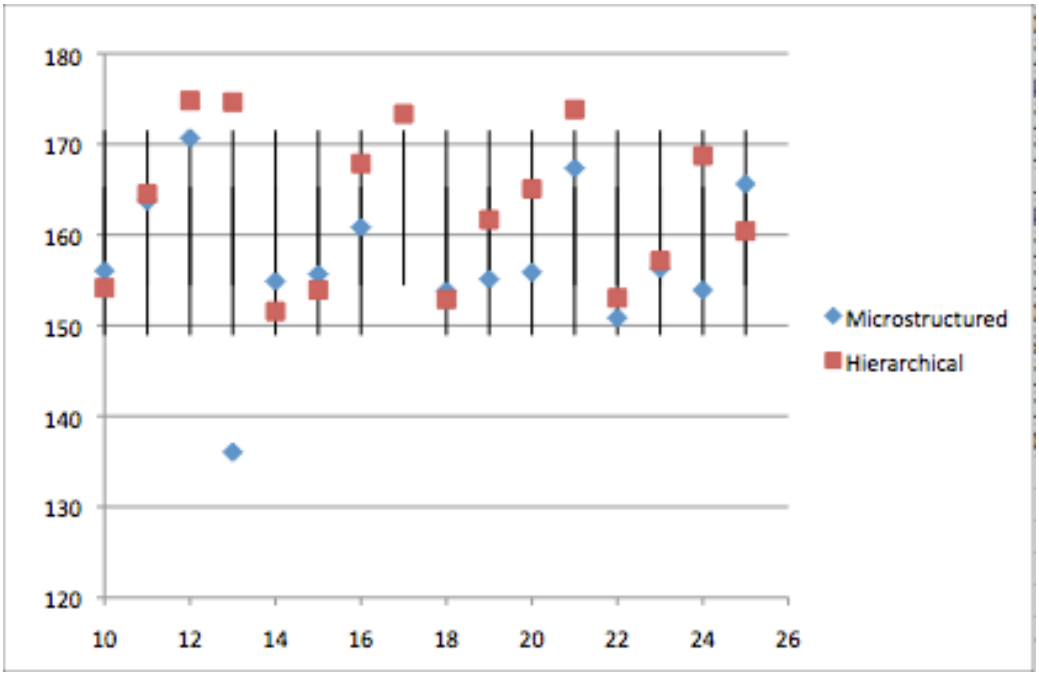

Figure 18: Sample Number vs. Average Sample Contact Angle with error bars.

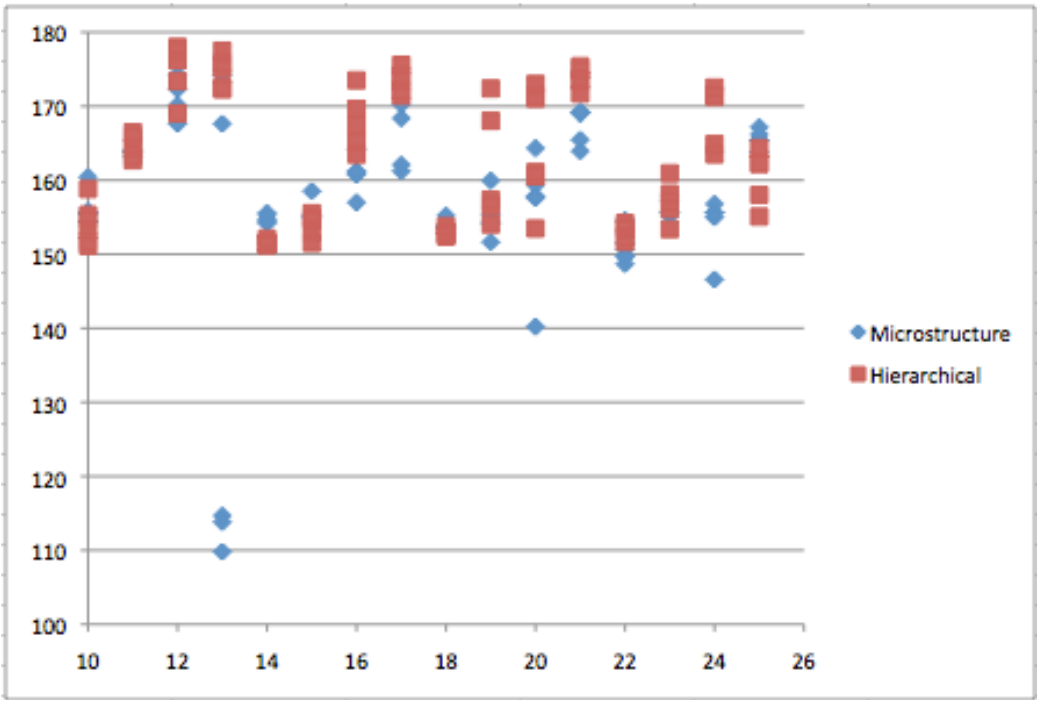

Figure 19: Sample Number vs. Contact Angle for all measured values.

Another factor of interest was the surface roughness utilized by the two classic wetting models: the Wenzel roughness factor, *r*, and the Cassie–Baxter area fraction, ϕ. Surface roughness varied between the two due to the differing projected and actual surface areas in each model. Length and gap values from Figure 20 were used for each pattern to calculate roughness parameters. In order to determine the effect of surface roughness with respect to both modes on the static contact angles, these parameters were calculated and are shown in Table 3[58]. The microstructured surface roughness factors were calculated for the Cassie–Baxter and Wenzel models using the equations below.

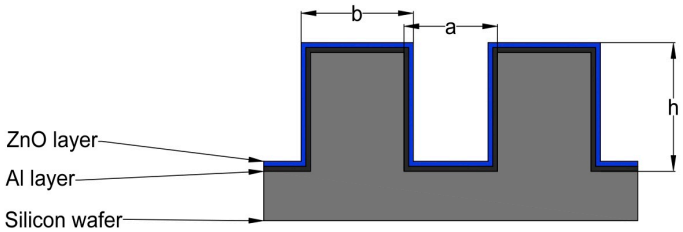

Figure 20: Coated Pillar Array Schematic.

$$\phi = \frac{b^2}{(a+b)^2} \quad (7)$$

$$r_w = \frac{4bh+(a+b)^2}{(a+b)^2} \quad (8)$$

Table 3: Microstructured and hierarchically structured sample surface roughness parameter values for Cassie–Baxter and Wenzel wetting models.

Sample #	Pillar Dimension	Spacing	Cassie Roughness	Wenzel Roughness
10	5	5	0.25	3.4
11	5	10	0.11111	2.06667
12	5	15	0.0625	1.6
13	5	20	0.04	1.384
14	10	5	0.4444	3.133
15	10	10	0.25	2.2
16	10	15	0.16	1.768
17	10	20	0.1111	1.533
18	20	10	0.4444	2.06667
19	20	20	0.25	1.6
20	20	30	0.16	1.384
21	20	50	0.0816	1.2
22	30	10	0.5625	1.9
23	30	20	0.36	1.576
24	30	30	0.25	1.4
25	30	50	0.140625	1.225

Although it is possible to determine surface roughness with the presence of nanostructures, existing models vary widely and are determined empirically. For this experiment, surface roughness trends were only analyzed for the microstructure data. Later chapters of this thesis take the nanostructured roughness into account as well. Both wetting models showed a positive trend with contact angle increasing as surface roughness increased (Figure 21 and Figure 22).

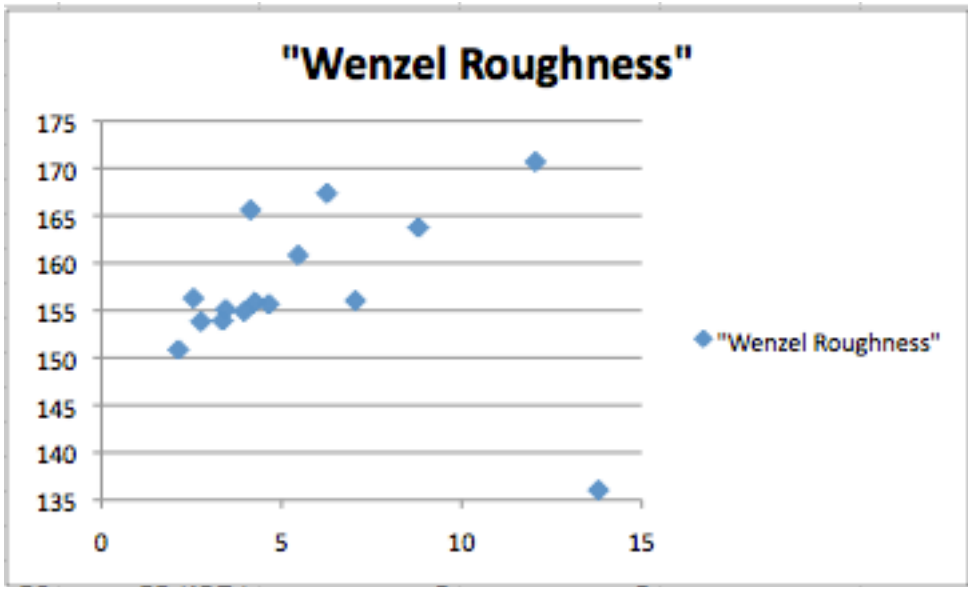

Figure 21: Wenzel Surface Roughness parameter vs. Contact angle for microstructured surface.

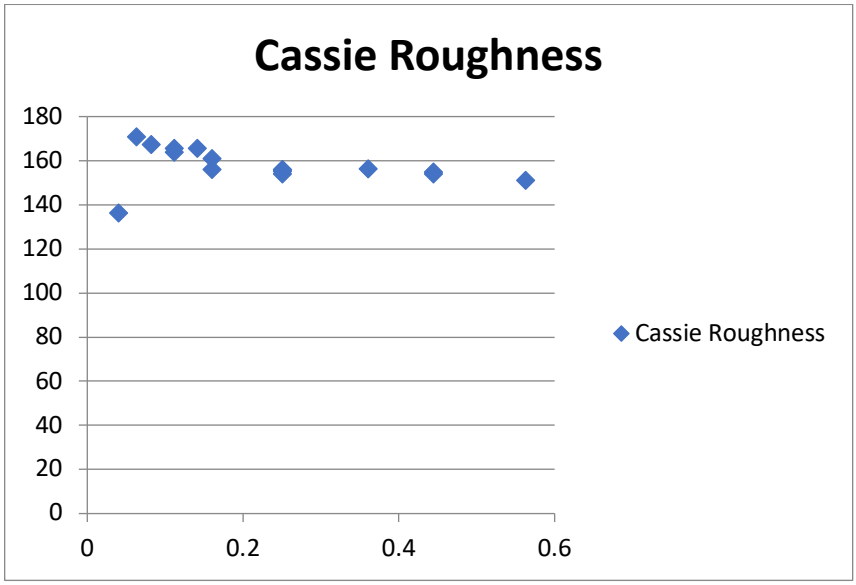

Figure 22: Cassie surface area fraction vs. Contact angle for microstructured surface.

As mentioned in the literature review, previous work on hierarchically structured surfaces with micropillar arrays found that not only high static contact angles but also low roll-off angles are often demonstrated by superhydrophobic surfaces. However, the structures measured in this experiment experienced a high amount of droplet pinning when tested for roll-off angle despite having superhydrophobic contact angles. It was assessed that due to the large nature of the microstructures and the 5 μL droplet size used for static contact angle measurements, a sagging mechanism ensued, causing the droplets to eventually wet the bottom of the microfeature gaps. Similar results were found

by Teisala et al., for varying nanoscale structures. They observed that varying the scale of the nanostructures — from hundreds of nanometers down to much smaller values — demonstrated different wetting and adhesion properties. Although surfaces all were found to be superhydrophobic based on contact angle measurement, adhesion was affected by the ability of the water to penetrate the nanopores on the substrate surface[59].

Specifically, this experiment found varying adhesion based on microstructure scale rather than nanostructure scale differences. The adhesion was caused by a partial wetting state characteristic of both Cassie–Baxter and Wenzel wetting. Droplets would partially penetrate the microstructured surface without fully wetting, creating a superhydrophobic effect but with high adhesion. The nanostructures increased the surface area contact available for water penetration, offering additional pinning effects as can be seen for pattern 21 in Figure 23.

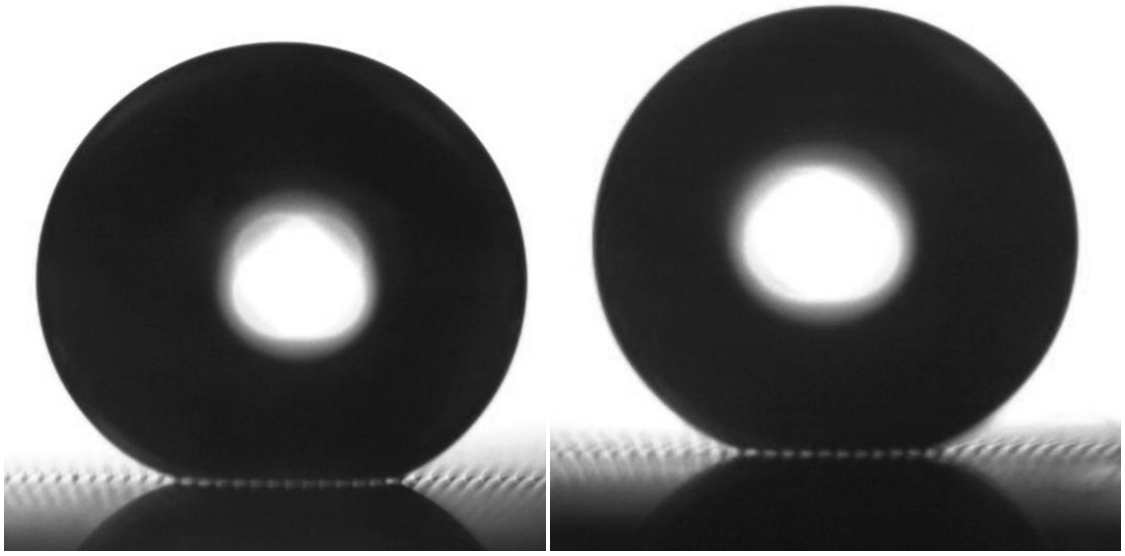

Figure 23: Pattern 21: (a) Microstructured surface with CA of 169° (b) Hierarchically structured surface with CA of 175°.

2.5 Conclusion and Future Work

In this report, microstructures composed of pillar arrays were examined for contact angle and droplet shedding properties. Microstructured samples and hierarchically structured samples with chemically induced nanopillars were compared. In addition to pillar arrays as potential solutions to condensation acceleration and droplet shedding on aluminum surfaces, microgrooves, inverted pillars (mesh-like structures), and chevron arrays are also of interest and were included in the original mask design for comparative purposes. However, those patterns will need to be characterized in future work.

It is also of interest to visualize and quantify how these test surfaces behave in a dynamically condensing environment. In the following chapters, samples were tested for

droplet shedding capability and condensation performance once contact angle and droplet roll-off angles were fully characterized. Little research has been performed to analyze dynamic condensation in a humid environment with varying air speeds, air temperatures, and coolant temperatures. It is of great interest to quantify how hierarchically structured samples behave in such conditions.

3 Chapter: Characterization and comparison of microdome and micropillar-patterned, hierarchical surfaces

After characterizing the static and dynamic measurements of assorted hierarchically structured aluminum samples with pillar microstructure geometry, the question arose of how to fabricate a curved microstructure geometry to more closely resemble nature's lotus leaf and whether or not the feature curvature would affect condensation and droplet shedding performance. A technique to produce microdome structures was developed and utilized for a full comparison of static, dynamic, and condensing behavior with the micropillar structures[71]. Masks were designed to directly compare the same ranges of feature size and gaps for both pillar and dome arrays, and similar fabrication processes were utilized to grow zinc oxide on the aluminum surface and render the surface hydrophobic through chemical functionalization. A better-performing surface with respect to static behavior was defined as having higher average static contact angle and lower contact angle hysteresis. In later chapters, a better-performing surface in condensation testing was defined as producing stable dropwise condensation as opposed to filmwise or flooded surfaces over long-term testing.

3.1 Background

Micropillars have been widely investigated and reported in the literature while very little research has been performed on evaluating microdomes, in particular, hierarchical microdomes on metal[36,47,57,58,72]. Micropillar geometries are easily fabricated using lithographic processes, as demonstrated in the previous chapter, and produce straight or scalloped sidewalls, depending on the DRIE depth, and the feature corners are often sharp. Pillar height, width, and spacing are also easily tunable based on the mask design, and much research has been performed to tune the wettability of surfaces with varying pillar arrays. In scaling processes or to fabricate such structures on metal, casting techniques, roll-to-roll embossing, and sputtering are some of the more commonly used methods. The drawbacks to all come with manufacturing complexity and higher cost – either upfront in the case of roll-to-roll or sustained with casting and sputtering. In addition, the sharp-cornered features of pillars provide a strong pinning force to any droplets that become large enough to sag or seep into the pores. Once pinned, the droplets are extremely difficult to shed and negate any advantage of having a microstructured surface to improve droplet shedding.

Despite a recent push to replicate lotus leaf geometry for superhydrophobicity,[59] curved microstructures or microdomes have not been investigated as thoroughly for heat transfer, wettability, or condensation applications. The typical use of dome fabrication is for optical microlenses in polymers rather than sheet metal. The investigation presented

here hypothesizes that the curvature of the dome features will result in a lesser pinning force for condensing droplets that will allow for droplet shedding at lower roll-off angles than pillar features of the same dimension and spacing (Figure 24).

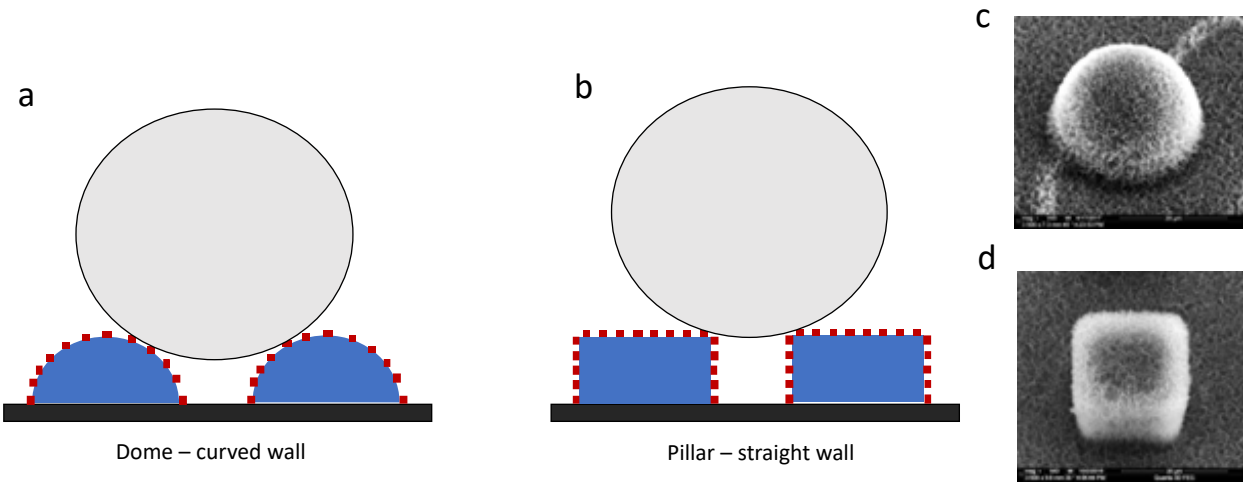

Figure 24: Inspired by the hierarchical topography of superhydrophobic lotus leaves, a, b) novel, water repellent surface with micro and nano hierarchical structures was designed and fabricated via a standard single-layer photolithography and a hydrothermal nanostructure synthesis. In static measurements, microdome and micropillar arrays both demonstrated droplet suspension on top of the features in a traditional Cassie–Baxter wetting mode. c, d) Nanostructures can be seen on SEM images of individual dome and pillar features to demonstrate structural hierarchy.

To directly compare the dome and pillar geometries, two masks (Figure 25 and Figure 26) employing 16 patterns were designed. One mask had varying arrays of square features while the other had circular features. Rows included size to gap ratios of 1:.5, 1:1, 1:1.5, and 1:2 while columns were based on the length dimension for the squares and the diameter dimension for the circles. These values were feature sizes of 20 μm, 30 μm, 40 μm, and 50 μm.

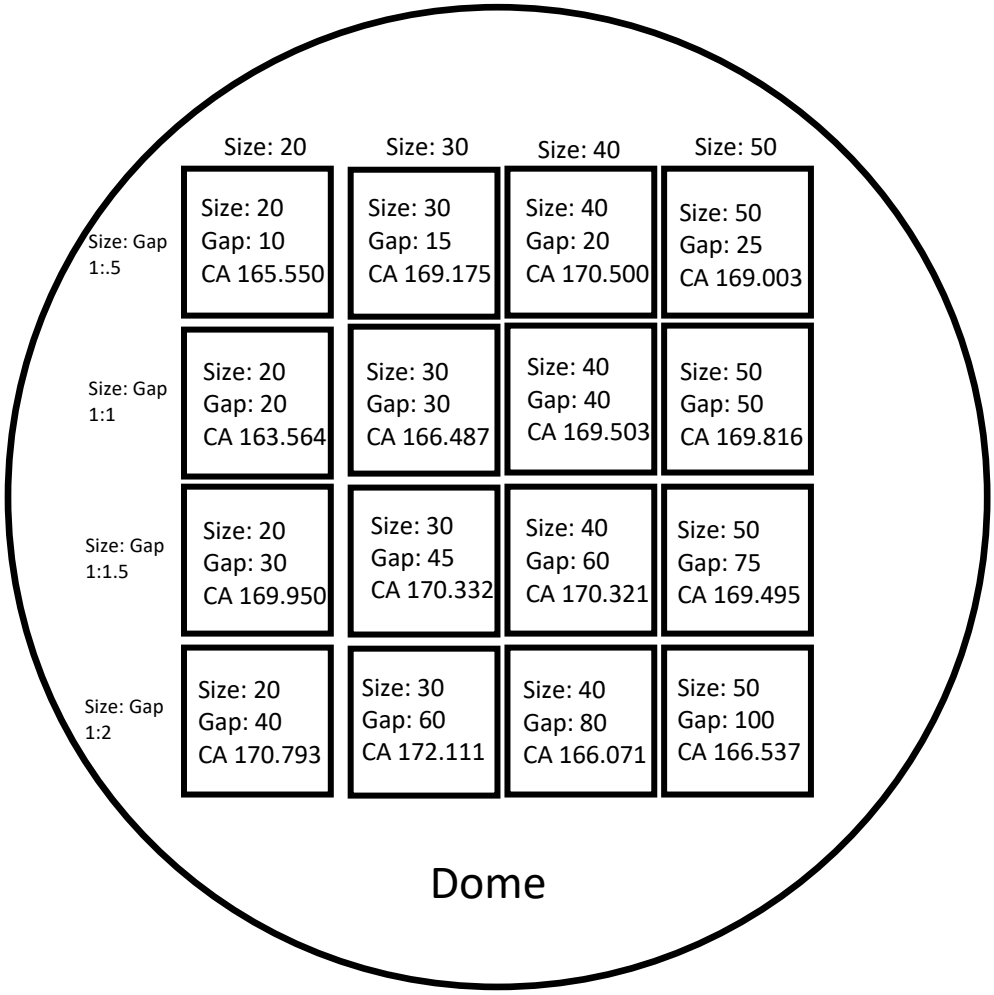

Figure 25: Mask layout and design for dome patterning with measured average static contact angles of samples with hierarchical roughness.

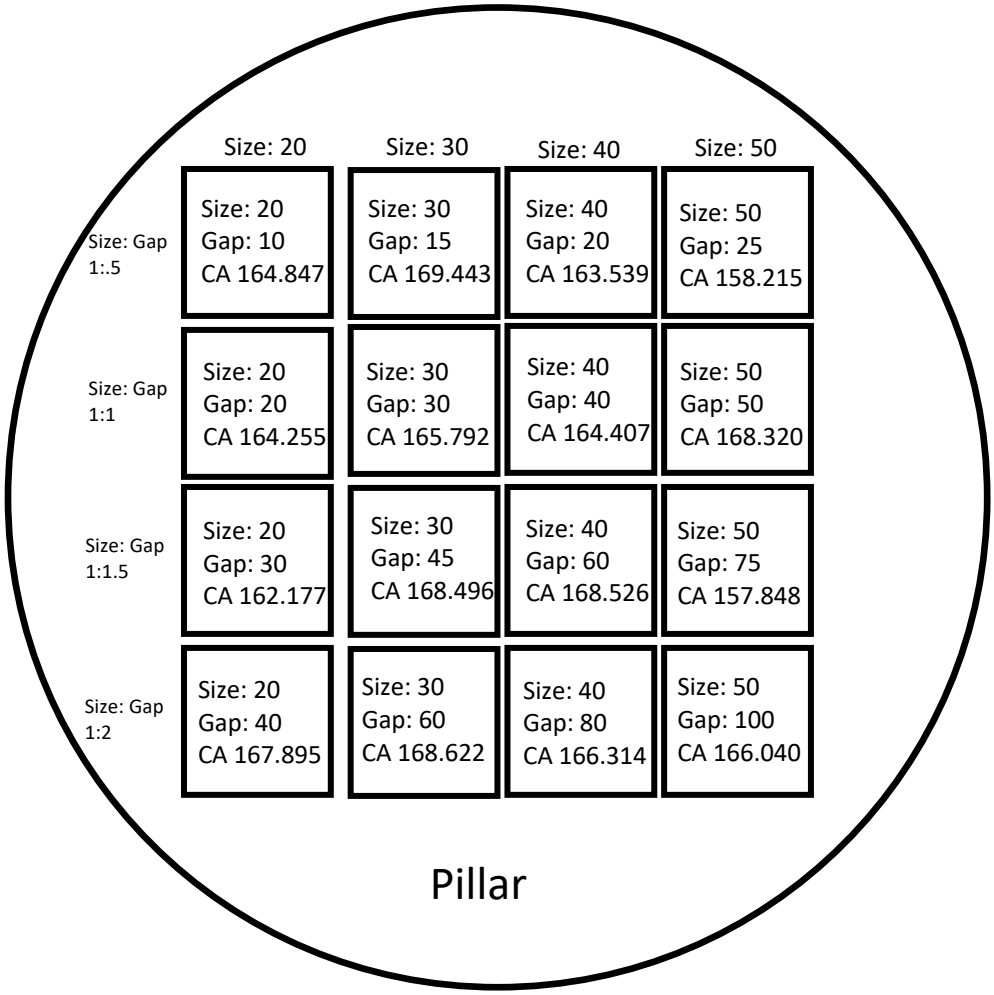

Figure 26: Mask layout and design for pillar patterning with measured average static contact angles of samples with hierarchical roughness.

3.2 Fabrication of Micropillar and Microdome Array

In order to directly compare dome and pillar feature surface wettability characterization for varying feature sizes and spacings, the micropillar and microdome arrays were fabricated via a standard, single-layer photolithography process. The process is detailed in Figure 27a and c. Prior to the microfabrication, two 4-inch silicon <100> wafers were cleaned by sonication in acetone and isopropanol followed by rinsing with deionized water and dehydrated at 150 °C for 15 minutes. Then, the fully dehydrated wafers were treated with an oxygen plasma at 70 W, 200 mTorr for 2 minutes. To improve adhesion between the photoresist and the substrate, an adhesion promoter, hexamethyldisilazane (HMDS, Sigma-Aldrich™) was vapor-phase coated onto the silicon

wafer for 5 minutes. The positive photoresist (PR), AZ P4620 (MICROPOSIT™), was spin-coated onto the silicon wafer by 300 rpm with a ramp of 50 rpm/s for 19 seconds, followed by 1000 rpm with 100 rpm/s for 39 seconds. The PR-coated sample was next soft baked at 90 °C for 30 minutes. To prevent cracking of the PR in subsequent steps, the wafer was placed in a dark room for 10 minutes with 30–50% RH. Following the rehydration step, the sample was exposed to a 1200 mJ/cm^2 UV light dose in a mask aligner and developed with 1-part AZ 400K:3-parts DI water by volume for 4 minutes. The developed PR pattern was rinsed with DI water and treated with oxygen plasma for 10 minutes to remove any residual resist. The remaining patterns for both wafers at this time were vertical-walled pillar features from the unexposed resist. Resist height was evaluated using a Dektak profilometer, and one wafer was kept for the vertical-pillar pattern array. For the dome pattern, an additional process step was added to reflow the photoresist by baking at 130 °C for 1 hour in order to obtain the array of the fully curved shapes. Heights for both the pillar and dome patterns were kept similar for comparative purposes. Results of the varying arrays, features sizes, and ZnO nanostructure coatings are shown in Figure 27b–g.

A double-replica process of the micropillar and microdome wafers was then performed using a standard polydimethylsiloxane (PDMS, Sylgard 184, Dow Corning™) mold–cast procedure. The first replica was made with a PDMS mold–cast process with a prepolymer-to-crosslinker mixing ratio of 5:1 (Mold: Patterned wafer; Cast: PDMS 5:1). The second replica was then made with the same method with the mixing ratio of 10:1 (Mold: the first PDMS 5:1 replica; Cast: PDMS 10:1).

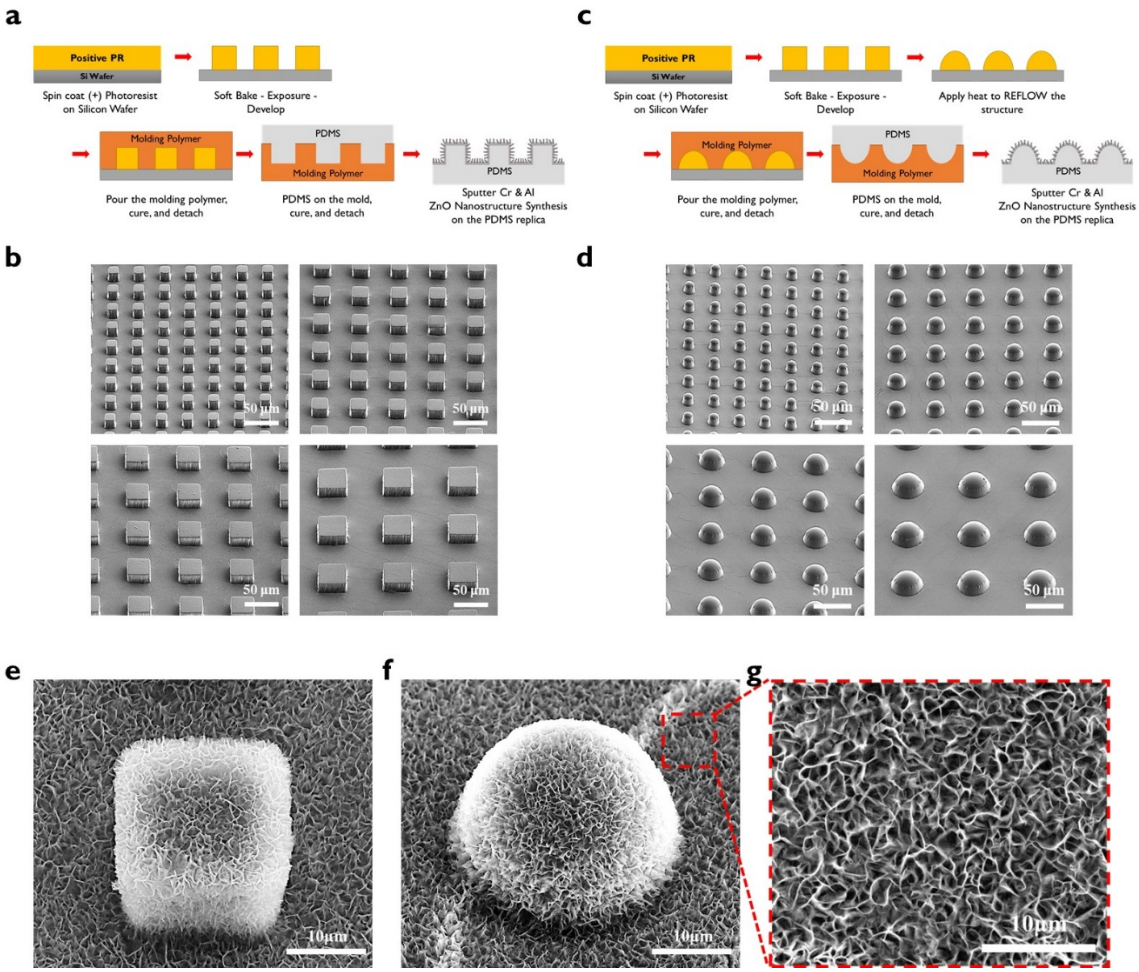

Figure 27: Fabrication of the hierarchically structured surfaces and surface morphology characterization (a) Schematic of the micropillar array fabrication (The molding polymer was PDMS with mixing ratio of 5:1); (b) Scanning electron microscope (SEM) images showing various sizes of the micropillar array: (Top-Left) Size:gap = 20 μm:20 μm, (Top-Right) Size:gap = 30 μm:30 μm, (Bottom-Left) Size:gap = 40 μm:40 μm, (Bottom-Right) Size:gap = 50 μm:50 μm; scale bar is 50 μm; (c) Schematic of the microdome array fabrication (The molding polymer was PDMS with a mixing ratio of 5:1); (d) Scanning electron microscope (SEM) images showing various sizes of the microdome array: (Top-Left) Diameter:gap = 20 μm:20 μm, (Top-Right) Diameter:gap = 30 μm:30 μm, (Bottom-Left) Diameter:gap = 40 μm:40 μm, (Bottom-Right) Diameter:gap = 50 μm:50 μm (Scale Bar is 50 μm); (e,f) Scanning electron microscope (SEM) images of the hierarchical structures (Left-Pillar, Right-Dome) with micro and nano roughness; (g) Enlarged view of the ZnO nanoporous structure (scale bar is 10 μm).

3.3 ZnO synthesis

After successful fabrication of the PDMS molds for the microstructured patterns, the samples were sputtered with a 10 nm layer of Cr followed by a 150 nm layer of Aluminum 99.999% as a seed layer for the next synthesis step. The aluminum-coated

PDMS was then treated in an aqueous solution of 25 mM zinc nitrate ($(Zn(NO_3)_2 \cdot 6 H_2O$, Sigma-Aldrich™) and hexamine (Hexamethylenetetramine, Sigma-Aldrich™) at 70°C for 90 minutes in a thermal oven chamber. Samples were placed vertically to avoid contact with excess precipitate and to ensure a conformal, uniform ZnO nanowire growth[73]. Following the bath synthesis, samples were rinsed with DI water and dried with N_2. Samples were left in a fume hood for 24 hours to completely dry.

In order to achieve superhydrophobicity of the surface, a chemical vapor deposition process was used. Any residual organic material on the sample surfaces was removed using a RIE chamber for an oxygen plasma treatment (60 W, 200 mTorr, 2 min). The cleaned substrates were then immediately placed in a vacuum desiccator with 100 µL of perfluorosilane (1H,1H,2H,2H-Perfluorooctyltrichlorosilane, Sigma Aldrich) with a 20-minute pumpdown and 40-minute rest period. Samples were then rinsed with DI water and allowed to dry and anneal at room temperature in a fume hood for 24 hours.

The results of the zinc oxide synthesis process were characterized using X-ray photon spectroscopy (XPS), shown in Figure 28, to confirm successful coating of the zinc oxide on the aluminum surface. Based on analysis of a sample of a ‘flat’ zinc oxide case with no microstructures, several zinc and oxygen orbital peaks can be observed. The peaks refer to the y-axis, which is the number of electrons detected (or count) per unit time in seconds. The x-axis is the binding energy of the electrons detected. In this case, the most prominent peaks for the zinc are the Zn2p1 and Zn2p3 orbitals. The next most prominent peak is O1s which refers to oxygen. Toward the bottom right of the graph, more trace amounts of carbon and aluminum can be observed, including C1s, Al2s, and Al2p. This aligns with the fact that the zinc oxide was grown on aluminum and trace amounts of atmospheric carbon are usually identifiable in XPS readings.

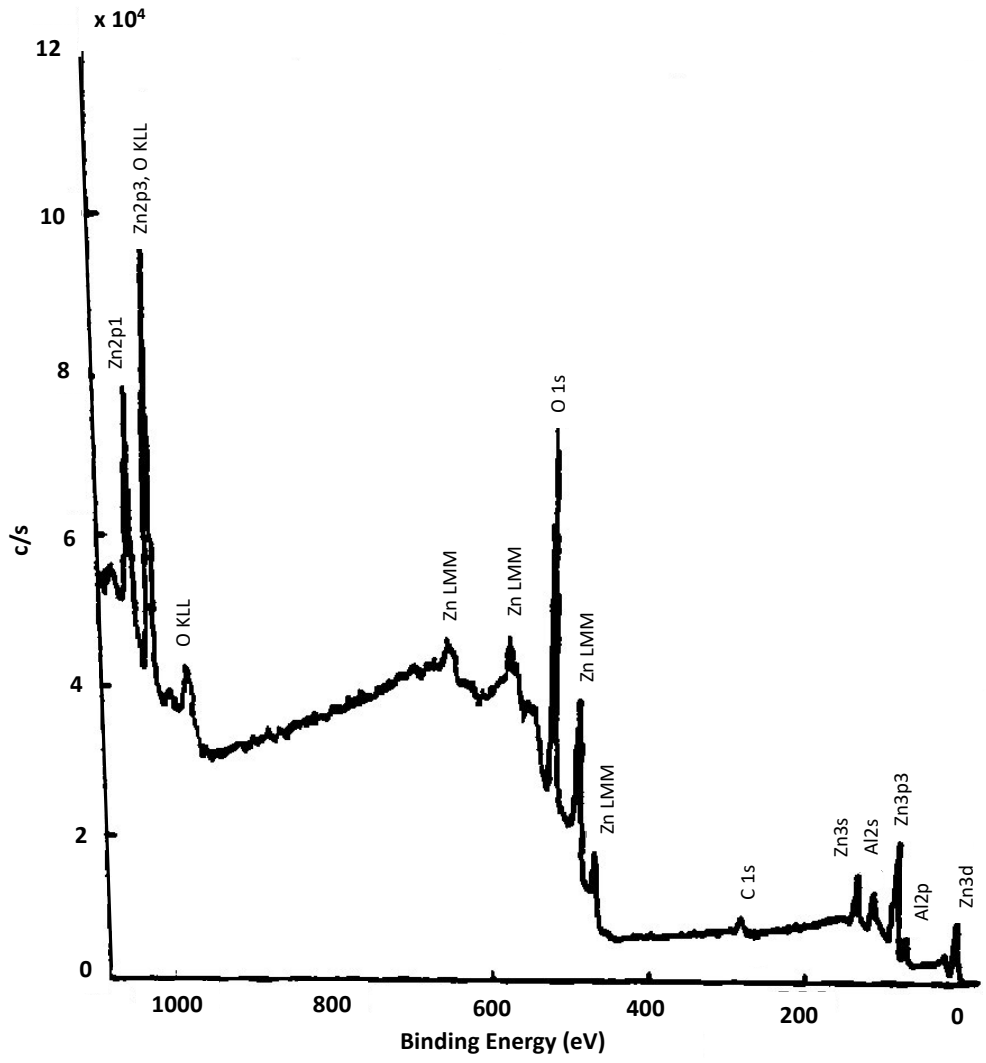

Figure 28: XPS characterization of ZnO surface.

3.4 Characterization

Because the microdome features were neither ideal spherical caps nor oblate or prolate spheroids, a more in-depth method was needed to calculate the exact feature surface area. These calculations were critical for later determining wetted surface area in the Cassie–Baxter and Wenzel wetting formulations as well as for comparing wetted surface areas between the dome and pillar geometries. Exact height and diameter measurements were obtained from SEM imaging shown in Figure 29.

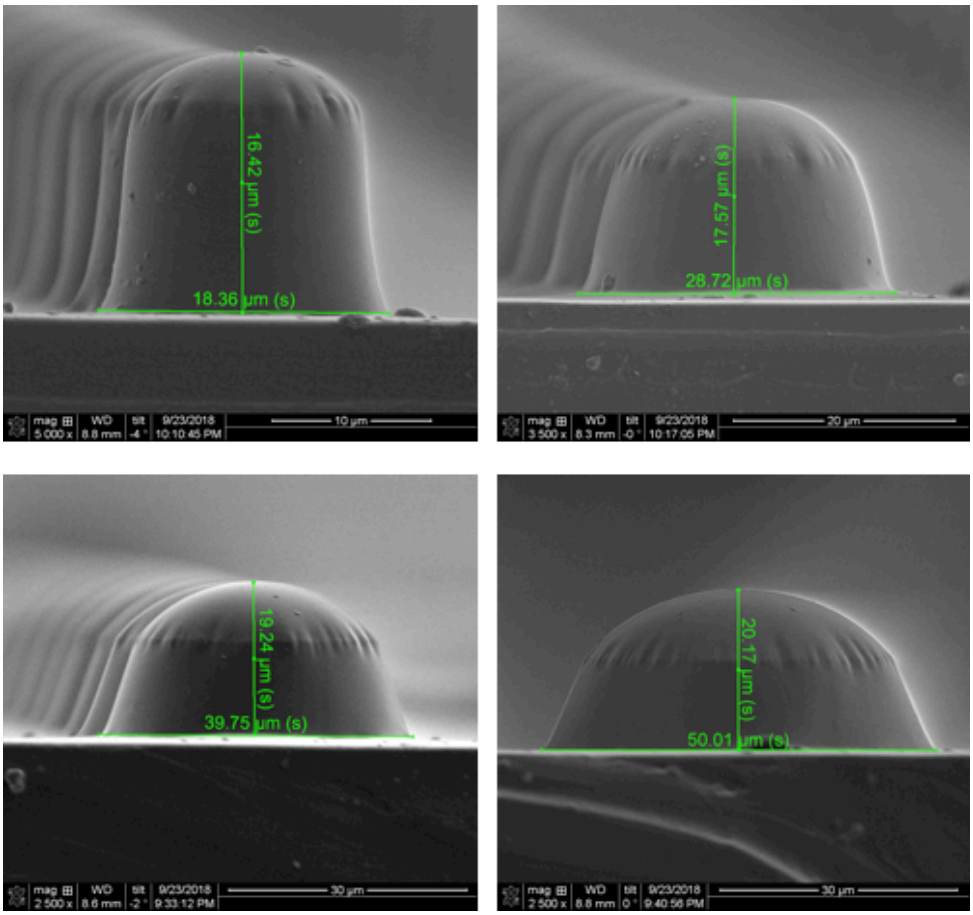

Figure 29: SEM of individual domes for height and diameter characterization.

It can be observed that there is a slight wrinkle or deviation in the curvature part way down the dome feature. This artifact is due to the reflow process in which the resist forming the circular pillars is partially melted but the base of the feature is thought to be 'locked' into place by bonding with an HMDS layer during the fabrication process. The two regions, considered the cap and base, were approximated with different ellipses in the 2-D images and modeled as oblate spheroids to calculate total surface area. In addition, a 'touching point' — the point at which a droplet suspended on the surface features would rest at the equilibrium static contact angle on the dome — needed to be determined for wetted area calculation (Figure 30). The following assumptions were made:

- Shape for patterns follows an elliptical cross-section of a spheroid with radius of curvature at the touching point, ρ.

- The spheroid approximations were oblate or prolate depending on the dome feature diameter and height.

- For the local contact angle at the touching point, it was assumed that the contact angle would be the contact angle of the purely nanostructured ZnO surface: $\theta_{CA} \approx 157°$. The touching point is designated as (x, y).
- $a = radius\ of\ dome$ and $c = height\ of\ dome$
- $\theta c = 180 - \theta_{CA}$

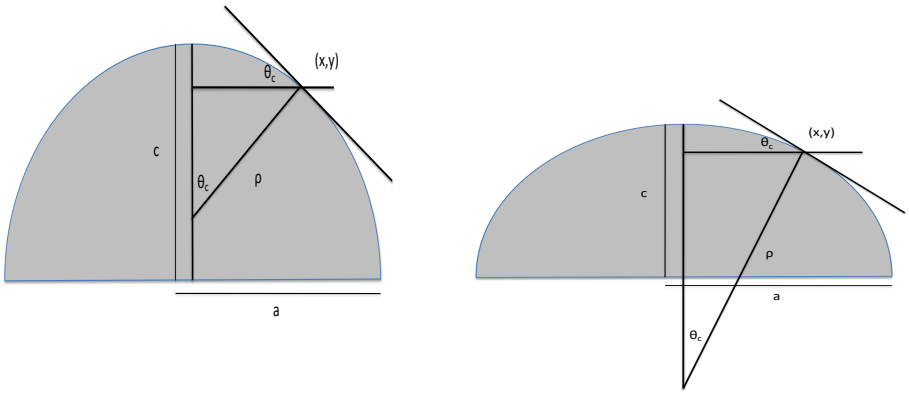

Figure 30: Schematic of static droplet contact point on a dome feature based on the feature radius of curvature which can be treated as a prolate spheroid on the left or as an oblate spheroid on the right.

Variables used are in Table 4 below.

Table 4: Feature surface area characterization variables.

c	Feature height in microns
θ	Recorded static contact angle
g	Space between features
d	Pattern diameter for dome
a_{pillar}	Feature length, or width, for pillar geometry
b	Pitch of cell, corresponding to feature length dimension + gap

a_{dome}	$\frac{d}{2}$ = radius of dome
θ_{comp}	$180 - \theta$
h	Vertical distance from contact point *y* to top of dome
e	Eccentricity for surface area
e_1	Secondary eccentricity for surface area
A_{cap}	Surface area of the wetted spheroidal cap
A_{cell}	Projected area of dome and adjacent area in one unit cell, as illustrated in Figure 31
A_{base}	Area of flat region between features in one unit cell
A_{dome}	Full feature surface area
A_{total}	$A_{dome} + A_{base}$

Specifically, for the surface area of the cap, relationships for describing the touching point or point of contact with a suspended water droplet are:

$$e = \sqrt{1 - \frac{a^2}{c^2}} \quad (9)$$

$$e_1 = e\left(1 - \frac{h}{c}\right) \quad (10)$$

$$A_{cap} = \pi ac\left\{\frac{(sin^{-1}e - sin^{-1}e_1)}{e} + \frac{a}{c} - \left(1 - \frac{h}{c}\right)\sqrt{1 - e_1^2}\right\} \quad (11)$$

$$A_{dome} = \pi ac\left\{\frac{(sin^{-1}e)}{e} + \frac{a}{c}\right\} \quad (12)$$

$$A_{cell} = (2a + g)^2 \quad (13)$$

$$A_{base} = A_{cell} - \pi a^2 \quad (14)$$

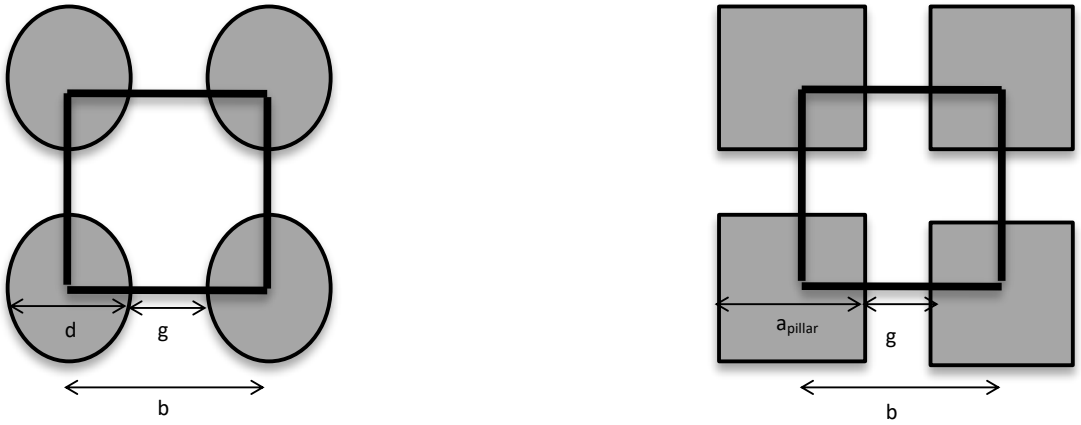

Figure 31: Schematic of unit cell definitions for dome and pillar pattern arrays, for which the unit cell area corresponds to (the nominal feature length plus gap size) squared.

For a dome of diameter *d*, the point of contact is defined as being at (x, y) with a radius of curvature of ρ and, most importantly, a wetted surface area (A_{cap}) corresponding to the area seen by a droplet for later implementation in an expanded Cassie–Baxter formulation. The full feature area was determined by adding the wetted cap area to an additional spheroid calculation performed for the bottom portion of the dome. It is interesting to note that the larger diameter domes have significantly higher wetted surface area for a droplet suspended on the surface. Additionally, for the larger features, which have a lower curvature or higher radius of curvature and are spaced further apart, the hydrostatic pressure needed to overcome the Laplace pressure is lower, and thus the droplet more readily begins to seep into the pores.

Table 5: Total feature surface area and wetted cap surface area for dome features.

Diameter (μm)	Height (μm)	Radius (μm)	ρ, radius of curvature (μm)	Wetted cap surface area (μm^2)	Total feature surface area (μm^2)
20	16.42	9.18	6.240	39.204	814.131
30	17.57	14.36	13.084	69.124	1380.00
40	19.24	19.875	21.547	144.174	2088.24
50	20.17	25.005	31.184	261.165	2911.99

The equivalent wetted and total surface area calculations were much simpler for the pillar cases due to straightforward geometry. Also, using scanning electron microscope (SEM) imaging, the actual feature heights and side lengths were determined. These measurements were important because they differed from the nominal mask values, which were used for the unit cell calculations (Figure 31).

Table 6: Total feature surface area and wetted top surface area for pillar features.

Nominal length (μm)	Actual length (μm)	Height (μm)	Wetted top area (μm^2)	Total feature surface area (μm^2)
20	14.65	16.75	214.623	1196.173
30	24.57	16.75	603.685	2249.875
40	33.99	16.75	1155.320	3432.650
50	42.46	16.75	1785.908	4617.328

It is particularly interesting to note that the wetted top areas and total feature surface areas are significantly greater for all of the pillar patterns compared to the dome patterns as shown in Table 5 and Table 6. Thus, a droplet wetting a given projected area would see much greater surface roughness for pillars. While increased surface roughness is generally indicative of higher contact angles and improved hydrophobicity, it does not necessarily bode well for droplet shedding capability. The higher curvature at the corners of the pillar features is likely to yield a higher Laplace pressure for any droplets that become pinned in the feature gaps.

3.5 Static and Dynamic Contact Angle Measurement

After characterizing the structures themselves, the static water contact angles and contact angle hysteresis were determined using a custom-built goniometer and open-source image analysis software. Five droplets (7.5 μL) were deposited onto different parts of the substrate surface using a silanized needle and microsyringe. Images were captured using a Thorlabs CMOS image sensor coupled to an objective lens, and were analyzed for contact angle values using the ImageJ software and the available plug-in LB-ADSA[74]. For symmetric droplets, the software approximates the droplet curve and contact angle values based on fitting the Young–Laplace equation to the image data. Contact angle hysteresis, including the advancing and receding water droplet contact angles, was determined by both a tilting-cradle method and droplet inflation method. For the tilting cradle method, a water droplet (7.5 μL) was deposited on the substrate surface. The sample stage was then incrementally tilted until incipient rolling motion of the droplet was detected. The angle of tilt was taken to correspond to the droplet hysteresis value. Alternatively, a droplet inflation method was also utilized. A droplet was incrementally inflated in volume up to 10 μL volume and then deflated to achieve advancing and receding contact angles through video recording of the process.

3.6 Results and Discussion

The initial baseline ZnO nanostructured surface resulted in an average contact angle of approximately 157°. This value is worth noting because it is significantly less than the contact angle results from the micropillar characterization in Chapter 2. Although SEM images of both growth cases exhibit similar porosity and appearance, the presence of the PDMS is the primary distinguishing factor between the sample sets and most likely contributed to the lower static contact angle results. However, because these experiments

were comparatively performed, the ~157° 'flat'-case contact angle serves as the baseline for the microdome and micropillar performance evaluation.

3.6.1 Theoretical Calculation and Results

The theoretical calculation of droplet angles on the hierarchical surfaces was performed using an expanded Cassie–Baxter model, taking into account the nanoscale roughness of the ZnO nanowires in addition to the microscale roughness of the pillar and dome features[75]. In order to expand the formula for the different contact areas and regions of the surface — both with respect to the surface and trapped air within the feature pores — the apparent contact angle for a silanized, nanoscale ZnO surface was determined experimentally from averaging a set of five water contact angle measurements. This value, which, based on wetting theory, should be within the range of the substrate advancing and receding contact angle values, was used as the surface baseline value, θ^*_{nano}. The Cassie–Baxter formula was then utilized with roughness coefficients and proportionalities determined by the specific geometries of the nanostructured and microstructured patterns for the dome and pillar surfaces respectively with nanoscale variables defined in Table 7, nano and microscale variables defined in Table 8, and model coefficients defined in Table 9.

$$\cos\theta^* = \Sigma\phi_i r_i \cos\theta_i \quad (15)$$

$$= \phi_m r_{mt} \cos\theta^*_{nano} + (1-\phi_m)\left[\phi_{fm} r_{mp} \cos\theta^*_{nano} - \left(1-\phi_{fm}\right)\right] \quad (16)$$

$$\cos\theta^*_{nano} = \Phi_{tn}\cos\theta_0 + (1-\Phi_{tn})[\Phi_f r_n \cos\theta_0 - \left(1-\Phi_f\right)] \quad (17)$$

$$\cos\theta^*_{nano} = \Phi_{tn}\cos\theta_0 + (1-\Phi_{tn})\cos\theta^*_{nanopore} \quad (18)$$

where

$$\cos\theta^*_{nanopore} = \Phi_f r_n \cos\theta_0 - \left(1-\Phi_f\right) \quad (19)$$

Table 7: Variables for nanoscale Cassie–Baxter model.

$\Phi_f r_n = A_{SL}$	Areal ratio of solid–liquid interface
$1-\Phi_f = A_{LV}$	Areal ratio of liquid–gas interface
Φ_f	Fraction of nanopores filled

Φ_{tn}	Nanotips area fraction
r_n	Roughness of nanostructures outside of Φ_{tn}

$\cos\theta^*_{nanopore}$ is the apparent contact angle associated with the nanopore geometry. $\cos\theta_0$ is the measured contact angle on a baseline smooth surface of the same chemical functionalization. In the case of the $\cos\theta^*_{nano}$, $\cos\theta_0$corresponds to a smooth, silanized aluminum surface with no nanostructures.

Once the nanopore contribution was determined, $\cos\theta^*_{nano}$ was calculated by summing the contributions of the respective fractions of the wetted areas or tips of the nanostructures and nanopores of the nanostructured surface.

Variables:

Table 8: Nano and microscale general variable definitions for Cassie–Baxter expanded model.

θ_0	Contact angle on flat surface of same chemical functionalization
Φ_f	Fraction of nanopores filled
r	Roughness of nanostructures outside Φ_{tn}
Φ_{tn}	Nanostructure tip area fraction
r_{mt}	Microstructure roughness (wetted region of tip touching the droplet, corresponding to actual wetted touching area on top/projected wetted touching area on top)
r_{mp}	Microstructure roughness (wetted region within pore, corresponding to actual wetted touching area in pore/projected wetted touching area in pore)
Φ_{fm}	Proportion of microstructures in Wenzel mode (0 or 1 value)
Φ_m	Wetted area fraction of microstructure protrusion, corresponding to wetted touching top area/unit cell area

For the ZnO growth conditions of 70 °C, 90 min, 25 mM from Brockway and Taylor[73], the fractions of the nanotip and nanopore contributions were determined from statistical modeling of empirical data.

Table 9: Nanoscale coefficients statistically determined for the ZnO nanowire surface used in this Cassie–Baxter expanded model.

θ_0	$105.0°$ (CA on flat surface of same chemistry)
Φ_f	$.018606$ (fraction of nanopores filled from original model)
r	3.5 (roughness of nanostructures outside Φ_{tn})
Φ_{tn}	$.0051$ (nanostructure tip area fraction)
Ψ_0	$51°$ (mean reentrant angle)
σ_0	$25.0°$ (standard deviation)

Microscale Variables:

The microscale variables were defined as in Table 10 below.

Table 10: Microscale variable definitions more specifically defined for pillar and dome geometries.

r_{mt}	Microstructure roughness (top touching point part) which corresponds to the actual wetted touching area on top divided by the projected wetted touching area on top. Using this definition, r_{mt} is equal to 1 for the pillar and is greater than 1 for the dome.
r_{mp}	The microstructure roughness for the region within the pores. This corresponds to the actual wetted touching area in the pore divided by the projected wetted touching area in the pore.
ϕ_{fm}	The proportion of microstructures in Wenzel mode.
ϕ_m	The wetted area fraction of the microstructure protrusion corresponding to the wetted touching top area divided by the unit cell area, where the unit cell is previously defined.

In calculating the theoretical static contact angles for each of the patterned surfaces, the wetted and total surface area values previously determined using the measurements taken directly from SEM images, shown in Figure 32e–f, were used to evaluate each of the respective roughness factors and proportionality constants associated with the microscale features. It was also assumed that ϕ_{fm} was zero, which would correspond to the case of the proportion of microstructures being completely in Cassie–Baxter mode rather than Wenzel.

For the individual microstructures, slightly different unit cell and fraction definitions were used.

For domes:

Unit cell:

Table 11: Microscale Cassie–Baxter model variable definitions for dome structures.

A_{cell}	$(2r+g)^2$
A_{total}	$A_{dome} + (2r+g)^2 - \pi r^2$
r_{mt}	$\frac{A_{cap}}{(\pi * cap\ radius)^2}$
r_{mp}	$\frac{A_{total} - A_{cap}}{A_{cell} - (\pi * cap\ radius)^2}$
Φ_m	Protrusion area fraction of microstructures $= \frac{A_{cap}}{A_{cell}}$
Φ_{fm}	Observed fraction based on estimated pores in Wenzel mode (0 or 1 value)

For pillars:

Unit cell:

Table 12: Microscale Cassie–Baxter model variable definitions for pillar structures.

b	$length + gap$, which is the same as the pitch
A_{cell}	b^2, which is the same as the projected area

A_{base}	$A_{cell} - length^2$
r_{mt}	1
r_{mp}	$\frac{4 * length * height + bottom}{bottom}$
Φ_m	Protrusion area fraction of microstructures $= \frac{SA_{cap}}{unit\ cell}$
Φ_{fm}	Observed fraction based on estimated pores in Wenzel mode (0 or 1 value)

3.6.2 Experimental Results and Discussion

The values used for the theoretical and measured plots in Figure 32a–d are listed in Table 13 for the microdome samples and Table 14 for the micropillar samples. A ratio between the measured and predicted values was calculated to determine if the offset between the model and experiments was consistent for all samples.

For the Dome features:

Table 13: Calculated Cassie–Baxter model values and experimentally determined static contact angles for the microdome array pattern of the hierarchical surfaces.

Mask Number	Size:Gap	Model CA Value	Measured CA Value	$\frac{\cos(model\ value)}{\cos(measured\ value)}$
1	20-10	177.5774	165.55	1.031744684
2	20-20	178.1831	163.564	1.042080425
3	20-30	178.5465	169.95	1.015256497
4	20-40	178.7888	170.793	1.012825075
5	30-15	176.5488	169.175	1.016270564
6	30-30	177.4118	166.487	1.02742209
7	30-45	177.9295	170.332	1.013744924
8	30-60	178.2746	172.111	1.009096872
9	40-20	175.6225	170.5	1.010947337
10	40-40	176.7473	169.503	1.015381976
11	40-60	177.3979	170.321	1.013394416
12	40-80	177.8317	166.071	1.029558407

13	50-25	174.9035	169.003	1.014678866
14	50-50	176.1781	169.816	1.013747636
15	50-75	176.9427	169.495	1.015599152
16	50-100	177.4524	166.537	1.027239703

The average ratio of $\frac{\cos(model\ value)}{\cos(measured\ value)}$ was 1.019311 and the standard deviation was .009296402.

For the Pillar features:

Table 14: Calculated Cassie–Baxter model values and experimentally determined static contact angles for the micropillar array pattern of the hierarchical surfaces.

Mask Number	Size:Gap	Program CA Value	Measured CA Value	$\frac{\cos(model\ value)}{\cos(measured\ value)}$
1	20-10	163.23	164.847	0.9919599144
2	20-20	167.4422	164.255	1.014128357
3	20-30	169.961	162.177	1.034330355
4	20-40	171.6375	167.895	1.011866647
5	30-15	163.23	169.443	0.9739567459
6	30-30	167.4422	165.792	1.006876419
7	30-45	169.961	168.496	1.004876508
8	30-60	171.6375	168.622	1.009201573
9	40-20	163.23	163.539	0.9983919581
10	40-40	167.4422	164.407	1.013373975
11	40-60	169.961	168.526	1.004769572
12	40-80	171.6375	166.314	1.018279789
13	50-25	163.23	158.215	1.031109425
14	50-50	167.4422	168.32	0.9967156211
15	50-75	169.961	157.848	1.063164933
16	50-100	171.6375	166.04	1.019478663

The average ratio of $\frac{\cos(model\ value)}{\cos(measured\ value)}$ was 1.012030029 and the standard deviation was .01998040.

With very low standard deviations for both the pillar and dome contact angle data sets, the average ratio comparing the expanded Cassie–Baxter model formulation to the measured values was the same to three significant figures, 1.01, for both. Although this indicates a shortcoming in the Cassie–Baxter model assumptions, it also suggests a multiplicative factor or coefficient that can be used to achieve a correct predicted contact angle for hierarchically structured surfaces.

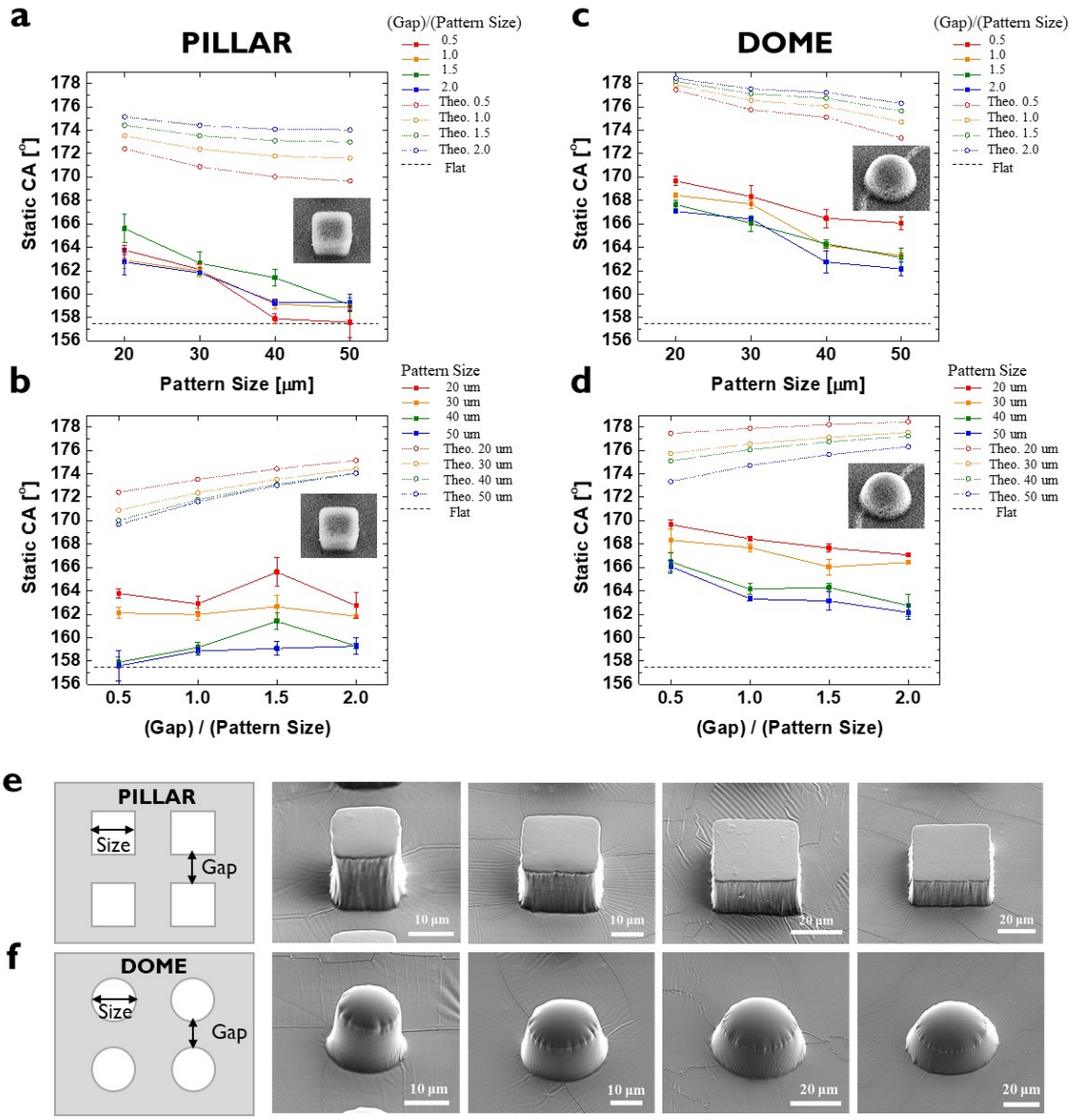

Figure 32: Theoretical and experimental water sessile contact angle distribution of various pattern sizes and spacings, and comparison between micropillars and microdomes. (a) Plot of water contact angle (CA) versus the micropillar pattern size (i.e. square width of the top surface). Solid lines are experimental measurements and dotted lines are theoretical calculation using the Cassie–Baxter model. (b) Plot of water CA versus the ratio of the gap to micropillar pattern size. (c) Plot of water contact angle (CA) versus the microdome pattern size (i.e. circular diameter of the bottom surface). (d) Plot of water CA versus the ratio of the gap to microdome pattern size. (All

the samples are the hierarchical surfaces with micro and nanostructure roughness, while the "Flat" means the sample with the ZnO nanoporous structure on a surface with no microstructures) (e) Scanning electron microscope images of the of micropillar with various sizes. From left to right, the pattern sizes (i.e. square width of the top surface) were 20, 30, 40, 50 μm, with the uniform average height of 16.75 μm (f) Scanning electron microscope images of the microdome with various sizes. From left to right, the pattern diameters (i.e. circular diameter of the bottom surface) were 20, 30, 40, 50 μm, with the average center heights of 16.52, 17.57, 19.88, 25.01 μm, and the radii of curvature of the apex were 9.02, 12.52, 18.16, 25.39 μm. (For all plots, the error bars represent ± one standard error of the mean, and the sample size is five separate droplets per specimen.)

In more detailed discussion of the physical results, all surfaces were found to be superhydrophobic. The dome-shaped structures had higher average static contact angles than the rectangular pillars by approximately 6° for every size-and-gap combination. Based on the Cassie–Baxter model, the introduction of surface roughness increases the apparent contact angle because the fraction of solid surface area which is in contact with water relative to the actual area, ϕ_i, decreases as surface roughness increases in the equation. Experimental observation showed the clear increase in both the dome and the pillar contact angles compared to the flat case.

From the 16 different array patterns characterized, the static contact angle measurements for the dome and pillar patterns both had a decreasing trend as the ratio of gap to pattern size increased as shown in Figure 32b and d. The dome pattern also exhibited a decreasing trend as the ratio of gap to pattern size increased. This indicates that the smallest pattern size as well as smallest gap to pattern size ratio had the overall highest contact angle for the dome. The calculated theoretical values using an expanded Cassie–Baxter model also followed the same trend for increasing pattern size with respect to the contact angles.

However, the Cassie–Baxter formula alone was not able to explain why the microdomes had higher CA values than the micropillar arrays. As shown in Figure 32, the averaged apparent static contact angle measurements for the microdomes were higher than the pillar patterns of the same feature size. A possible physical explanation could be related to the droplet's equilibrium position on the dome's curved shape, for reference, individual features are shown in Figure 32e and f. When a droplet was gently placed and released to perform a static contact angle measurement, the droplet followed the contour of the curvature due to its weight until it reached a force balance. The pillar structures have inherent discontinuities at the corners of the features and did not exhibit the same force balance equilibrium or contact line as the dome structures. In addition, the droplet balanced on the curved surface caused the dome's static contact angle to be similar to the advancing contact angle mode of the flat surface, approximately 173°, making it the most superhydrophobic of the tested samples.

In addition, a consideration when comparing varying pattern and spacing sizes was the overall pattern density per wetted portion of the surface. Due to the constrained droplet size of 7.5 μm, the number of patterns in contact with the droplet lessened as the

pattern gap increased, yielding contact angle measurements approaching the purely nanoscale or 'flat,' non-microstructured surface case. This was most evident with the larger pillar patterns which approached the flat surface control case for the 40 and 50 μm patterns. Although the Cassie–Baxter model was able to predict the trend direction of the static contact angle values correctly for the dome and pillar when pattern size served as the independent variable, it was not able to correlate well with the observed static contact angle values graphed against the gap to pattern size ratio. Contact angles were higher with decreasing pattern size, as was also shown in Figure 32a and c; however, increasing gap-to-pattern-size ratio showed a decrease in contact angle while the model predicted an increase. This discrepancy is best explained by the previously mentioned lower pattern density for correspondingly larger gap sizes. The total contact area is still predicted based on the assumption of a fully suspended droplet state over a lower apparent surface contact area. Both the pillar and the dome features showed the observed decreasing contact angle trend. The apparent contact angle was averaged over five measurements and was found to be approaching the advancing angle case. The dome features, in every gap-to-pattern-size-ratio and pattern-size case, had higher observed and predicted contact angle values than the pillar structures.

3.7 Dynamic Contact Angle

Following the static contact angle measurements, the dynamic contact angle measurements for the dome and pillar patterns, shown in Figure 33, compared the advancing angles, receding angles, and hysteresis values for each of the dome and pillar patterns. Advancing angles for both geometries as well as the flat, purely nanostructured case were observed to be similar, around 170°. Interestingly, the receding angles for the dome cases were much higher than the flat and comparable pillar cases, suggesting that the inherent curvature of the features did help to prevent strong pinning within the microfeatures and allowed for easier droplet contour movement along the curved surface of the feature, similar to the advancing mode. The droplet on the pillar surface yielded contact angle measurements approaching the purely nanoscale or 'flat,' non-microstructured surface case, most evident in the larger pillar patterns in which overall pattern density per wetted portion of the surface decreased due to the constrained droplet size of 7.5 μL.

The higher receding angle was significant for the micro-dome array because it indicated that the contact angle hysteresis — which is representative of the energy required for the droplet to roll off the surface — was lower than that of either the pillar or the flat case. The receding angle for the pillar pattern approached the receding angle for the flat case. For a droplet completely wetting one of the feature gaps or pores between patterns, the energy needed to overcome the force associated with the pattern curvature would be lower for the dome than the pillar. This effect was observed in the significantly lower hysteresis values for all dome patterns when compared to the pillar structures despite similar advancing angles[15]. It was, therefore, easier for a droplet to roll off a dome-patterned surface.

In terms of contact angle hysteresis — the advancing angle minus the receding angle — the dome patterns had lower hysteresis than their corresponding pillar features shown in Figure 33. Both the dome and pillar cases had higher contact angle values and lower hysteresis when compared to the 'flat' nanostructure baseline case. Indeed, the dome patterns in general exhibited 10–15° lower contact angle hysteresis than their rectangular pillar counterparts. The more favorable, lower hysteresis of the dome structures is associated with the absence of sharp-edged corners in the structures to act as a pinning mechanism. Water was able to shed more effectively at lower roll-off angles due to the inherent curvature of the domes and less pinning on these structures compared to rectangular pillars. When compared with the purely nanostructured case, both the microdome and micropillar hierarchical patterns exhibited higher static contact angle performance. This can be explained by the classic Cassie–Baxter formulation in which increasing surface roughness enhances the apparent contact angle and wettability characteristics of a given surface. The overall surface roughness is greatly increased by the presence of the greater number of features. In addition, the smaller gap size of the dome patterns would indicate that there is a larger number of features per unit area than for a larger gap size sample. This would increase the apparent surface roughness from the perspective of a droplet. The performance of the pillar static contact angles did not vary significantly based on gap size.

In comparing hysteresis values with respect to gap size, the dome structures had lower hysteresis values across all gap sizes when compared with the pillar structures. As the spacing increased for the dome patterns, the hysteresis increased due to the likelihood of the droplet forming capillary bridges with the curved side of the features closer to the base of the pore[76]. The receding angle would need to overcome a larger surface area than for the smaller domes. The pillar patterns did not have an apparent trend for hysteresis relative to gap size. However, hysteresis values were high for all samples. Due to the sharp-cornered features of the pillar structures, the droplets were more likely to stick to the sharp corners of the pillars due to increased Laplace pressure. These sharp features would have caused a stronger 'sticking' behavior compared to the smoother curves of the domes which would have lowered the energy barrier of the droplets to roll-off.

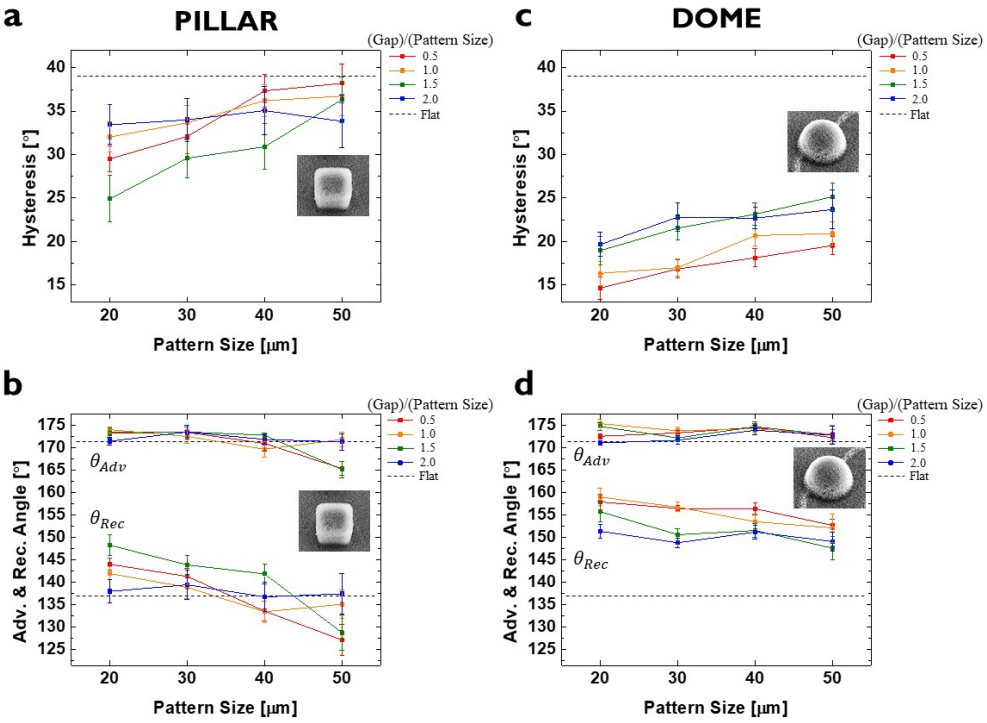

Figure 33: Dynamic contact angle measurements of various pattern sizes and spacings, and comparison between micropillars and microdomes. (a) Plot of contact angle hysteresis versus the micropillar pattern size (i.e. square width of the top surface). (b) Plot of advancing and receding contact angles against the micropillar pattern size. (c) Plot of contact angle hysteresis versus the microdome pattern size (i.e. circular diameter of the bottom surface). (d) Plot of advancing and receding contact angles against the microdome pattern diameter. All the dynamic measurements were done by the tilting plane method. For all plots, the error bars represent ± one standard error of the mean, and the sample size is five separate droplet shedding events per specimen.

The values for the experimentally determined average advancing angle, average receding angle, and average contact angle hysteresis for each sample are listed in Table 15 for the microdome samples and Table 16 for the micropillar samples.

For the dome samples:

Table 15: Average advancing angles, average receding angles, and hysteresis values for the Dome samples.

Sample #	Average Advancing	Average Receding	Hysteresis
1	172.3023333	155.26	17.04233333
2	174.4613333	154.732	19.72933333
3	176.3706667	159.818	16.55266667
4	173.749	160.7816667	12.96733333
5	177.192	152.1373333	25.05466667

6	174.158	148.9116667	25.24633333
7	175.679	164.2473333	11.43166667
8	176.6696667	149.8503333	26.81933333
9	176.0436667	166.3663333	9.677333333
10	174.3073333	167.2706667	7.036666667
11	177.364	169.9556667	7.408333333
12	174.181	164.3333333	9.847666667
13	172.704	165.8516667	6.852333333
14	173.3956667	158.9283333	14.46733333
15	176.1006667	163.2816667	12.819
16	177.2186667	156.842	20.37666667
Flat	174.1636667	135.059	39.10466667

For the pillar samples:

Table 16: Average advancing angles, average receding angles, and hysteresis values for the Pillar samples.

Sample #	Average Advancing	Average Receding	Hysteresis
1	175.125	154.4403333	20.68466667
2	174.6276667	152.4693333	22.15833333
3	169.052	142.726	26.326
4	163.9253333	129.1893333	34.736
5	176.0596667	152.8273333	23.23233333
6	172.404	140.93	31.474
7	169.2273333	140.4113333	28.816
8	170.9633333	148.434	22.52933333
9	174.9476667	144.687	30.26066667
10	173.3406667	136.5923333	36.74833333
11	173.4866667	154.971	18.51566667
12	158.3296667	132.6636667	25.666
13	172.4883333	152.2003333	20.288
14	173.2553333	143.992	29.26333333
15	171.262	151.4693333	19.79266667
16	166.9866667	150.4346667	16.552
Flat	174.1636667	135.059	39.10466667

3.8 Theoretical Hysteresis Model

A preliminary set of calculations for the receding contact angle of the droplet on a surface was performed using a capillary bridge model[77–79]. While contact angle hysteresis is a standard measurement for surface characterization, a definitive model for

predicting contact angle hysteresis on roughened hydrophobic surfaces has proved elusive. Existing attempts delve into energy minimization and balance looking at the Laplace pressure, hydrostatic pressure, movement of the triple phase contact line through molecular kinematic theory and capillary forces, surface tension, slip length and movement from surface friction, capillary bridging, and the Kelvin effect to name a few[80–83]. What is generally accepted is that the measured static contact angle of a surface falls between the advancing contact angle and receding contact angle. The advancing and receding contact angles are largely dependent on surface chemistry and topography. For instance, in the case of a roughened surface, the advancing and receding angles are affected by what is characterized as slip-stick behavior in which the droplet, as it is moving, will jump between the wetted surfaces of neighboring features to metastable energy states. Assuming that surface pores or gaps are too small for a perched droplet to overcome the capillary pressure and preferentially wet, the droplet will remain on the tips of the features and will skip over the gaps resulting in the slip-stick mechanism.

In the idealized case of the Cassie–Baxter model, the contact angle is determined by a free surface energy minimization at the three-phase contact line. The advancing angle corresponds to the maximum angle that the droplet can attain in its lower portion before it slides on a tilted surface or is the maximum angle a droplet achieves before changing to a different stable energy state if it is being inflated. It is largely dependent on surface topography and chemistry. For the dome and pillar structures developed in this project, a modified Cassie–Baxter formula was applied to predict the equilibrium contact angle for free surface energy minimization. However, there was a multiplicative factor offset between the predicted values and the measured values, with the measured values being lower. Instead, the modified Cassie–Baxter formula used previously is able to closely predict the actual advancing angles, especially for the dome structures, which can be explained by the equilibrium point of the contact line on a curved surface being similar to an advancing mode as opposed to a varying equilibrium state on a sharp-cornered surface with discontinuities in curvature.

However, the receding angle, which corresponds to the upper part of the droplet before rolling occurs on a tilted surface or the dewetting of the surface, depends strongly on the movement of the three-phase contact line over surface topography and is not necessarily equivalent to the motion of the advancing contact line. In a very preliminary calculation to determine receding angle, the tops of the features can be treated as solid surfaces that form individual, axisymmetric capillary bridges with the receding droplet in the case of the inflation/deflation hysteresis method. As the liquid volume is reduced through the syringe, a capillary bridge with a corresponding neck radius forms a concave droplet shape with the surface due to the inherent hydrophobicity (based on the superhydrophobic surfaces described in this thesis) and resulting negative capillary force. It is important to note that the initial assumptions are not taking into account evaporative effects, liquid viscosity, Wenzel or partial pinning modes, or thermodynamic effects. Gravity also has a relatively negligible effect due to a Bond number value of Bo = .77292 for a 7.5 μL volume droplet. The Bond number, which is a dimensionless constant relating

gravitational forces and surface tension forces, indicates a dominance in surface tension forces for values significantly less than 1. The interfacial tension from the solid surface and the surface tension from the liquid surface create a force balance at which the capillary bridge will rupture at a critical neck radius[84]. Based on early work by Kralchevsky and Nagayama, a force balance and shape approximation were determined for a capillary bridge between a solid planar surface and liquid planar surface[55,85–87]. In the case of the pillars, if each pillar is treated as the base for a bridge, then the radius corresponding to the meniscus at the contact line can be assumed to be half of the pillar length.

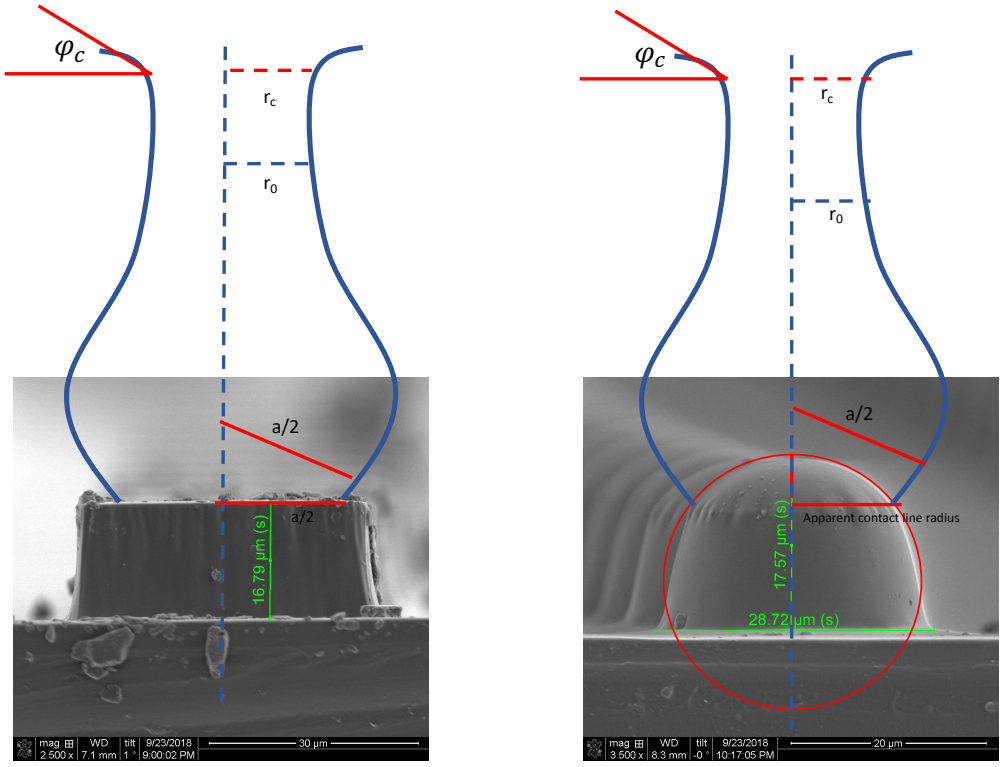

Figure 34: Capillary bridge formed on a hydrophobic pillar surface and hydrophobic dome surface at the moment before rupture when the capillary force is zero.

In the case of the dome structures, one could consider using the arc length of the cap as the contact area or the apparent contact area which would correspond to the radius value of the base of the cap that was calculated for the equilibrium contact angle point on the side of the dome. This refers to the point on the curved part of the dome structure that would experience the same contact angle based on free surface energy minimization as the general surface static contact angle. As mentioned earlier, this approximate point would be on a region of the dome in between points that would correspond to the advancing and receding angles separately. The varying cap radii length values for each of the dome features are:

Radius of feature (μm)	10	15	20	25
Apparent wetted contact radius (μm)	6.862302483	10.52186178	15.69715142	18.93553223

Beginning with a capillary force balance, the surface attraction of the droplet to the substrate is attractive, leading to a negative capillary force. In addition, with the hydrophobic substrate and subsequent meniscus angle, the curvature shape of the capillary bridge can be approximated using an unduloid model. The capillary force can be written as a sum of the force contributions from surface tension of the liquid and the meniscus capillary pressure:

$$F_c = F^{(\sigma)} + F^{(P)} \quad (20)$$

$$F_c = -\pi(2r_c\sigma\sin(\varphi_c) - r_c^2 P_c) \quad (21)$$

$$P_c = P_1 - P_2 \quad (22)$$

where P_c is the capillary pressure corresponding to the internal and external pressures of P_1 and P_2, r_c is the radius of the contact line at the particle surface, r_0 is the radius of the neck, and φ_c is the meniscus slope at the contact line and is equivalent to $180 - \cos(\theta)$ where θ is the contact angle at the meniscus. All variables are defined in Figure 34.

In looking at the point of rupture of the capillary bridge, the capillary force goes to zero

$$0 = F_c = -\pi(2r_0\sigma\sin(\varphi_c) - r_0^2 P_c) \quad (23)$$

$$2\sigma\sin(\varphi_c) = r_0 P_c \quad (24)$$

$$\varphi_c = sin^{-1}(\tfrac{r_0 P_c}{2\sigma}) \quad (25)$$

and the shape of the bridge approaches the shape of a cylinder. This leads to the approximation that the radius of the contact line can be approximated as the radius of the neck, which has a maximum value of the radius length or half the length of the pillar feature dimension. In this regard, $r_c \sim r_0$ and $0 < r_0 < \frac{a}{2}$. As also detailed by Kralchevsky and Nagayama, the capillary pressure can be nondimensionalized as

$$p = \tfrac{P_c r_0}{2\sigma} \quad (26)$$

For the case of an unduloid, p results in stable approximations of capillary bridge dimensions for $0 < p < \frac{1}{2}$. For the case of a cylindrical neck, $p = \frac{1}{2}$. This value was utilized for the simplified expression based on the assumption that at the point of rupture when the capillary force is zero, the neck geometry can be approximated as a cylinder[85,88].

$$\varphi_c(r_0) = sin^{-1}\left(\frac{r_0 P_c}{2\sigma}\right) = sin^{-1}(\frac{a}{4r_0}) \quad (27)$$

In order to calculate the receding contact angle, the meniscus slope angle can be used.

$$\theta_r(r_0) = 180 - \varphi_c(r_0) \quad (28)$$

Where the neck radius, r_0, is varied between 0 and $\frac{a}{2}$ given the previously stated assumption that the neck radius would not exceed the contact line radius. In graphing the receding contact angle with respect to changing neck radius, a percentage of the contact line radius, $\frac{a}{2}$, was used to account for a contact line radius being less than the actual feature length radius due to nanofeature roughness and some receding behavior along the wetted surface as droplet volume is decreased. This need became apparent due to the contact line radius giving predicted results that had a maximum of $150°$, which is lower than the measured values in some cases. In subsequent steps to build this model, an energy balance model would need to be utilized to determine the accurate contact line radius experienced by the droplet. However, in a preliminary analysis, it can be observed in Figure 35 and Figure 36 that for fractional amounts of the contact line radius, the predicted receding angles fall into the range of the measured receding angles[89].

For the dome structures:

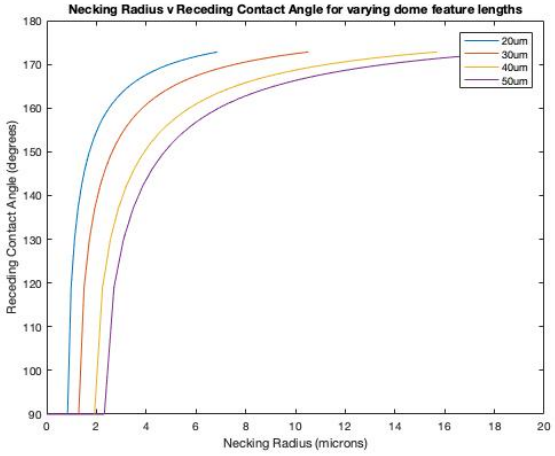

50% of cap radius value)

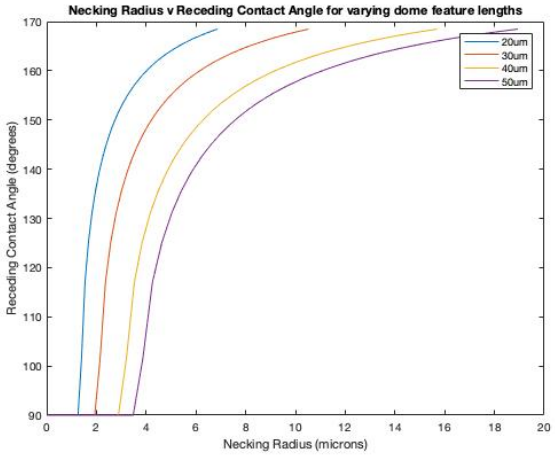

80% of cap radius value)

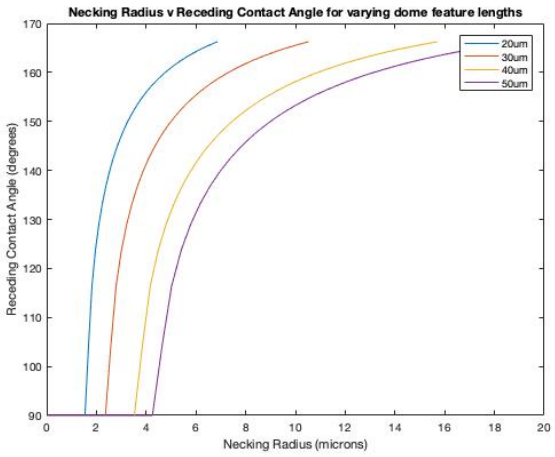

95% of cap radius value)

Figure 35: Receding contact angle for the dome structures as a function of the neck radius from a capillary force balance between the surface and droplet with the contact line or cap radius value varied as 50% of the original value, 85% of the original value, and 90% of the original value.

For the pillar structures:

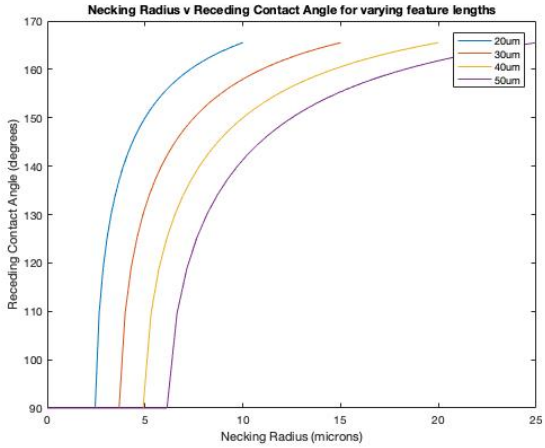

50% of cap radius value)

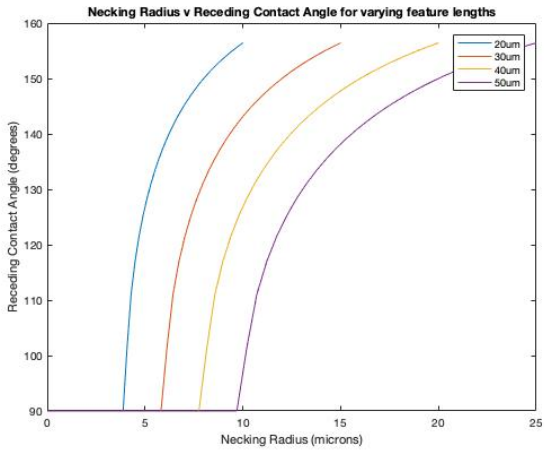

80% of cap radius value)

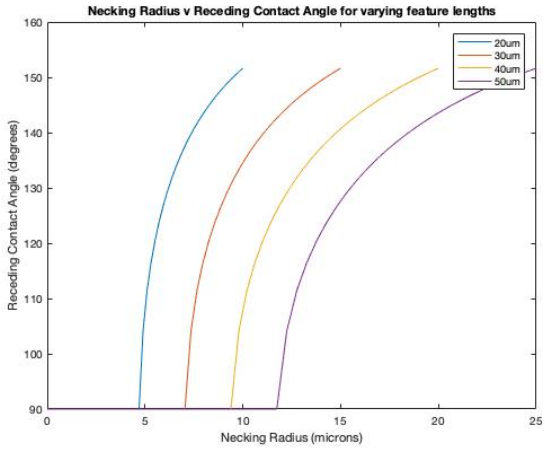

95% of cap radius value)

Figure 36: Receding contact angle for the pillar structures as a function of the neck radius from a capillary force balance between the surface and droplet with the contact line or cap radius value varied as 50% of the original value, 85% of the original value, and 90% of the original value.

Interestingly, hydrophobic and hydrophilic interactions between a liquid and solid surface can be treated with similar geometric and energy balance analyses by initially assuming a capillary bridge shape, which could be based on a spheroid, catenoid, cylinder, unduloid, or nodoid. An unduloid was assumed for hydrophobic capillary bridge formation in the case of the silanized dome and pillar surfaces and a cylinder approximation was selected for the point of rupture allowing for selection of a nondimensionalized, stable capillary pressure value.

It is important to note that in order to provide a proper energy balance with the interfacial tension of the substrate, the capillary bridge, and the surface tension of the liquid, viscous effects, evaporative effects, and contact line dynamics would need to be taken into account. In other words, the pattern density, which would reduce the surface tension experienced by a single feature for a higher density of features, is not taken into account. In addition, the contact line radius is treated as being equal to half of the pillar length or half of the dome cap diameter. As droplet volume is decreased, this contact line would also begin to decrease until a rupture event occurred. A contact line dynamic formulation would be required to solve for the actual contact line radius for a more refined solution. Also, this solution analysis is based on the receding contact angle pertaining to the microfeatures. Due to the presence of nanofeatures that introduce additional surface roughness as well as a wetted area fraction, the contact line assumption would further need to be reduced if the wetted percentage of the region was to be taken into account.

3.9 Conclusion

This study provided a description of the fabrication and characterization of biomimetic microdome and micropillar hierarchical surfaces. By comparing the dome geometry to standard pillar configurations, it was demonstrated that microdomes with ZnO nanostructures had superior droplet shedding capability when compared to micropillar structures. The dome features, in every gap to pattern size and pattern size case had higher observed and predicted contact angle values and lower hysteresis values when compared with the pillar structures as well as the flat, nanostructured case. Theoretical models for static contact angle prediction and advancing and receding contact angle prediction were also evaluated based on the measured experimental values.

4 Chapter: Condensation test bed design

4.1 Wind Tunnel Test Bed

In order to evaluate the dome and pillar structures for air conditioning applications, a test bed design was required to simulate condensation on HVAC materials in tropical conditions. A closed-loop wind tunnel design was chosen to allow for recirculating hot and humid air for stable conditions during testing.

4.2 Introduction

Wind tunnels are experimental tools typically used to study airflow characteristics around a stationary object. Originally utilized to examine aerodynamic forces around early aircraft concepts, wind tunnels have since developed in both purpose and design, varying test section size, flow velocity, open or closed circuit setup and uses for modeling aircraft, automobiles, wind flow past building configurations, and improving CFD models, to name a few[90]. Wind tunnel design depends primarily on the intent and final purpose of the test section with respect to air flow, air speed, and size conditions. Once a design is finalized and built, aerodynamic parameters are tested and recorded to validate the original desired test conditions.

The purpose of the following wind tunnel design is to simulate the environmental conditions which HVAC components may be exposed to in tropical environments through a low cost, easily fabricated, lab-scale test bed. Size constraints were determined based on a scaled down, interchangeable evaporator coil model that would allow for a variety of coated materials to be fabricated and analyzed. Utilization of 3D printing allowed for rapid manufacturing of contraction and diffuser design components to enable various test section dimensions. The key parameters for the selected design included: temperature, relative humidity, and air velocity. Because the testing apparatus was designed to replicate the inside of a HVAC system, some turbulence in flow conditions was advantageous, as most HVAC systems do not include turbulence minimization devices. Selection of temperature and humidity ranges was motivated by the tropical environment of Singapore where the mean monthly temperature ranges from 26–27.5 °C[91], and the monthly relative humidity (RH) is over 80%[92]. In the United States, HVAC accounts for over 50% of a non-residential building energy usage[93], and in tropical nations, such as Singapore, the percentage is 60%, with the added statistic of 98.8% of residential apartments owning air conditioning systems[94]. It was desired to have a testing apparatus to study the condensation formation and shedding on a cooling coil, as well as the behavior of the water droplets after they leave the cooling coil. The test bed design, materials used, manufacturing process, and validation of the testing apparatus are detailed below.

4.3 Design and Construction

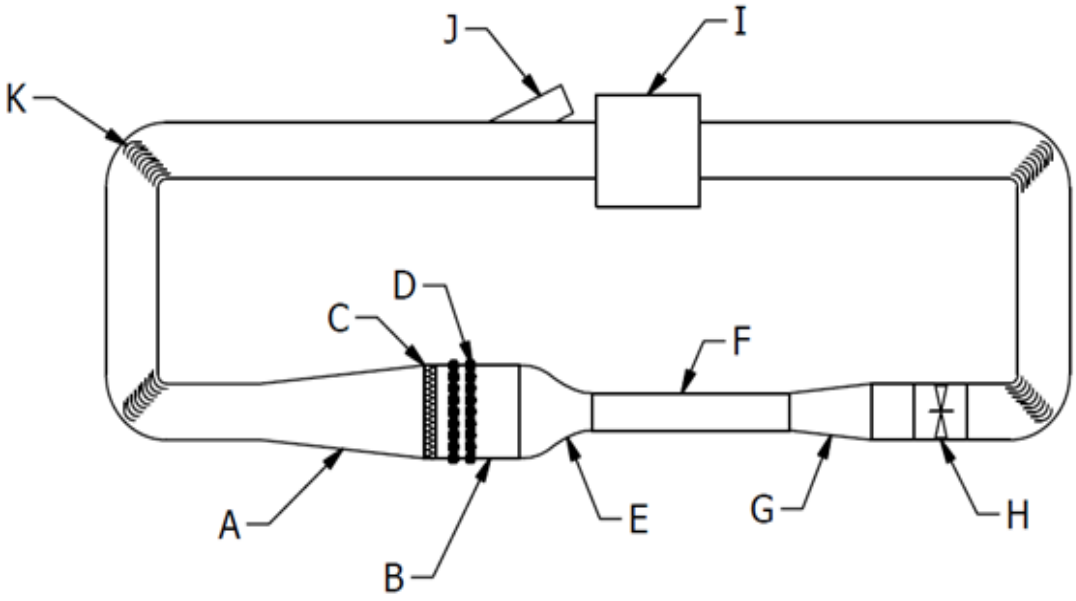

Figure 37: Schematic of closed-loop wind tunnel. (A) Diffuser number 1. (B) Settling chamber. (C) Honeycomb. (D) Screens. (E) Contraction. (F) Test Section (4" × 4" cross section). (G) Diffuser number 2. (H) Axial fan. (I) Resistance heater. (J) Input for water vapor stream. (K) Turning Vanes.

The key design, performance, and setup parameters under dynamic wetting conditions include the following:

- Condensation testing in the wind tunnel setup at supersaturation (SS) values
  - Low SS: 1.1–1.25
  - High SS: >1.25

- Heater, nebulizer, chiller, and fan to simulate AC condensing environment
  - 100 mm^2 test section

- Samples mounted to peg with stereomicroscope to video
  - Video recordings for samples 20–30 min duration
  - Sample thickness 1 mm

- Condensation and shedding will give different characterization of patterns

- Air conditions
  - Temperature range 36–38°C
  - RH values 40–50 %
  - Air Velocity ~ 3 m/s

4.4 Wind tunnel airflow components:

Figure 37 shows a schematic of the condensation research wind tunnel. This is a closed-loop wind tunnel with a test section that can be easily changed to accommodate different experiments. The wind tunnel can be used to conduct flow and condensation experiments on sections of cooling coils, as well as on chilled material samples.

A closed-circuit wind tunnel design was selected for the condensation simulation. The two primary types of wind tunnels include an open-circuit design, in which airflow follows a path through a contraction, test section and diffuser before being released to the atmosphere, and a closed-circuit design that maintains airflow in a loop. The closed-loop design is advantageous in the case of a humid-flow environment because it reduces the heat and vapor input for the airflow. The airflow is in a counterclockwise direction based on the above figure and originates from the axial fan. The primary concerns driving the aerodynamics of the wind tunnel design were minimizing pressure losses throughout the tunnel setup and maintaining specific air speed and flow conditions in the test section. The following discussion delves into greater detail about parameter selection for the various aerodynamic components in the setup.

The working section of the wind tunnel consists of a first diffuser, a settling chamber with honeycomb and two screens, a contraction, the test chamber, a second diffuser, and a fan.

4.5 Diffusers

Two diffusers were utilized in this wind tunnel design. The first diffuser was composed of two items, an adapter to change the shape from round to square shown in Figure 38, and a diffuser to expand the cross-sectional dimensions from 6-inch square, to 10-inch square placed in front of the flow straightening section shown in Figure 39. The adapter was created in a fused deposition modeling (FDM) 3-D printer (Ultimaker) and is designed to slip over the 6-inch round duct at one end, and screw into the other mating square diffuser. To change the cross-sectional dimensions, a diffuser was built with inlet dimensions of 6×6 inches, and outlet dimensions of 10×10 inches with an expansion angle of 6°. This diffuser section was built of 0.125-inch-thick plywood and coated with clear polyurethane. Flat areas were insulated with 0.5-inch-thick polyisocyanurate foam board insulation.

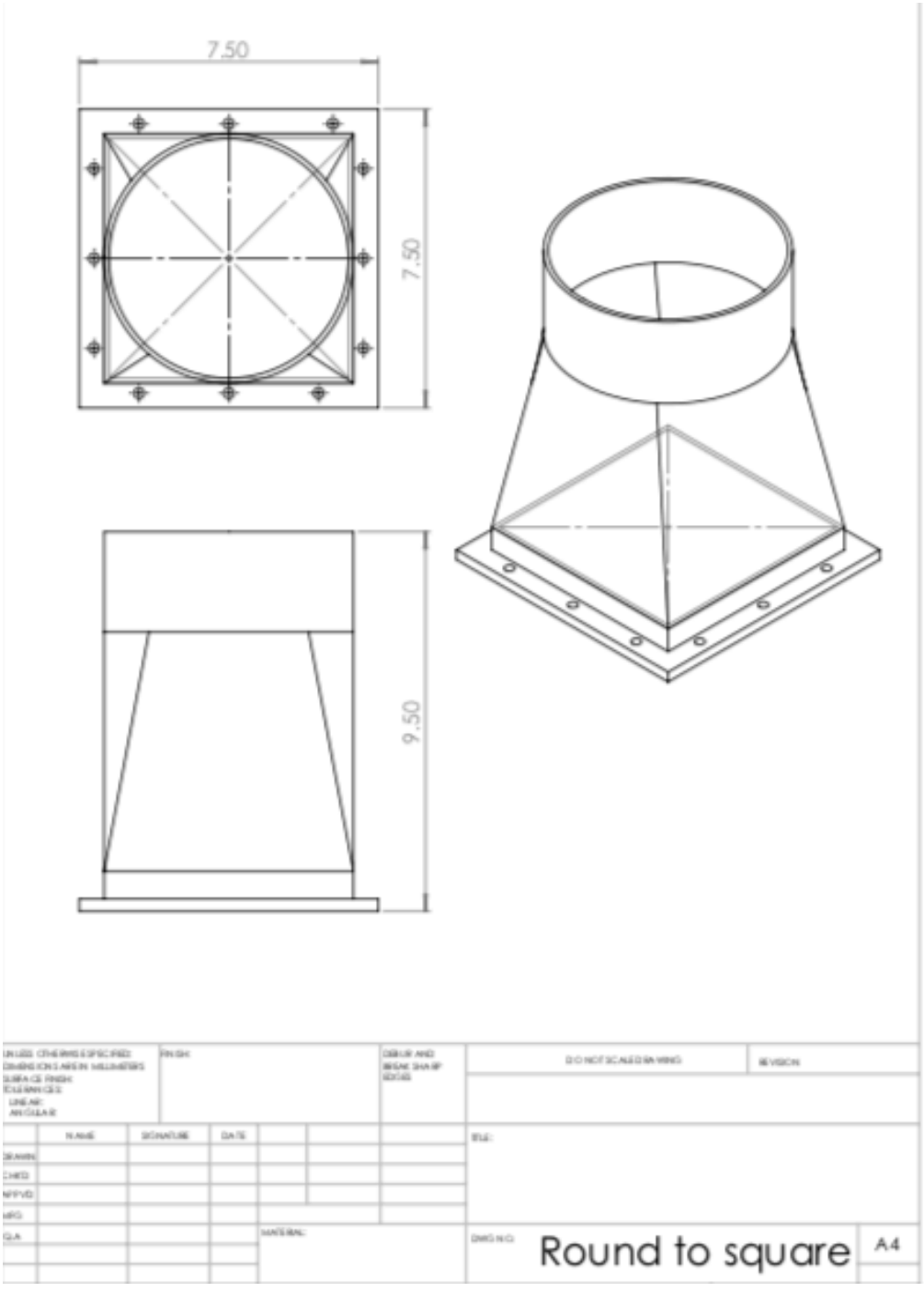

Figure 38: Partial engineering drawing and isometric view of the wind tunnel round to square adapter from the ducting to the diffuser and test section.

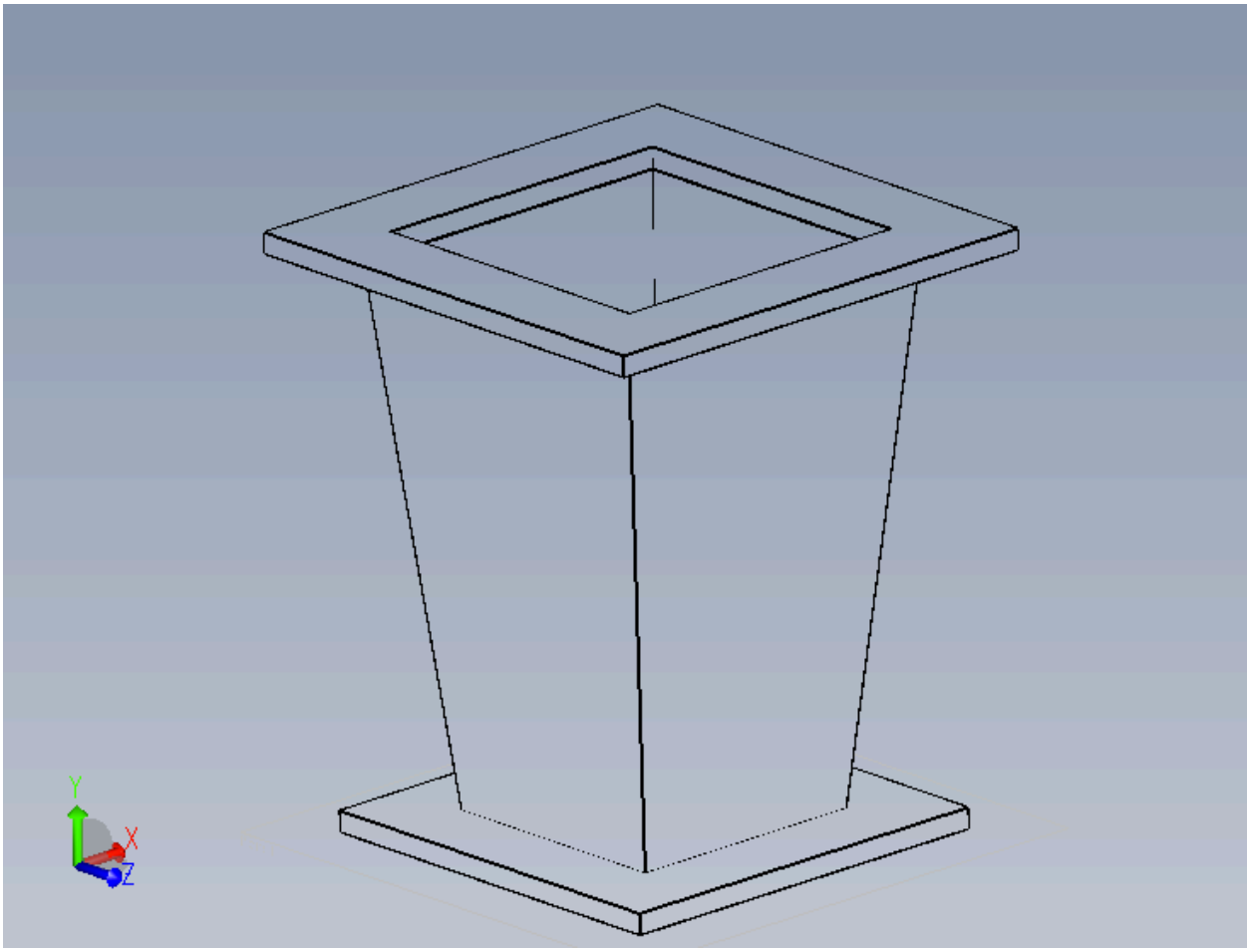

Figure 39: SolidWorks rendering view of the wind tunnel diffuser.

The second diffuser had inlet dimensions of 4 × 4 inches, and outlet dimensions of 6 × 6 inches with an expansion angle of 6° total and was designed to recover some of the pressure losses experienced in the test section. As a general rule, the diffuser should be as long as possible to maximize pressure recovery and the angle of the diffuser should be no greater than 3.5° per side in order to avoid flow separation from the diffuser walls. This diffuser section was built of 0.125-inch thick plywood and coated with clear polyurethane. Flanges were built at the ends of the diffuser so that it could be attached to the mating pieces of the wind tunnel.

4.6 Contraction

The contraction placement and design serve to increase the airflow velocity by reducing the cross-sectional area of the tunnel from the duct size to the test section size. The most critical considerations in contraction design include the contraction ratio (size of the inlet relative to the size of the contraction outlet), shape, and radius of curvature. Contraction ratios ideally should be between 7–10 in order to reduce adverse flow and turbulence that would be generated if the curvature of the contraction varied too

quickly[95]. Conical contractions are preferred because larger pressure losses are experienced from any square or cornered design. However, adverse effects from square cross sections can be mitigated if a sufficient amount of straight ducting follows the contraction section in order to reestablish laminar flow conditions. Radius of curvature is determined roughly via cubic spline in order to minimize boundary layer growth. The contraction used was designed to have a 6.25:1 ratio with inlet dimensions of 10-inch square, and outlet dimensions of 4-inch square. It was created by forming 0.0092-inch aluminum around a wooden form. The inside was coated in fiberglass reinforced polyester body filler (Bondo) for strength and was sanded smooth. Flanges were built into either end of the contraction to facilitate mating to adjacent wind tunnel pieces.

4.7 Turning Vanes

Around 50% of pressure losses in closed-circuit wind tunnels are experienced at the tunnel corners; and turning vanes or turning vane cascades, pictured in Figure 40, are typically used to reduce the pressure losses across corners. The dimensions for the turning vanes were chosen for an ideal gap/chord ratio of .25, based on standard, empirical wind tunnel design data[96,97]. Based on the flow direction, there should be a 4° angle of incidence at the beginning of the vane cascade with the trailing edge positioned parallel to the downstream flow. Due to the thickness of sheet metal, which was chosen as vane material, 9–10 vanes were used per cascade per corner. Dimensions included: total length of vane: 2.5”, curved part 1.8” with a radius of curvature of 1.2” and a straight extension of .7”. The gap between vanes was .545”.

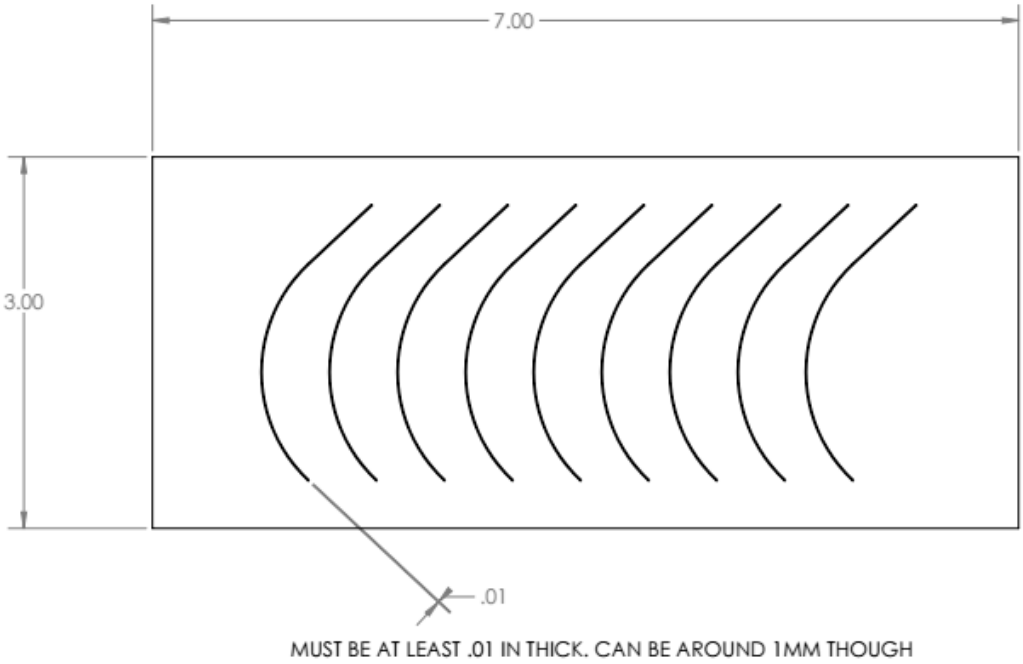

Figure 40: Engineering drawing side view of wind tunnel vane layout.

4.8 Settling Chamber

Based on the size of the settling chamber, 1 honeycomb piece and 2 screens were utilized with 2" spacing between each component in order to straighten the flow and reduce lateral turbulence (although axial turbulence is introduced, it is possible to reduce it by having a long, straight section of 10–15 times the duct width, which was unrealistic for the lab space available). The ratio of screen:apertures needed to be approximately .57[90] so that pressure loss across screens wasn't too high. Placement of screens was used to straighten flow before the test section to help achieve the desired test section airflow velocity as well as laminar, developed flow characteristics. The settling chamber was constructed out of 0.125-inch-thick plywood and coated with clear polyurethane. It measured 10-inch square in cross section and was 12 inches long. The flow straightener was a sheet of aluminum honeycomb spanning the entire cross section. After the honeycomb, 2 screens were placed 2 inches apart, the first one 2 inches from the flow straightener. The screens were of 16 mesh aluminum and spanned the entire cross section.

4.9 Test Section

The key parameters for a test section design selection include desired test section air speed and cross section shape in order to maintain laminar flow and minimize drag. For the HVAC simulation application, the cross section was dictated by the evaporator coil sample size. Other key parameters for the selected design included: test section velocity, required fan and heater power, energy input necessary for test section relative humidity (RH) of up to 90%, overall size, and ease of construction. Due to the importance of flow visualization through the test section, it was also desired that the test section be modular and easy to instrument. Additionally, sections of cooling coil could be installed directly into the wind tunnel to test behavior of cooling coil materials and design. In this case, the cooling coil spanned the entire cross section, and had viewing windows to observe condensation on the cooling surfaces. Secondary contractions and diffusers could be installed at either end of the cooling coil should the cross-sectional area need to be changed.

Dimensions were chosen to achieve the above parameters as well as to reduce the pressure losses through the tunnel as much as possible. Two test section purposes were selected. The first was a complete, scaled-down cooling coil. The second was a standard material testing section created for testing of material samples mounted to a cold plate shown in Figure 41. The cold plate was designed to have coolant running through the backside for active chilling during experiments. The test section itself was 21 inches long with a 4-inch square cross section. A 4-inch-long viewing window was placed in the center of the top and front sides and was made of 0.125-inch-thick acrylic. The inside of the test section was painted black for contrast and was coated in clear polyurethane.

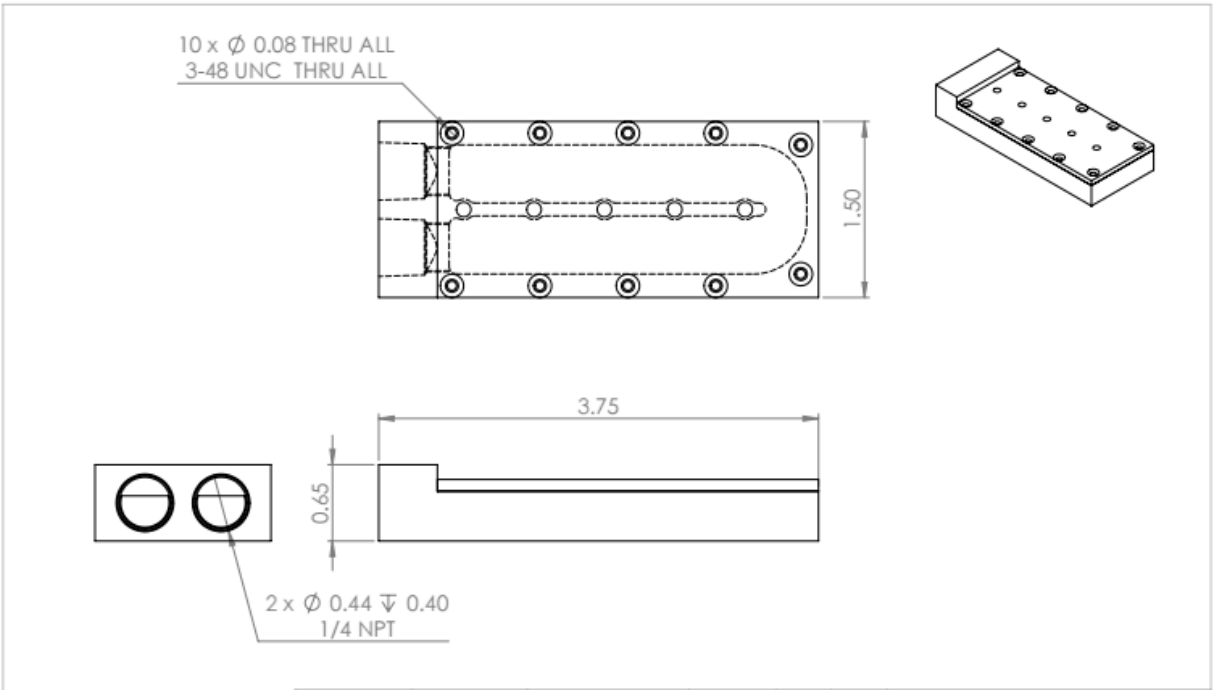

Figure 41: Engineering drawing of aluminum SEM peg mount for wind tunnel test section.

4.10 Test Section Calibration

4.10.1 Air Flow Results

Air flow velocity in the test section was measured at varying fan powers as a percentage of maximum power using a differential pressure anemometer (Fluke). Air velocity measurements were taken from an array of points in the cross section. The pattern of measurement points was 5 across and 5 high, at values of 0.296, 1.152, 2.000, 2.848, and 3.704 inches determined by the Log-Tchebycheff rule for rectangular ducts that takes the duct size into account and averages all velocity readings for a given cross section[98]. Holes were cut into the top of the test section for insertion of the anemometer pitot tube so that it would directly be facing the oncoming flow. Average velocities versus fan power are shown in Table 17. The fan used to move the air in the wind tunnel was an axial style fan (delta model number THB1548AG) running on 48 V DC.

Table 17: Percent Fan Power vs. Average Flow Speed (m/s)

% Fan Power	Avg. Flow Speed (m/s)
100	17.205
90	16.578
80	15.621
70	14.685
60	12.088
50	10.046
40	8.247
30	6.756
20	5.507

The maximum theoretical air speed given the dimensions of the wind tunnel cross section, and assuming zero static pressure was 24 m/s and was calculated from Velocity = (Volumetric Flow Rate) / (Cross sectional Area).

In order to determine if the flow was laminar or turbulent, the Reynold's number, a dimensionless coefficient relating inertial and viscous forces, was calculated for the test section geometry[99]. The Reynold's number for pipe flow is,

$$Re = \frac{u d_h}{v} \qquad (29)$$

where u is the velocity in m/s, $d_h = \frac{2ab}{(a+b)}$, is the hydraulic diameter for a rectangular duct with sides of a and b, and v is the kinematic viscosity in $\frac{m^2}{s}$ at given temperature and pressure conditions. To gauge a range of Reynold's numbers, values of 1 m/s to 20 m/s were input for incoming airflow velocity. Realistic values would be between 1.5 and 2 m/s for the experiments in this tunnel. This yielded Reynold's numbers from approximately 6100 to 120000, which is significant because numbers greater than 4000 for pipe flow are considered turbulent.

It is also worth noting that based on test section cross-section and length, the airflow is not fully developed. However, because a settling chamber and honeycomb flow straighteners were upstream of the test section, flow conditions could be improved before reaching the test section and subject. In addition, the Reynold's number calculations pertained to airspeed seen specifically in the center of the test section where the sample was placed. Thus, the sample would see some turbulent flow. Flow near the walls is laminar due to skin friction on the boundaries that reduces air velocity to zero.

For the ducting sections and to minimize overall construction cost, standard 6-inch diameter galvanized steel-round HVAC ducting was used as the airflow channel. This ducting is typical of both commercial and residential HVAC installations. The turning vane

cascade was fabricated and installed into the 6-inch diameter HVAC elbows that were used for the four corners.

4.11 Environmental Generation

It is desired to replicate the environment that HVAC components would be exposed to in tropical, urban, regions, specifically Singapore. As mentioned previously, in these climates, the temperature remains fairly constant at around $27°C$[91], and relative humidity is usually above 85%[92]. The surrounding conditions of the testing apparatus are roughly $21\ ℃$ and 30–40% RH. Using the nebulizer and heater within the closed loop, a variety of supersaturation conditions was easily achieved. Temperatures, for safety, could be brought up to $40\ ℃$ although simulated conditions were better achieved ranging from $32\ ℃ – 34\ ℃$, and relative humidity values could be achieved reliably up to 90% based on the purchased sensors.

4.11.1 Latent Heat

With such high RH values seen in areas such as Singapore, humidity plays a key role in the power consumption of an air conditioner. Dry air at 1 atm and $30\ ℃$ conditions has a specific heat of 1.005 kJ/kg*K. Water has a specific heat of 4.187 kJ/kg*K, meaning that to raise the temperature of a unit of water 1 degree would take four times as much energy as to raise that same unit of air by one degree[100]. Water also has a high latent heat of vaporization of 2270 kJ/kg, which is the amount of energy required to evaporate liquid water at its saturation point[101].

The moisture in the air is often expressed as relative humidity (RH), where

*RH= 100% ** (*Actual Vapor Density*) */* (*Saturation Vapor Density*).

A RH of 100% would indicate that the air is holding the maximum amount of water vapor it can at that temperature and pressure, and the addition of any more water vapor would force some water vapor to condense.

In order to generate humidity conditions representative of the tropics, with RH values approaching 85%, water vapor and heat must be supplied to the air. To provide the additional moisture, a purchased nebulizer was installed. The nebulizer used a stream of air to atomize water into droplets of varying sizes and inject them directly into the oncoming airflow after the air left the heater and before it reached the turning vanes and settling chamber. The heater, a resistance heater specifically designed to be installed into ducting, heated the dry air, helping to evaporate many of the water droplets. The nebulizer and heater combined raise the relative humidity of the air while simultaneously slightly lowering the temperature due to the latent heat of vaporization as water droplets evaporated. The air needed to be overheated to account for this cooling action.

4.11.2 Cooling

A DuraChill air- and water-cooled 1.5 HP chiller was purchased with cooling capacity down to $-5\ ^{\circ}\mathrm{C}$. A mixture of 38% ethylene glycol to deionized water was used as a coolant. Tubing was connected from the chiller output into the back of the aluminum peg mount in the test section. The conduction from the coolant through the aluminum block allowed the block to achieve a temperature close to the desired set point of the chiller — in the case of the experiments detailed later, around $4\ ^{\circ}\mathrm{C}$.

4.12 Control System

Due to the unique application of this testbed as a means for observing droplet condensation on various materials in a controlled, HVAC-simulated environment, the telemetry setup focused on airflow, temperature and relative humidity data. However, based on the interchangeable geometry of the test section, different sensors could be placed upstream and downstream of the test samples based on desired information.

For the later purposes of condensation testing, two Dwyer duct-mount 2% RH/temperature transmitters using 4–20 mA for RH output and 4–20 mA for temperature output, with an LCD screen were purchased. One was placed upstream and the other downstream to determine real-time readings of RH and temperature within the testbed. A simple potentiometer circuit using an Arduino microcontroller was designed to operate the axial fan and adjust air speed based on pulse width modulation (PWM). A similar circuit was also implemented for the heater. In order to adjust the humidity, manual input was used for the nebulizer.

In order to monitor and power the fan, heater, and nebulizer, the electrical arrangement consisted of:

1. Fan
    - 48 V power directly from AC to DC converter
    - PWM Control (Arduino)

2. Heater

    - V amplified to 10 V using an op amp.
    - Power comes from Arduino
    - PWM control (Arduino) or manual control

3. Nebulizer
    - Adjustable, manual knob
    - 120 V AC power

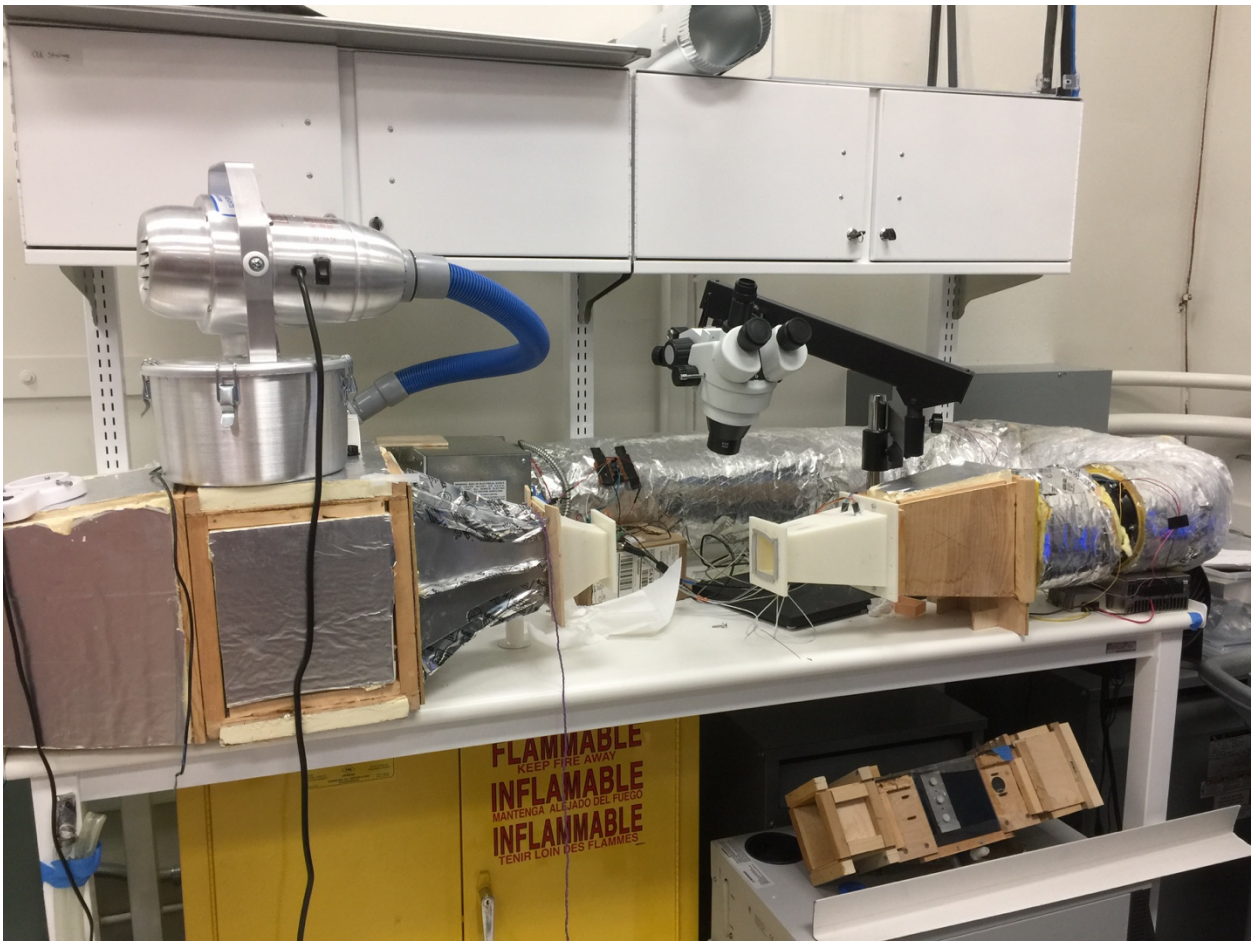

Figure 42: Picture of wind tunnel test setup with test section removed.

4.13 Conclusion

Parameters and design considerations for a low-cost, low-speed, lab-scale, and humid air conditioned wind tunnel test setup have been presented with the final result pictured in Figure 42. Readers wishing to replicate this arrangement will have a baseline of values for a small scale, subsonic design with validated air speed and flow parameters. The modularity of the design both in terms of the test section construction and the available sensor system allow for a broad range of applications.

5 Chapter: Condensation Theory

5.1 Heat Transfer Background

Heat transfer experiments are outside the current scope of this work. However, basic heat transfer theory can be applied as a preliminary means to better understand and explain experimental observations and results. In order to take a deeper look at the heat transfer component, both conductive and convective modes need to be considered depending on whether the surface is experiencing dropwise or filmwise condensation. For filmwise condensation, an important limiter of heat transfer is conduction through the liquid film on the surface of the aluminum substrate. A model treating each layer with its respective thermal resistance can be employed to calculate the conductive heat transfer from the boundary layer of the water film that comes into contact with the air flow, to the back-cooled plate of the testing apparatus. A convective heat transfer model can then be applied for the surface of the droplets or film with respect to the incoming airflow. In the case of dropwise condensation, the portion of the aluminum surface free of water also comes into contact with the incoming airflow — this can be treated as a location of convective heat transfer as well.

It is important to note some of the force interactions taking place with respect to the surface condensation in an evaporator coil. The incoming airflow provides a shear force parallel to the plate surfaces. Depending on the size of the droplets, droplet-surface interaction forces, and air speed, the shear force can assist with droplet shedding. Gravitational force also should be considered for droplet shedding. However, the size of a droplet required to reach a Bond number of 1 in which the gravitational force becomes the dominating force instead of capillary forces results in a critical capillary length droplet of 2.71 mm diameter or larger. Droplets of this magnitude are not ideal for heat transfer surfaces due to the size and the time needed for enough coalescence events to occur for that size to be achieved. The advantage of many manufactured superhydrophobic surfaces is that the droplet shedding size occurs for droplets of sizes several magnitudes smaller than the critical capillary length.

Water acts as a thermal barrier for heat transfer due to its low thermal conductivity compared to metal. Dropwise condensation is notably better at heat conduction than filmwise condensation due to increased coalescence and shedding events that create fresh, unwetted surface for further heat transfer to take place with the incoming air.

In the case of the condensation experiments, a 1-D steady state heat transfer analysis was performed to evaluate the thermal resistance experienced by the mounted sample[102]. The following layers, shown in Figure 43, were evaluated for thermal conductivity based on the sample fabrication. Using thermal tape, a sample of PDMS sputtered with a 5 nm layer of chrome, a 150 nm layer of aluminum, a 3 μm layer of zinc oxide nanowires grown on top of the aluminum, and a deposited monolayer of silane was

placed on an aluminum block with a chilled mixture of ethylene glycol and water running through it. These layers were treated as behaving according to a conductive heat transfer model while the aluminum block and regions of the sample not covered by condensation experienced convective heat transfer from the air stream. The droplets themselves also had a thermal resistance through the droplet, a resistance associated with the interfacial layer between the droplet and the air, and a resistance associated with the curvature of the droplet through the Kelvin effect in which the saturation vapor pressure is higher for a curved surface. However, the Kelvin effect is generally negligible for droplets larger than a fraction of micron. It was assumed based on the input conditions shown in Table 18 of the air and chiller that the layers of silane, ZnO, and tape were thin enough that their thermal resistance was deemed to be negligible relative to the thermal resistance of the PDMS layer.

Table 18: Input values for a standard condensation experimental setup.

$T_{wall} = Aluminum\ Wall\ Temp.$	3.5℃
$T_{air} = Hot\ Air\ Temp.$	37℃
$T_{PDMS\ Surface}$	16.5℃
$T_{coolant}$	~2℃
RH	~ 40-50%
Supersaturation (depending on experiment)	~ 1.2-1.4

The thermal analysis was treated such that the boundary conditions pertaining to the coolant block temperature and the air and vapor temperature were constant over time.

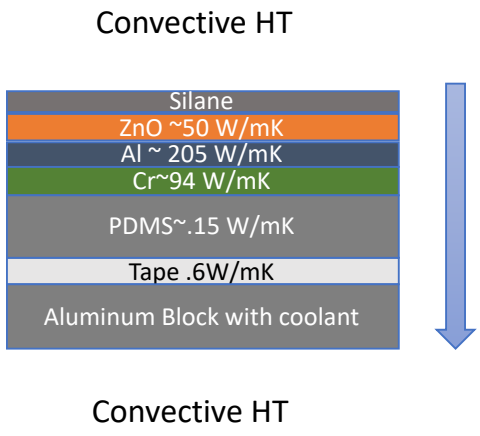

Figure 43: Thermal resistances for a sample mounted in the condensation test setup.

To determine a heat transfer coefficient for a surface, the thermal resistances were added together to reach a total equivalent resistance combining conductive and convective effects. In the case of the droplets, heat is transferred from the saturated vapor through the liquid–vapor interface, which has associated resistances for the curvature and interface itself. The remaining steps of heat transfer to the coolant block depend on

whether the droplet is wetting the pores of the surface or is suspended on top of the features. In the case of wetting, heat is conducted through the droplet to the substrate, including the microfeatures, and cooling block. However, for a suspended droplet, the heat transfer must also take into account the thermal resistance of air gaps between substrate features. The thermal resistance of air is much higher than that of water. Thus, heat transfer for a drop that partially wets the surface compared to a suspended drop is higher due to the improved conductivity of a layer of water. This is only the case for an individual droplet. For filmwise and dropwise condensation, convective heat transfer for a condensation-free surface is much more effective than conductive heat transfer through a layer of water. As a result, dropwise condensation has much better heat transfer than filmwise condensation.

To determine total heat flux, the heat transfer rate for a single droplet would need to be determined as a function of droplet size and boundary conditions, and the heat transfer contributions of all droplets on the surface — which in practice have a distribution of sizes — would need to be summed.

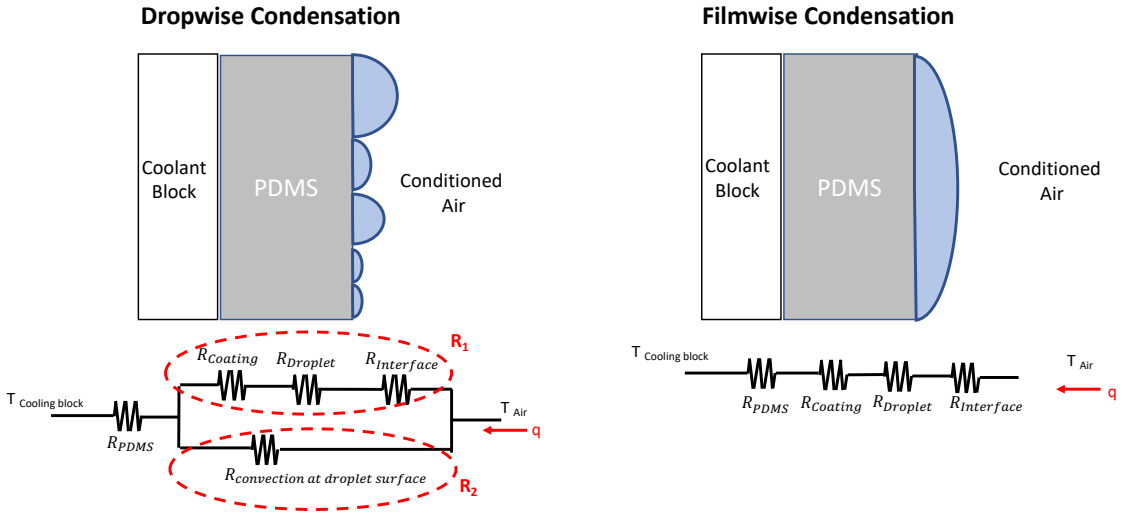

Figure 44: Thermal resistance diagrams for dropwise and filmwise condensation cases.

The equivalent circuit diagram, shown in Figure 44, is important when comparing the thermal resistance of dropwise vs filmwise condensation. By treating R_1 as the thermal resistance of the condensation and R_2 as the thermal resistance of the condensation-free surface, a total thermal resistance can be calculated for the dropwise case. For the filmwise case, it is assumed that the primary thermal resistance is the film of water with no exposed condensation-free surface.

$$\Delta T = q \cdot R_{th} \tag{30}$$

$$R_{Dropwise} = \left(\frac{1}{R_1} + \frac{1}{R_2}\right)^{-1} = \frac{R_1 R_2}{R_1 + R_2} = \frac{R_1}{1 + \frac{R_1}{R_2}} \tag{31}$$

$$R_{Filmwise} = R_1$$

Thus,

$$R_{Filmwise} > R_{Dropwise}$$

5.2 Nucleation Theory and Coalescence

In looking at nucleation, growth, and coalescence more closely, Tuteja et al. identified three general droplet growth morphologies for microstructured surfaces, pictured in Figure 45. Droplets can nucleate and grow on the tips of features barring interaction with other droplets or gravitational forces. Nucleation is also experienced on the sides of features and within the pores between features. The latter two will lead to a partially wetted mode or pinning. As nucleation occurs and droplets grow, the pores become filled once the droplet touches the feature base and continues to grow beyond the initial unit cell. In the case of nucleation on the side of the feature, the contact line may not reach the unit cell bottom in which case the droplet can continue growing above the surface without pinning[103,104].

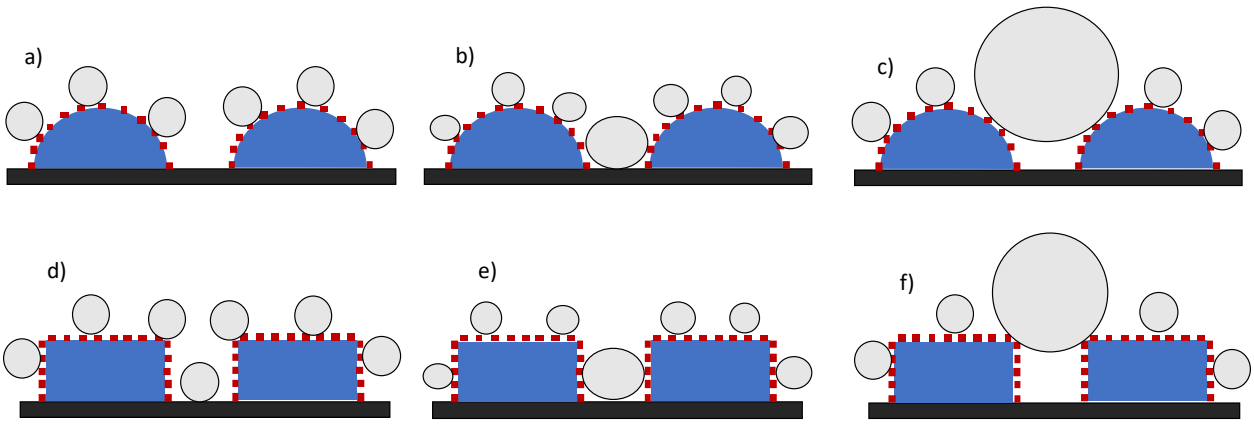

Figure 45: The dome structures in a-c experience different morphologies for growth. In a), droplets nucleate on the sides of the features. In b), a droplet nucleates in the gap region as well as the feature sides. In c), droplets merge into a suspended state as opposed to a wetted state. The pillar structures in d-f experience different morphologies for growth. In d), droplets nucleate on the sides of the features and in the gap. In e), a droplet coalesces in the gap region and nucleates on the feature sides. In f), droplets merge into a suspended state as opposed to a wetted state.

In general, nucleation depends on the surface roughness and surface energy. By classical nucleation theory and the principle of Gibbs free energy, the free energy barrier that must be overcome for heterogeneous nucleation is lower than that for homogeneous nucleation.

$$\Delta G_{max}^{het}(\theta_Y) = \Delta G_{max}^{hom} \frac{(2+cos\theta_Y)(1-cos\theta_Y)^2}{4} \quad (32)$$

$$\theta_Y = 0° \rightarrow G_{max}^{het}(\theta_Y) = 0$$
$$\theta_Y = 90° \rightarrow \Delta G_{max}^{het}(\theta_Y) = \frac{1}{2}\Delta G_{max}^{hom}$$
$$\theta_Y = 180° \rightarrow \Delta G_{max}^{het}(\theta_Y) = \Delta G_{max}^{hom}$$

Condensation will occur preferentially on a surface rather than on another existing droplet. However, in the case of a fully hydrophobic surface with contact angle of 180°, the free energy barrier for condensation is the same as that of homogeneous nucleation and there is no preferential nucleation site. When nucleation eventually does occur, the hydrophobicity leads to an increase in critical nucleation radius as well as a decrease in nucleation site density. As reference, classical nucleation theory for a heterogeneous surface gives a critical nucleation droplet radius of 7 nm, a droplet nucleation radius for inertial coalescence of 15 nm, and average nucleation site density $5 * 10^9$ sites/m^2[105].

In addition to surface energy, surface roughness plays a strong role in determining nucleation. For example, based on the Kelvin effect, water is less likely to condense on a highly curved surface at the nanometer length scale. The saturation vapor pressure is higher over a curved surface such that water vapor won't condense readily out of the air onto the surface[106].

a)

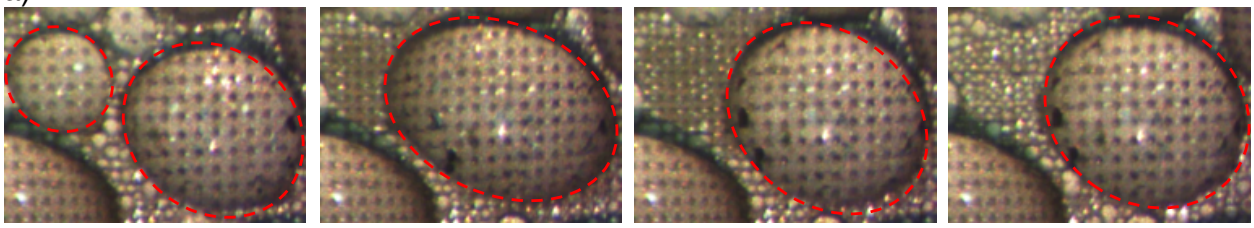

b)

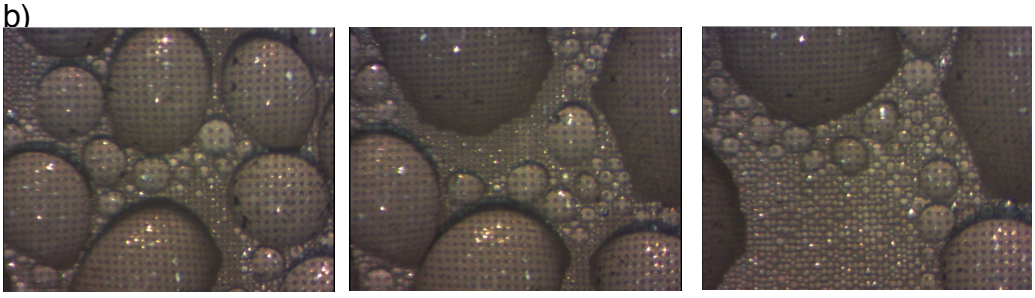

Figure 46: Two instances of droplet coalescence and shedding for long term video footage of condensation testing for the dome structures. In a), two droplets merge to form a droplet with larger volume. New area is freed for condensation and the combined droplet shrinks in surface footprint by reducing its surface area. In b), several droplets merge and shed outside the footage frame revealing condensation-free area for heat transfer to occur and more condensation to take place.

However, after initial nucleation and growth such that droplets are large enough to interact with adjacent droplets, coalescence can occur either through viscous or inertial forces. During coalescence events on hydrophobic surfaces, several researchers have observed a droplet jumping phenomenon due to the release of excess surface energy as the enlarged droplet minimizes its surface area[45,107–110]. This may or may not allow the droplet to overcome pinning forces. In the absence of droplet jumping or external shear forces, a droplet relies on gravity for removal once the diameter has surpassed the critically capillary length of 2.71 mm. For superhydrophobic, rough surfaces, researchers have observed steady state conditions where average droplet diameter for coalescence was 10 ± 2 μm, 30× smaller than the droplet capillary length[111]. Once droplets coalesce and shed, they create regions for fresh condensation to occur, ideal behavior of a candidate surface for air conditioning evaporator coil fins. This behavior can be observed in Figure 46 and is one set of experimental results from condensation testing in the following chapter.

6 Chapter: Condensation Testing

6.1 Introduction and Background

Condensation phase change is a topic of wide interest with applications ranging from desalination and water harvesting to heat exchangers, air conditioning and refrigeration[9,69,108,112]. Water will condense on a given surface in either a filmwise or dropwise condensation mode depending on the surface energy and chemical or morphological modifications of the surface. In general, high surface energy substrates will exhibit hydrophilic behavior and form water films with low contact angles. Low surface energy substrates will exhibit hydrophobic behavior with water condensing as droplets with contact angles greater than 90°. It has been widely demonstrated that dropwise condensation has up to 5–10 times better heat transfer performance than filmwise condensation due to improved water shedding creating fresh surface for further condensate nucleation and droplet growth to occur[9,60]. Chemical functionalization and surface roughening techniques have been heavily researched as means to promote surface hydrophobicity with improvement in water shedding of droplets smaller than the capillary length scale as the contact angle of the surface is increased. Superhydrophobicity, or a contact angle greater than 150° is difficult to achieve on a smooth surface with chemical functionalization alone. However, with the addition of micro, nano, or hierarchical micro and nano surface roughness, contact angles approaching 180° have been achieved.

There are two widely used classical theories of wettability on rough surfaces – the Wenzel and Cassie–Baxter models[32,33]. Both introduce the concept of an apparent contact angle corresponding to the amount of surface area encountered by a droplet on a surface. This apparent angle is greater than the intrinsic contact angle associated with an equilibrium energy balance of the three-phase contact line between liquid, solid, and vapor phase if the surface is already inherently hydrophobic. Wenzel wetting occurs when the droplet penetrates and fully wets the surface asperities leading to a pinning effect and poor shedding or hysteresis behavior. Cassie–Baxter wetting occurs when the droplet is suspended on top of the roughened features and has good shedding behavior and low hysteresis values. In nature, plants such as the lotus, have surface roughness that enables the Cassie–Baxter wetting mode for droplets, leading to improved shedding, superhydrophobicity, and self-cleaning. The superhydrophobic behavior, dropwise condensation, and good shedding capability are desired for candidate surfaces for an air conditioning system, and the following condensation experiments look to those characteristics as success criteria.

6.2 Materials and Methods

In this study, three cases of ZnO nanostructured surfaces were grown on a flat aluminum substrate, on varying micropillar array geometries and on varying microdome array geometries[71,73]. The surfaces were characterized using static, dynamic and condensation properties and those results were reported in Chapter 3.

In order to characterize the dynamic condensation and droplet shedding, condensation experiments utilizing optical microscopy were performed to observe the structures in conditions simulating exposure to incoming tropical air. A custom-designed and built closed-loop wind tunnel test setup, described in Chapter 4, was used with air inlet conditions of 60–80% RH generated by an upstream nebulizer, 26–30°C temperature and 2 m/s air flow. Samples were initially placed on a back-cooled aluminum holder maintained at 4 °C and allowed to thermally stabilize before air speed and humidity were introduced. Video was recorded up to a 30-minute duration to allow for observation of early nucleation and coalescence as well as longer term behavior — stable dropwise, partially flooded, or fully flooded modes, depending on the particular surface. Video recordings were then assessed and analyzed for droplet size distribution as well as condensate area fraction and accumulated volume over time.

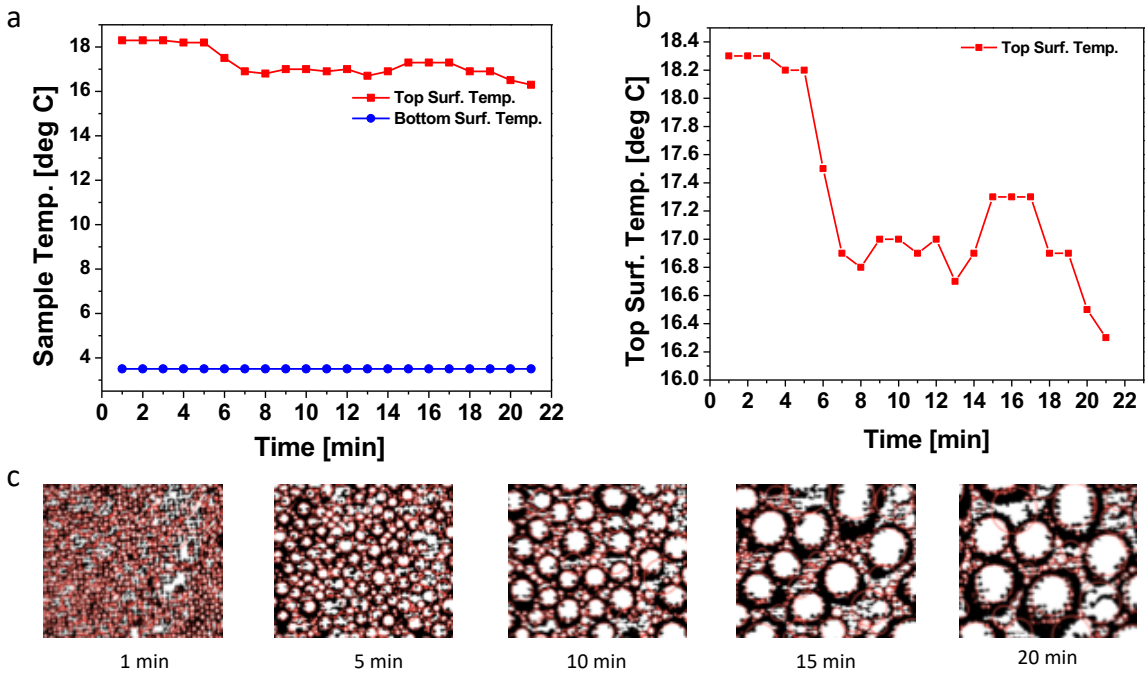

Figure 47: RTD Temperature testing. a) RTD temperature measurements over time for both the surface top and bottom of a sample mounted in simulated test experiment conditions and subjected to convective heat transfer on the air side and conductive heat transfer on the mounted side. b) A closer look at the top surface temperature of the sample over time. c) Condensation footage with identified droplet regions that correspond to the total duration of the RTD temperature testing.

Before full testing, however, an RTD (resistance thermal detector) was placed on the surface of a dummy sample and a full condensation experiment was performed in order to record the sample surface temperature over the intended extent of the experiments. Early samples of the aluminum-sputtered PDMS did not exhibit any condensation. It was surmised that the PDMS was too thick and was conducting too slowly to reach a stable temperature below the dew point of the air, due to the high thermal impedance of the PDMS relative to metallic materials, and the magnitude of the convective heat transfer from the warm, incoming airflow. Subsequent samples of aluminum-sputtered PDMS were fabricated to limit the PDMS thickness to around 1.2 mm to reduce the thermal resistance. Using thermal paste, an RTD was mounted onto a dummy sample of the reduced thickness PDMS and taped onto the aluminum mount. It was found that the aluminum mounting block maintained a stable temperature of 3 ℃ and the surface of the sputtered PDMS sample achieved a stable temperature of 16.5 ℃ over the duration of an experiment (Figure 47).

6.3 Results and Discussion

Following the static and dynamic contact angle characterization, samples were evaluated in condensing conditions. It was observed that after ~25 minutes of condensation testing with the humidity and temperature conditions described previously, the pillar and flat control surfaces showed surface flooding and complete wetting (filmwise condensation). Some of the dome surfaces also exhibited this behavior. However, it was observed that the dome structure with the 30 µm:30 µm size:gap geometry most successfully demonstrated stable, long-term dropwise condensation behavior (Figure 48b) while the pillar features of the same size experienced flooding similar to the purely nanostructured sample (Figure 48a). Multiple experiments of the 30:30 geometry were successfully performed in the same condensation environmental setup to verify the repeatability of dropwise condensation results.

In Figure 48a, the micropillar patterned samples with varying gap sizes were compared with the purely nanostructured case for condensation periods lasting up to 25 minutes — when longer-term condensation behavior became apparent. Time intervals throughout the condensation were observed and compared for effects in droplet growth and coalescence behavior. For the pillar structures, the early condensation behavior was similar across all gap sizes and when compared with the nanostructured case. At the 12-minute mark, which we consider “mid-term” condensation behavior, the largest gap size and nanostructured samples had larger droplet formation or an indication of more coalescence events. By the 25-minute mark or “long-term” condensation behavior point, all pillar samples as well as the nanostructured case exhibited flooding behavior.

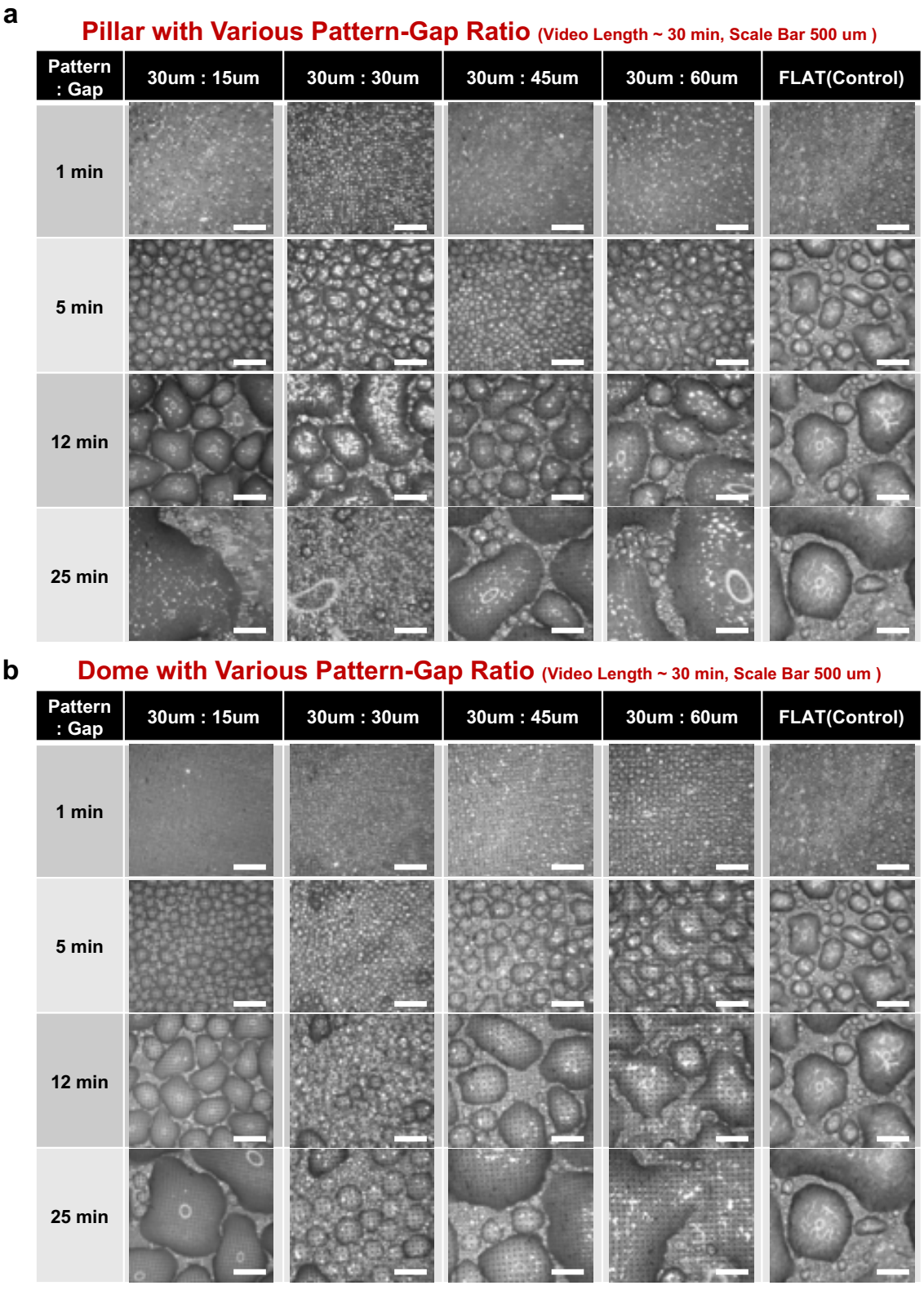

Figure 48: Condensation performance results of square pillar and microdome arrays with various pattern-gap ratios. Recorded video length was 25 min. Scale bars are 500 μm.

For the dome structures in Figure 48b, initial condensation growth appeared to occur primarily in between the features, the flat areas being more energetically favorable for nucleation than the highly curved sides of the dome. In observing the early term behavior of all samples, nucleation and incipient condensation appeared to occur in an ordered manner based on the feature array — for the pillar features, this occurred between the features as well as on the flat, top surfaces. In early behavior at the 5-minute interval, an ordered array of droplet formation could be seen for all gap sizes, which indicates droplet condensation aligning with the microdome feature spacing. Unlike the flat and pillared cases, the mid-term behavior for the smaller gap sizes of 15 and 30 μm retained small-size droplet presence and no flooding. However, with the increase in gap size, the wetting behavior resembled the flat case of larger, coalesced droplets. The smallest gap size case had several more features interacting with the droplet per unit of surface area. However, the 15 μm spacing appeared to inhibit shedding due to the smaller gap size between features. Although the mid-term behavior had a smaller droplet size, significant droplet growth eventually occurred for the long-term behavior. In addition, the larger gap sizes, in particular the 60 μm case, demonstrated flooding behavior as the increased space between features approached the flat, purely nanostructured case. However, equal diameter and equal gap were the best for continuous, stable dropwise condensation. The 30:30 dome case maintained dropwise condensation at droplet sizes less than the capillary length for water and demonstrated continuous shedding at small sizes allowing for a larger surface area available for heat transfer. It is interesting to note the superior dropwise behavior of the 30:30 case compared to the remaining 30 μm diameter dome cases, the 30 μm length pillar cases, and the ‘flat’ case with the silanized ZnO only. Macroscopic images were taken of samples at the 30-minute mark of testing to emphasize the condensation effects. (Figure 49).

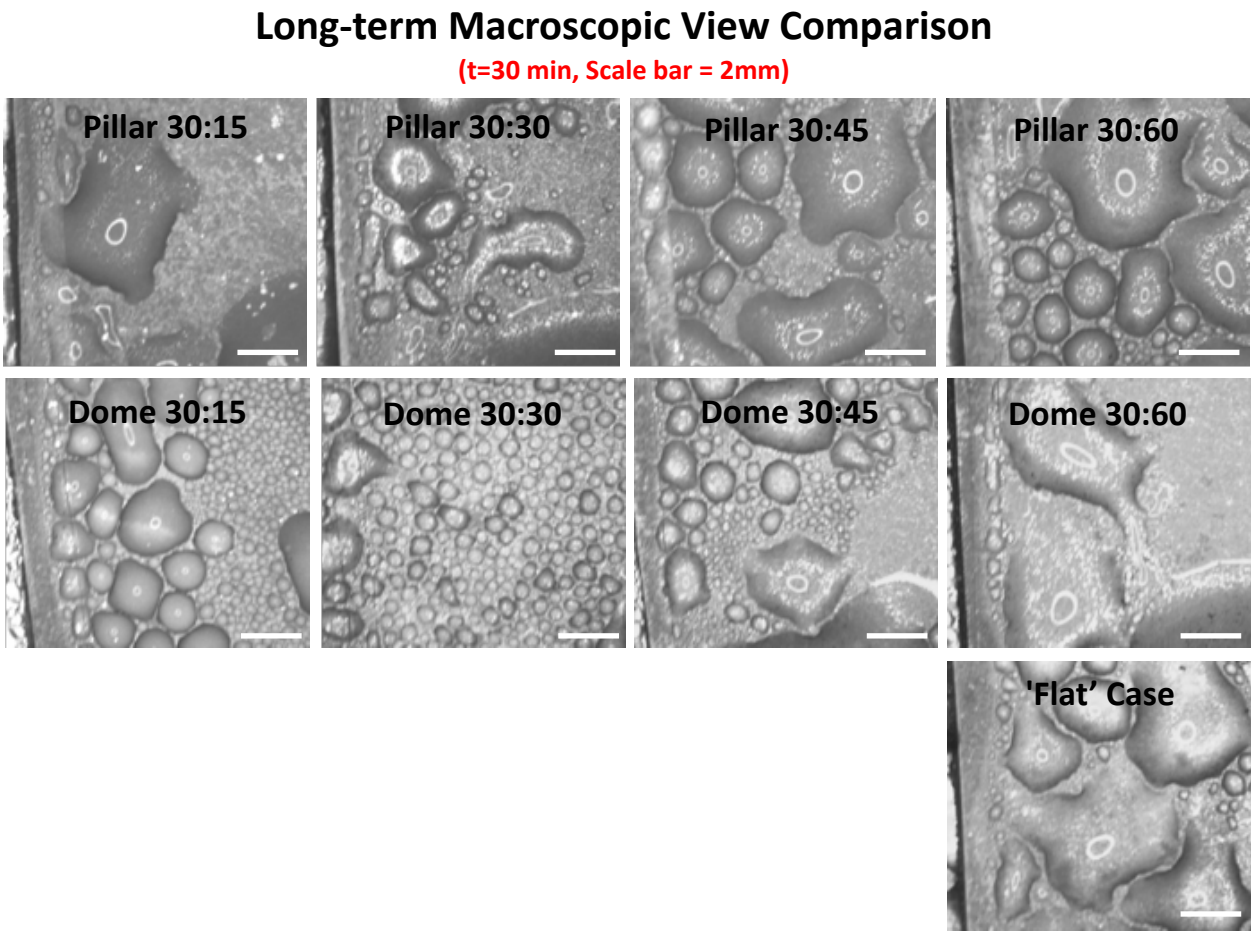

Figure 49: Macroscopic video stills of the long-term condensation behavior at t = 30 min for each of the 30 μm diameter or 30 μm length features compared to the 'Flat' case with a scale bar of 2 mm.

6.4 Image Analysis

In order to further evaluate the improvement in dropwise condensation behavior of the 30:30 dome pattern when compared to the pillar equivalent and purely nanostructured surfaces, the video data from the condensation footage were used to determine a droplet size distribution as well as the area fraction of the total surface covered by condensation. With a front-facing image and given the video resolution quality, the droplet volume and contact angles with the surface could not be accurately determined. However, distinct droplets could be identified, and a radius distribution could be determined through 2D-image analysis techniques. An image analysis algorithm was developed and used to identify droplets over the course of the video and record their size distribution as well as the area of surface covered by condensation compared to condensation-free area. For the early and mid-term condensation times, the domes, pillars, and nanostructured samples all had comparable condensate area fractions for the 30:30 cases, as was also shown in the images taken from the video recordings.

The image analysis algorithm was written in MATLAB and utilized some of the built-in Image Analysis Toolbox features. The algorithm was designed to take an input of a video still image and evaluate the condensation video footage for comparable wettability data. Distinct droplets were able to be identified and a radius distribution could be determined through 2D-image analysis, including looping through various thresholding techniques as well as a watershed segmentation technique in order to better segment the image to distinguish droplets from the background surface and microfeatures underneath them. The segmentation techniques allowed for larger droplets to be detected for mid-term condensation events. Without proper segmentation, the darker spots from light diffraction left by the microfeatures were treated as separate droplets by traditional image boundary detection techniques. This caused miscalculations in droplet radius distribution analysis as well as condensate area fraction calculations. By additionally converting to a binary image after a certain sequence of steps, the edges of the droplets could be better identified.

In more detail, the original colored image was cropped and converted to black and white. The cropping was performed to select the middle of the recorded image due to video quality and resolution being better focused in the center. The result was converted to grayscale and run through two global thresholding processes. The first was an adaptive histogram equalization function that enhanced the contrast of the grayscale image using a contrast-limited adaptive histogram equalization (CLAHE) to transform the values of the color matrix associated with the picture[113,114]. The next threshold step used the graythresh() command, an implementation of Otsu's method for minimizing variance between variables of the same class[115]. After enhancing the contrast of the image pixels, this step minimized the difference in values between adjacent intraclass regions. The result was converted to a binary image and a 'hole fill-in' command was used to fill in any regions of color enclosed within a region of the opposite color.

The resulting image was then fed into a watershed segmentation algorithm that allowed for better distinction of droplet and non-droplet regions[116]. The watershed transform function is also built into the MATLAB Image Analysis Toolbox. MATLAB has set up the function to avoid over-segmentation, which occurs with a general watershed segmentation algorithm due to the identification of any local minima as a distinct region. It identifies the desired objects as catchment basins, minimizes local minima, and uses a distance transform to roughly separate touching objects from being identified as a singular object. The resulting image is highly segmented and broken into distinct regions based on identification of black and white pixels.

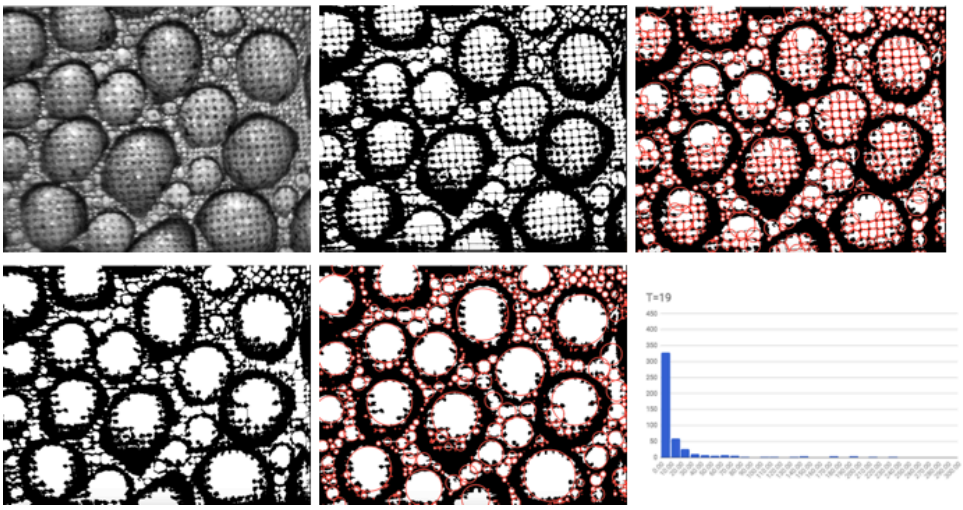

Figure 50: A step-by-step breakdown of the thresholding, watershed segmentation, and filling steps to better approximate accurate droplet radius size for a given frame during condensation testing, in this case, at t = 19 min in a 30:30 trial run. The histogram shows droplet size distribution.

The segmented image was then re-input into the first section of code that included filling in holes based on pixels in a given region and the adjacent region. The result was an image that had filled in most of the underlying microfeatures so that the larger droplets were identified as complete droplets rather than separate regions from the features. This allowed for larger droplets to be successfully identified. All steps are shown in Figure 50 with a sample droplet radius distribution plot for the time point as an example.

The same algorithm was also applied to the pillar samples as shown in Figure 51. Although the drops are not perfectly circular, the black and white pixel count could be evaluated, and the circle approximation was able to provide a similar area value when compared with manual evaluation.

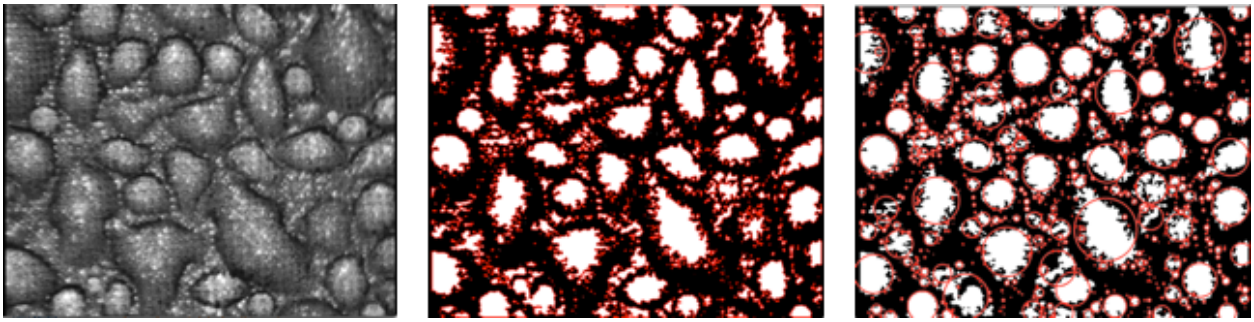

Figure 51: Image analysis algorithm applied to the mid-term condensation testing pillar pattern footage. Contrasting regions are identified from a binary version of the original frame followed by a circle approximation for each identified individual region.

6.5 Droplet Radius Distribution

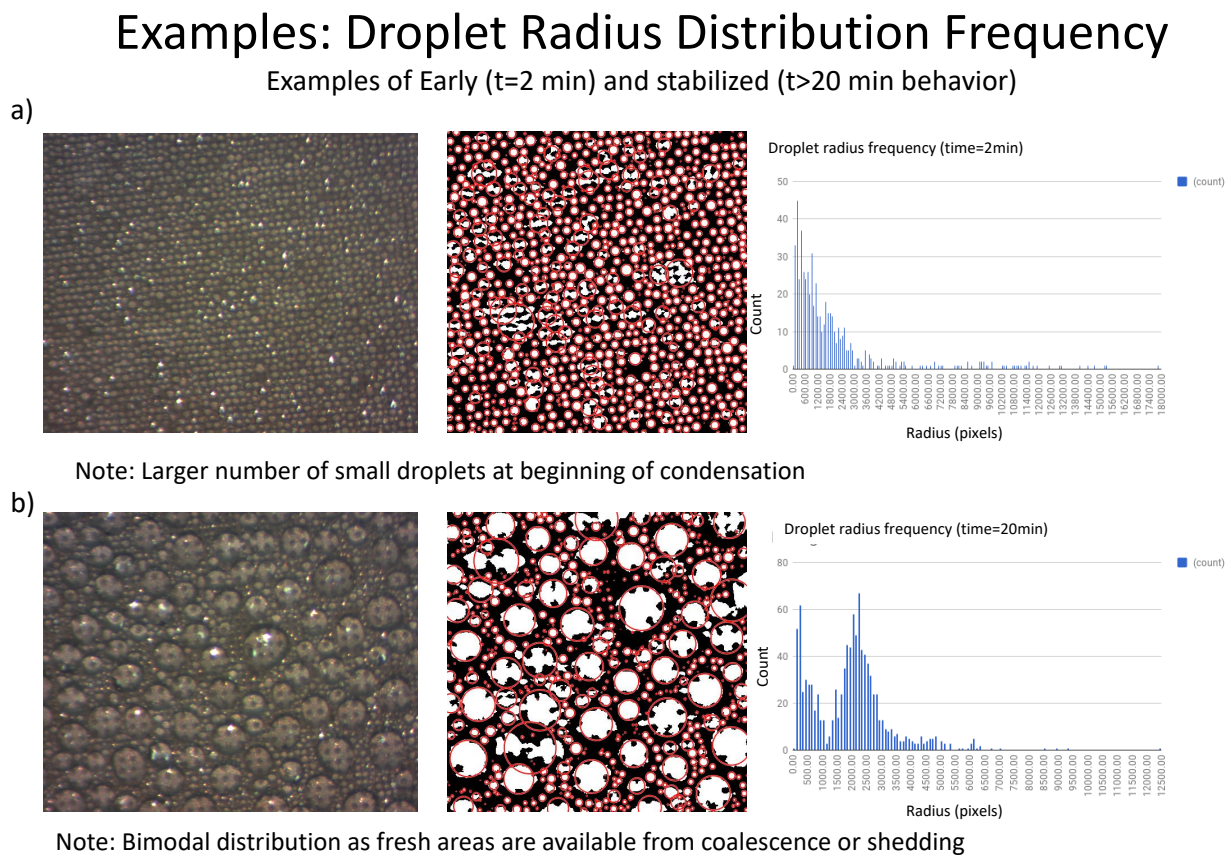

Figure 52: Droplet radius distribution frequency examples showing the original video footage, the droplets identified by the image processing algorithm, and the resulting frequency plot. a) Early behavior at t = 2 min b) Long-term behavior at t = 20 min showing a bimodal distribution of radii.

Based on the circle identification component of the analysis, a droplet radius distribution for different times could be determined. Some interesting observations can be seen in the droplet radius distribution from the condensation video data in Figure 52. Most notably, there is a large peak of small-radius droplets seen at the initial condensation phase. Before droplets have grown enough to coalesce, they nucleate on the surface in whichever regions are most energetically favorable. As they grow, the droplets continue nucleating on fresh surface from vapor from the air, and once they are able to touch an adjacent growing droplet, they merge. The newly formed droplet has the same center of mass as the previous two and will often bead, shrinking its boundaries on the aluminum, to minimize the total energy of the three-phase system. This shrinkage allows for the area surrounding the freshly merged droplets to be temporarily droplet-free and provide a new surface for further nucleation. Evidence of this phenomenon can be seen in the bimodal distribution of the stabilized dropwise condensation behavior in Figure 52b. A large number of droplets coalesce and have greater radius values. However, because of the

coalescence, a higher quantity of small-radius droplets occurs in the fresh condensation sites.

6.6 Condensate Area Fraction

Beyond the droplet radius distribution, the image analysis algorithm allowed for condensation area fraction plots to be determined based on the identified droplet regions subtracted from the entire frame. The measured conversion factor for the viewing window was 3.134 mm/1280 pixels or 2.49 μm based on microscope focus. This allowed for area calculations given an 800 $\times$ 800 pixel frame.

Using the same techniques and converting the image to a binary image, the number of white pixels, representing droplets, could be counted over the total number of image pixels to represent the amount of wetted surface. All algorithms were validated and verified by three sets of manual droplet counting.

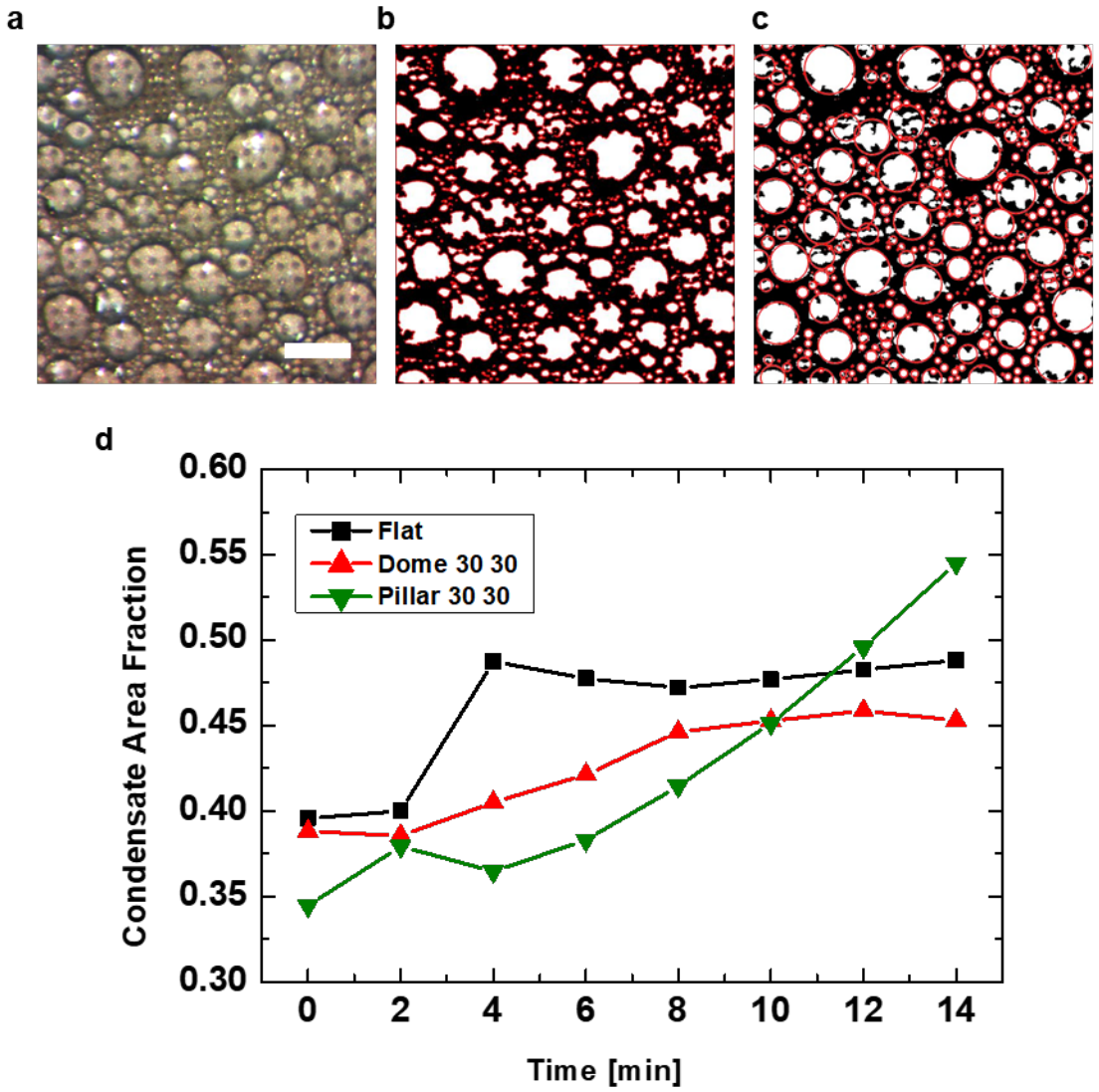

Figure 53: Image analysis breakdown. (a) Condensation performance of a sample of 30:30 microdome video still taken at t = 8 min. (Scale bar 500 μm, sample thickness ~ 1.8 mm, Saturation values (S) = 1.2–1.3, Air temp. ~ 35 °C, Surface temp. ~ 16.5 °C, RH ~ 40.6%, Air velocity ~ 3 m/s.) (b) Droplet boundary detection of the processed droplet image . (c) Fitted droplet diameters superimposed on image as circles. (d) Extracted condensation performance of a 30:30 micro-dome and micro-pillar samples versus a "flat" sample for a 14-minute experimental duration.

Going into more depth with the condensate area fraction analysis, in Figure 53b, the binary image has gone through the image modification steps; and white regions, representing droplets, have been circled to indicate what a typical edge detection algorithm would have achieved. The problem here lies with the dome and pillar features which prevent the droplet from appearing more circular. However, the dome and pillar features, though visible in the black and white image, do not vary the apparent droplet diameter. In Figure 53c, a region area detection block of code was used to find the centroid of a given region, determine the radius and area of a circle associated with that

region, return the radii values into a spreadsheet, and draw the calculated circles overlaid on the black-and-white image to check if the code had properly identified the droplets. The total area of all identified circles was then subtracted from the total area of the image to provide data for a condensate area fraction, or the fraction of wetted area per image. In Figure 53d, this analysis has been performed for the early behavior of the dome, pillar, and flat case surfaces, showing that initial condensation is similar between the three. However, while the 30:30 dome array remained in dropwise mode for long-term behavior, the pillar and flat cases became either covered in amorphous blobs of water or completely flooded due to coalescence and pinning, preventing droplet shedding from occurring. The circle approximation algorithm was no longer able to work with non-circular shapes; however, the edge detection was still comparably accurate to Figure 53b.

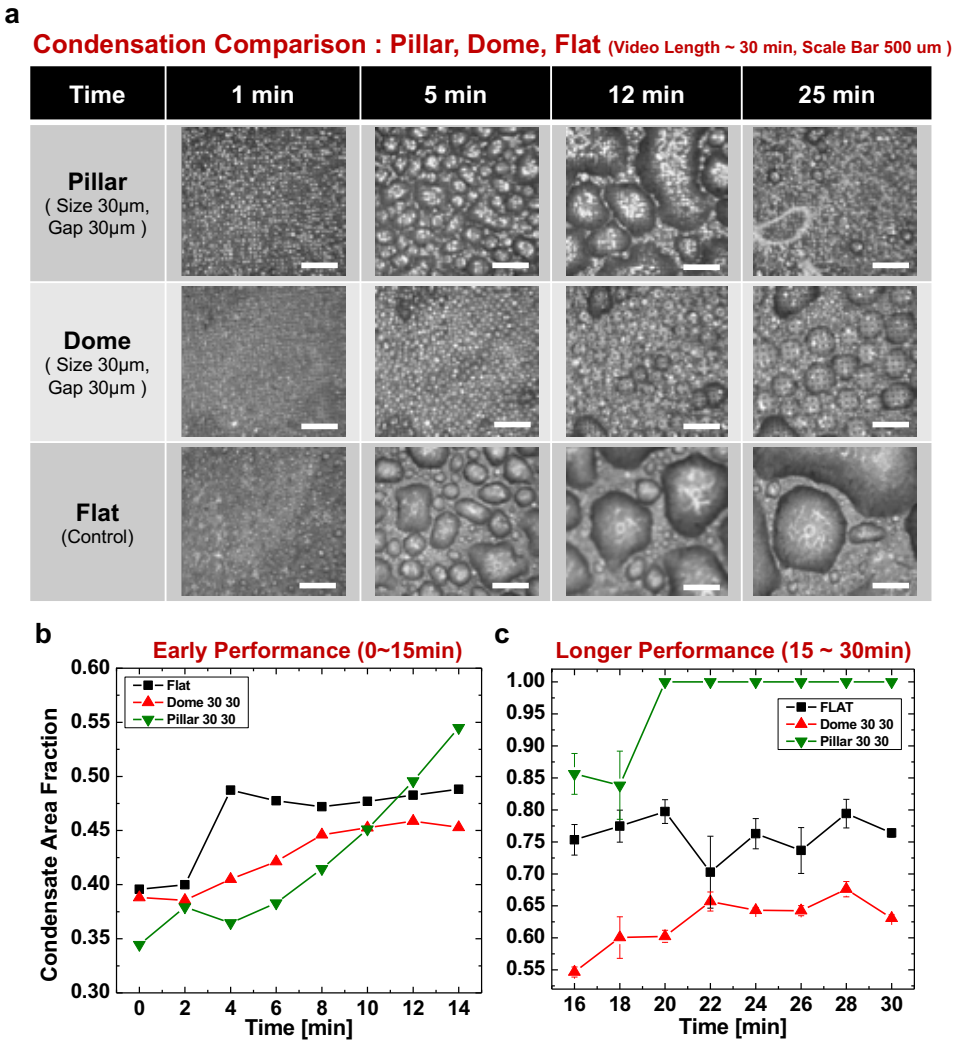

Figure 54: Condensation comparison. (a) For more direction comparison, the dome and pillar 30:30 cases and the 'flat' case condensation testing video stills are shown. (b) The early performance up to ~15 min for condensate area fraction of each. (c) The longer performance from 15 to 30 min for condensate area fraction of each.

While the image analysis algorithm was sufficient for identifying circular area droplets, the circle identification broke down as the surface flooded or amorphous droplets formed from coalescence events. Thus, in order to maintain a consistent analysis method for the dome, pillar, and 'flat' case surfaces that did not all have dropwise condensation, a manual technique was performed to gauge condensate area fraction for each of the samples from the 15-minute mark to the end of the condensation experiment video. The perimeter of the wetted areas was marked and the area consisting of water was subtracted from the total image area. This analysis was performed for the dome, pillar, and flat cases three times each to account for any human error, although a slight jump in condensate area fraction is observed from the algorithm analysis to the human analysis. Despite the percent difference, the pillar, flat, and dome cases still maintained similar trends, and the pillar case reached a condensate area fraction of one, indicating a fully flooded surface. Within the final video frame, the flat case appears to be heading to a more flooded regime; however, the latter part of the analysis reveals a sawtooth graph occurring from droplet growth and merging events that generate some new condensation surface. The dome structure, on the other hand appears to stabilize at the lowest area fraction of the three.

6.7 Accumulated Volume

The accumulated volume plots assumed a spherical cap distribution with the average static contact angle of the sample used to calculate the volume of water per droplet radius. Using a spherical droplet volume approximation based on contact angle:[117]

$$V = \frac{\pi D^3}{24}\left(\frac{2-3cos\theta+cos^3\theta}{sin^3\theta}\right) \quad (33)$$

where D = diameter and θ = measured contact angle, the volume of water could be calculated based on the droplet radius distribution. The obvious breakdown of this method is in assuming that all sizes of droplets have the same contact angle. However, in utilizing the same calculation for all time points and images, the accumulated volume on the surface should follow a trend corresponding to the actual accumulated volume. A second breakdown is when the surface floods and no longer has a radius distribution. This formula cannot be used to calculate volume of a water film.

For the dome and pillar comparison, the 30 μm features of all gaps were chosen to be analyzed based on the success of the 30:30 size:gap sample in stable long-term dropwise condensation and are shown in Figure 55. Each sample was compared to the flat, nanostructured case as well. In the early behavior up to about 7 minutes, the flat case had already accumulated the greatest volume of water. The pillar and dome cases grew the most slowly for the 30:30 case in which the dome sample had only accumulated ~2.3 μL water. However, as the spacing between the features increased, the pillars retained a

consistent lower growth while the behavior of dome samples began to approach that of the flat case.

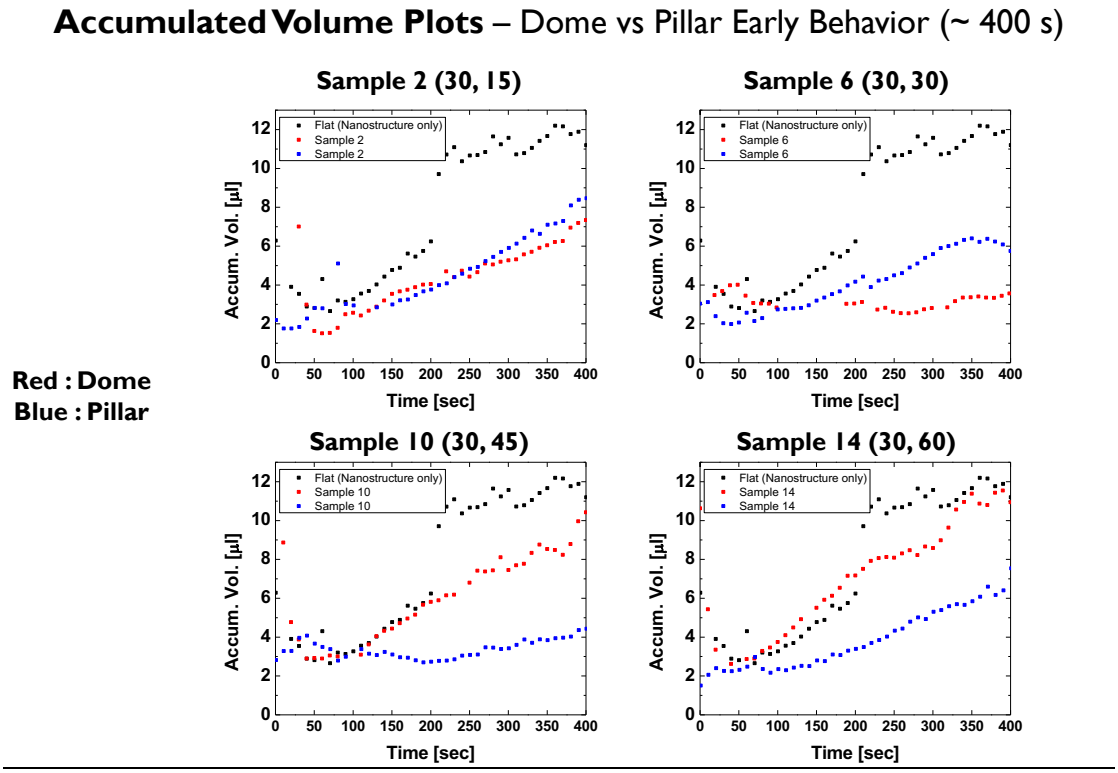

Figure 55: Accumulated volume plots comparing the early behavior (~400 s) of same dome and pillar geometries with the 'flat' case and assuming a spherical cap approximation for the volume calculations.

In next observing not just the early behavior but also up until ~30-minute point, the flat, dome, and pillar distinctions became more apparent and needed to be compared to the direct video footage for accuracy. The most interesting result was for Sample 6, which is the 30:30 case. The dome patterned samples had a slowly increasing trend aligning with the stable dropwise condensation observed. For the other cases as well as the pillar and flat samples, the lower accumulated volume calculation was a result of the fact that the surface flooded and formed a film. While a film would have a lower volume of water than protruding droplets, the complete lack of convective surface for heat transfer was a much higher impediment to cooling efficiency than a larger volume of distinct drops. Thus, while the plots in Figure 56 provide insight into total water volume, they do not guarantee that a lower accumulated volume would have better heat transfer performance in the event that it is due to filmwise rather than dropwise condensation.

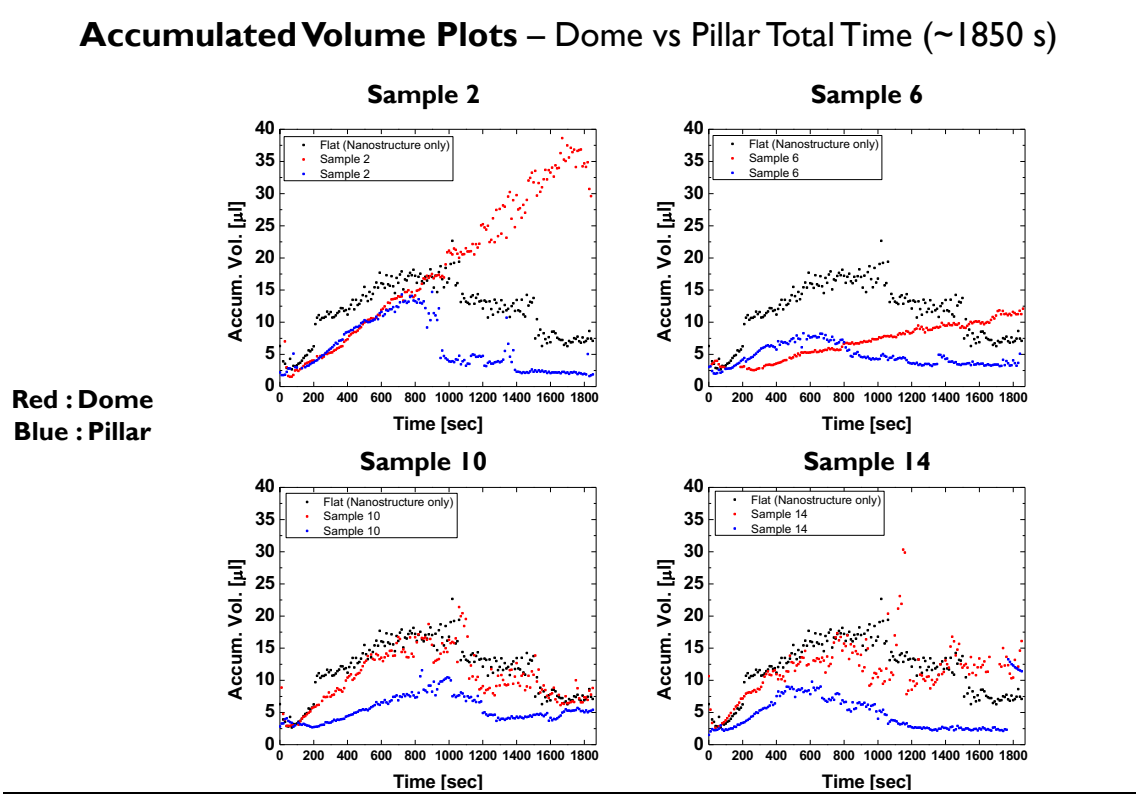

Figure 56: Accumulated volume plots comparing the long-term behavior (~1850 s) of same dome and pillar geometries with the 'flat' case and assuming a spherical cap approximation for the volume calculations.

In a final comparative set of plots in Figure 57, all four samples of the 30 µm geometry and the flat sample were superimposed on the same graph with the short term and full-length experiments being distinguished. The short-term accumulated volume is greatest for the flat case, as mentioned before. Interestingly, the pillar samples tended to experience accumulated water volume growth more slowly at early stages than their dome counterparts. There is no distinct trend based on gap sizing in the initial behavior. For the longer-term growth, it becomes more obvious when also comparing to the video footage that all of the pillar samples flooded and had a decreased accumulated volume. For the domes, the smaller gap sizes did not experience flooding. As a result, Sample 6, which is the 30:30 case, showed a slowly increasing trendline; and Sample 2, the 30:15 case, showed a significant increase in accumulated volume due to coalescence of large droplets on the surface that remained pinned within the smaller pores.

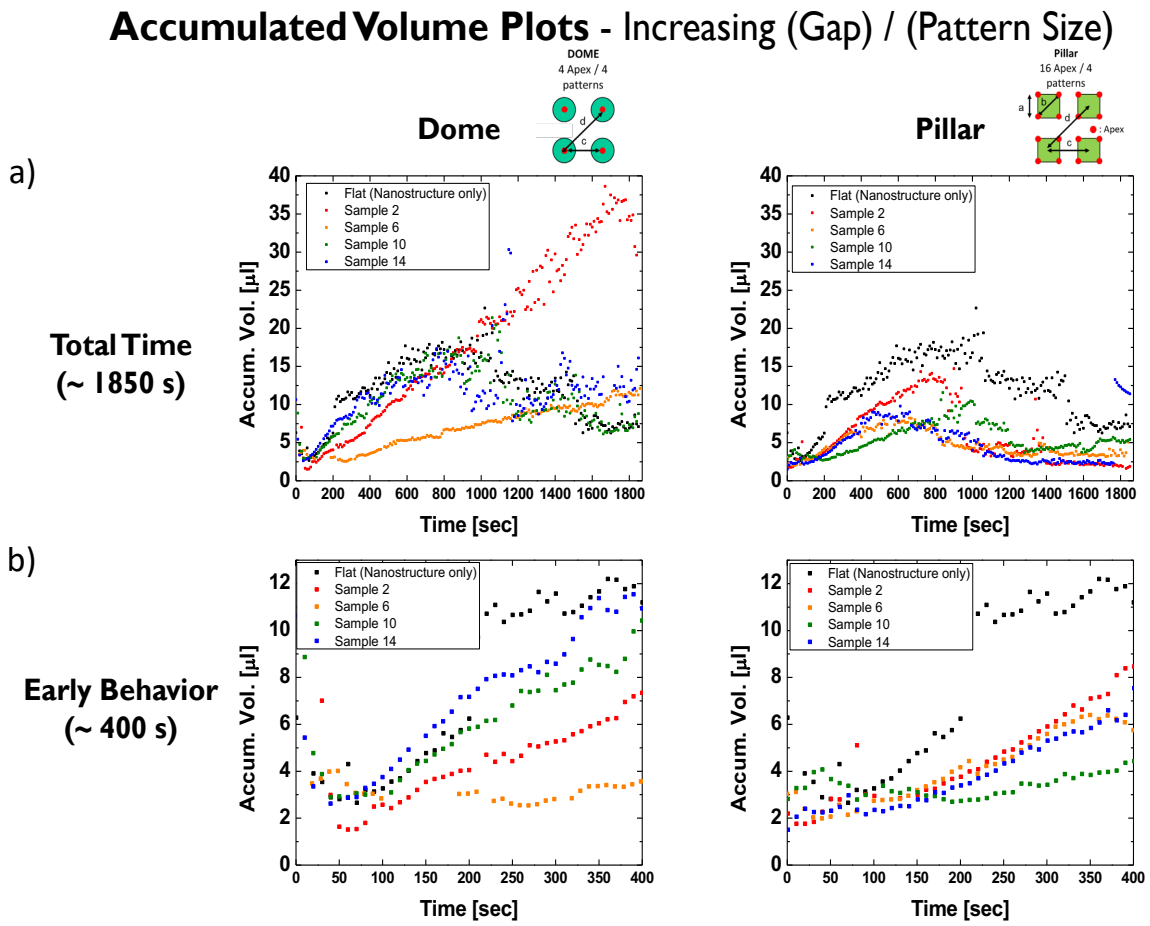

Figure 57: Combined accumulated volume plots comparing (a) the long-term behavior (~1850 s) of all of the 30 μm dome samples with the 'flat' case and all of the 30 μm pillars with the 'flat' case and (b) the early behavior (~400 s) of all of the 30 μm dome samples with the 'flat' case and all of the 30 μm pillars with the 'flat' case again assuming a spherical cap approximation for the volume calculations.

6.8 Conclusion

Although the lotus leaf geometry is often lauded as one of nature's best water shedding surfaces, drops will typically land on the leaf surface in a top-down manner. However, loss of superhydrophobicity in lotus leaves has received some attention when the droplet growth is bottom-up or nucleated from the surface itself[22,109]. Nucleation will occur in energetically favorable locations, for example regions of the fabricated surface with point defects or regions with a lower free energy barrier such as hydrophilic regions. For the domes, droplets appear to be able to nucleate in between and on the features but are not able to coalesce preferentially on the sides or tops. For the pillar structures, nucleation and coalescence appear to occur in between the features as well as on top of the features. This difference leads to a larger number of potential nucleation sites as well as an increased likelihood of droplet coalescence events on the pillared surfaces as opposed to the domed surfaces. In addition, the Cassie–Baxter effect of droplet

suspension on top of the features can be lost in a bottom-up condensation process because the pores may already be filled by condensed liquid. Apparent contact angles are lowered, and droplets become more easily pinned within the features, which inhibits shedding. By comparing varying gap sizes with respect to feature size, the existence of a critical size could be observed in which droplet growth would be limited and average droplet size for long term condensation behavior would be small and not prone to surface flooding.

This type of bottom-up condensation testing is relevant and useful when evaluating surfaces for air conditioning performance, because an air conditioner fin will experience a continuous wetting environment through condensation due to the cool surface meeting the warmer inlet air. The observed video results from the microdome, micropillar, and nanostructured surface comparisons indicate that a microdome pattern of 30:30 μm size:gap for the dome creates a wetting situation of stable, small, dropwise condensation, ideal for heat transfer performance. Although a pillar surface of comparable dimensions was analyzed, the lower radius of curvature of the dome feature compared to the sharp corners of the pillars allowed for lower pinning forces and better dynamic shedding behavior of the dome surface. Condensate area fractions taken from video analysis also demonstrated this stable long-term behavior.

7 Chapter: Scaling the Process

While fabricating surfaces with unique morphologies and characteristics is useful from the perspective of scientific advancement, the manufacturing and scalability of such surface modifications is often overlooked. The superhydrophobic surfaces and geometries described in previous chapters were shown to exhibit superior condensation and droplet shedding capability; however, all samples were created on a lab scale of 1 cm by 1 cm double-molded PDMS with sputtered aluminum to emulate aluminum evaporator coil fins. The original method of double-casting PDMS to fabricate microstructures was useful for testing multiple geometries with quick throughput; however, this process could not be used for large-scale manufacturing. A primary goal of this project was not only to characterize and fabricate superior wetting surfaces but also to scale the manufacturing to test with a full-scale evaporator coil. Based on results from the early pillar and nanostructured ZnO work, it was determined that scaling the hydrothermal growth rather than the microstructure fabrication method would be the most cost-effective means for coating a full coil. Methods for scaling microstructure fabrication were investigated. These included roll-to-roll processing which would be possible by designing a steel roller for sheet metal modification. The disadvantages to this process would be usage wear on the roller, the limitation of only one micropattern due to cost of roller production, the upfront cost of manufacturing a roller as well as designing and testing a full sheet metal process, and an inability to retrofit existing fins. Embossing, coining, knurling, and imprinting methods were also investigated and had similar drawbacks to roll-to-roll processing.

7.1 Synthesis and Characterization

The hydrothermal synthesis process used for the ZnO nanowire growth utilized a very low concentration of chemicals: 25mM of zinc nitrate hexahydrate and hexamethylenetetramine. Any fumes generated by the process as well as waste disposal were fairly simple to handle with a fume hood and ventilation system as well as chemical waste disposal service. In addition to scaling the hydrothermal process, the silanization or chemical functionalization step also needed to be scaled. Various methods were also investigated for this step of the process including CVD, dip coating, and spray coating.

Although the optimized ZnO nanostructure growth conditions were optimized at 70 °C, 25 mM, and 1.5 hours for the lab-scale condensation testing, a sweep of temperature, concentration, and growth time conditions was performed and tested for condensation performance before committing to a full-scale coil fabrication. The various conditions included 50 °C, 60 °C, and 70 °C, 1.5 hr, 3 hr, 4.5 hr, and 48 hr growth, and 10 mM, 17.5 mM, and 25 mM solution concentrations. Sheet stock alloy of 6061 aluminum was purchased from McMaster-Carr and cut into .75 cm by 2 cm pieces for growth condition testing. Before placing in the growth solution, samples were rinsed with acetone, IPA, and DI water to remove any organic material. The aluminum samples were kept in a same

temperature environment as the eventual synthesis temperature to prevent a temperature drop once added to the solution. Water was preheated before adding chemicals. A sample for each condition was then synthesized, rinsed with DI water, allowed to air dry and then characterized for pore size and growth using SEM images. The results are shown in Figure 58, and the major findings were:

- There was a distinct trend in nanopore size with respect to solution concentration and synthesis time. As the synthesis time increased and the bath temperature increased, the nanowire growth became more dense resulting in a smaller pore size.

- This trend was most obvious for the 50 °C and 60 °C temperatures which both exhibited a large porous structure for the longest synthesis time and lowest solution concentration.

- The 70 °C formed a dense structure for all times and concentrations with less of an obvious trend. This could be attributed to the solution having a faster reaction rate at higher temperatures, thus, generating a thicker layer of nanostructures.

- The 48-hour synthesis was also an interesting case, because although it had one of the more porous structured surfaces, the resulting film was much thicker than other sample coatings, so much so, that the surface was highly prone to cracking. This was deemed unsuitable for any scaling potential.

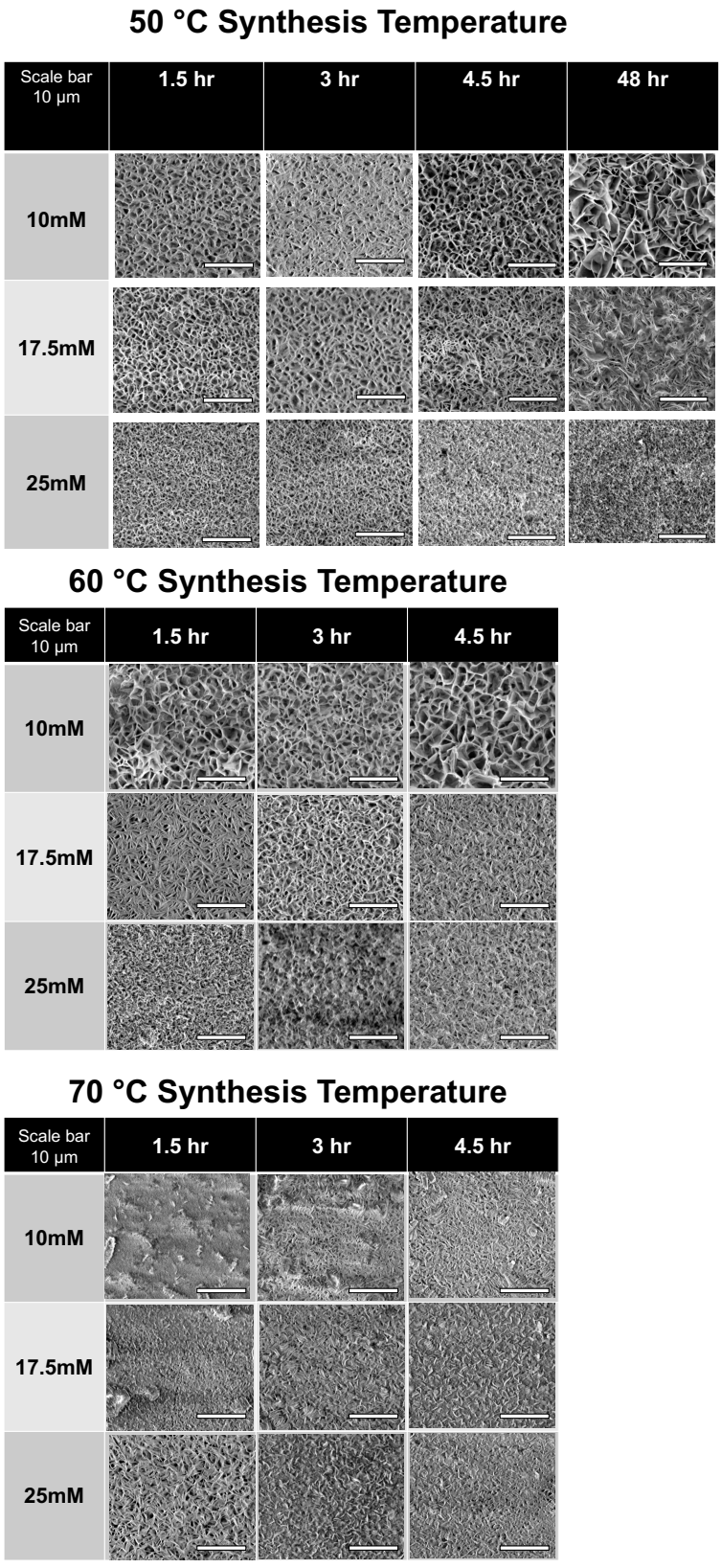

Figure 58: SEM results of the ZnO nanowire growth on the aluminum sheet metal varying temperature, solution molarity, and growth time.

Although interesting trends in terms of pore size were observed for the given growth conditions, condensation tests were necessary to evaluate dynamic wetting conditions for each of the samples. Prior work with the nanostructured synthesis at lab scale had demonstrated that the most superhydrophobic surfaces were not necessarily the best in dynamic condensing and coalescing conditions[22,118]. For each sample, a condensation test was performed at 65–70% RH, 26–30 °C air temperature, 4 °C chiller temperature, and the fan powered off. Video was recorded for each sample until ~25 minutes or else full flooding behavior. It was observed that the more end-case conditions of 50 °C, 17.5 mM and 1.5 hr synthesis and 70 °C, 25 mM, and 4.5 hr synthesis had the best dropwise condensation performance with the latter providing slightly better coalescence behavior. While droplets did not have the same force impetus for shedding from air shear, coalescence events helped to distinguish performance by either causing flooded surfaces or else creating fresh heat transfer and condensation surface by shrinking toward the center of mass of the collective water volume and reducing the sample surface contact (Figure 59).

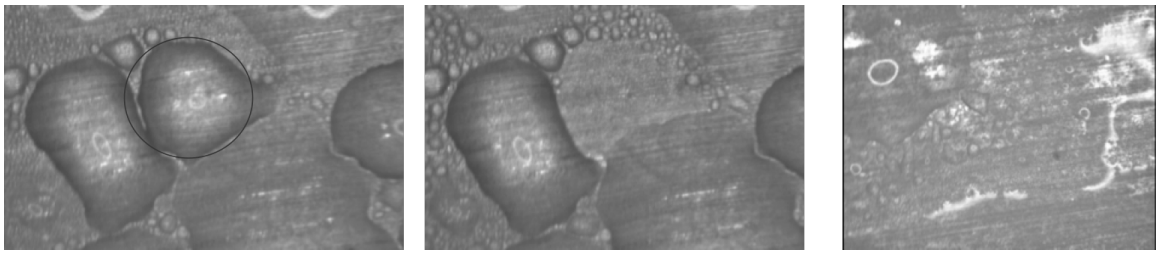

Figure 59: Droplet shedding event during condensation testing of the various sheet metal samples from the synthesis parameter sweep.

7.2 Scaled Hydrothermal Synthesis Setup

After determining that the best test condition for full-scale coil synthesis would be the 70 °C, 25 mM, 4.5 hr synthesis, a process was devised to synthesis ZnO nanowires and silanize a full-scale coil. A custom coil was designed and fabricated based on dimensions for a collaborative test setup at NUS in Singapore where the post-processed coil will be sent for heat transfer testing. With the given dimensions, a ceramic vessel was obtained for the bath synthesis. As shown in Figure 60 the vessel was insulated with vermiculite to retain heat during the heating synthesis process and placed in a walk-in fume hood. It was determined that a 32-gallon DI water bath would be necessary, requiring approximately 900 g zinc nitrate hexahydrate and 423 g of hexamine. Three separate PID-controlled immersion heaters with circulation capability were used to heat the bath to ~190 °F. A cover was placed on top of the bath to minimize evaporative losses during the heating process. Once the bath had reached the required temperature, the chemicals were added and sufficiently mixed to dissolve into solution. The coil was then added to the bath which dropped the temperature to the correct synthesis value of 158 °F. The heaters were then adjusted to this temperature and were confirmed to maintain bath temperature for the duration of the process.

Figure 60: Scaled hydrothermal bath setup with a ceramic, insulated tub for processing.

After the 4.5-hour synthesis had completed, the coil was removed, rinsed with DI water to remove any additional ZnO precipitate and allowed to air dry for a few days to ensure that water had sufficiently evaporated. As can be observed in Figure 61, a white coating had formed on the edges of the fins.

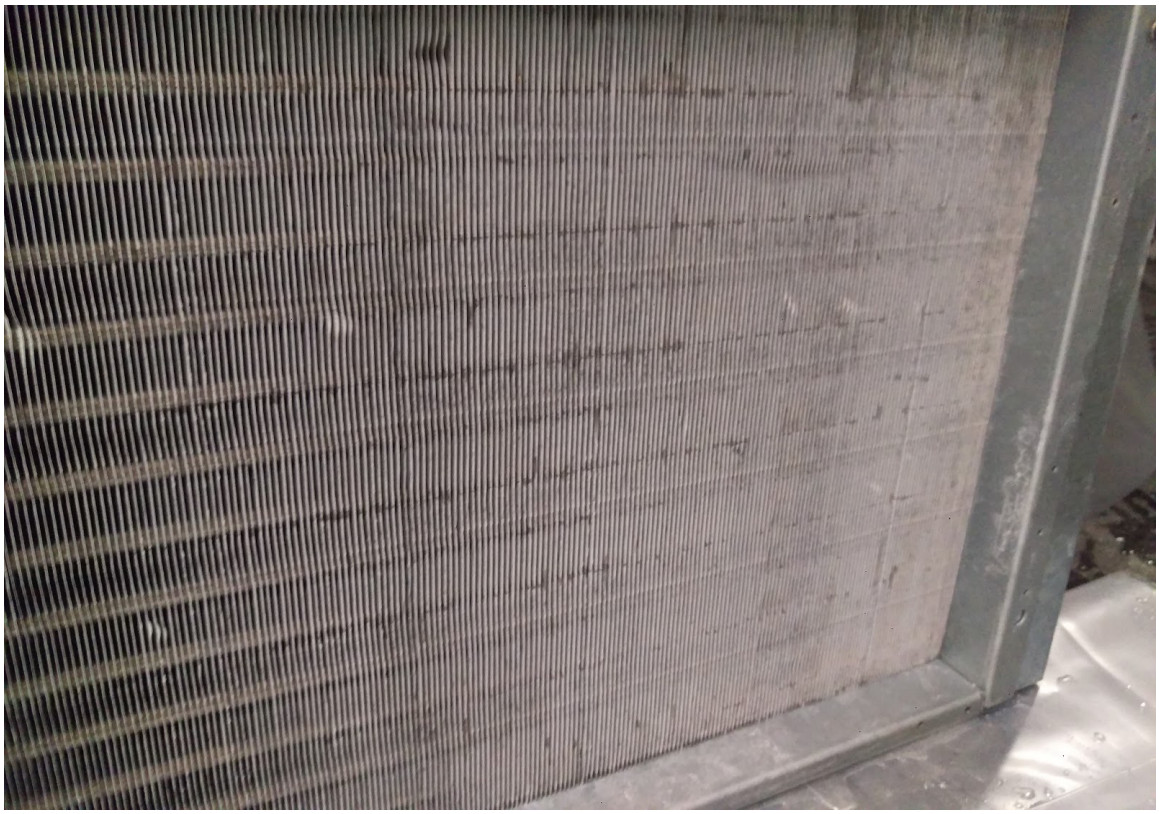

Figure 61: Evaporator coil aluminum fins after hydrothermal coating process. The whitish coloring is indicative of successful ZnO growth.

In order to ensure that the fins were, in fact, fully coated, a test coupon of 6061 aluminum of similar height was placed in the bath synthesis (Figure 62). It was visually determined that the test piece was fully coated.

Figure 62: Test coupon of aluminum sheet metal to verify ZnO coating.

7.3 Scaled Silanization Setup

In addition to scaling the bath synthesis, the silanization process was also scaled. 1H,1H,2H,2H-Perfluorooctyltriethoxysilane was chosen based on its average surface contact angle (104 degrees) for a flat surface and its off-gassing potential of ethanol instead of chlorine which occurred with the previously utilized compound of Trichloro(1*H*,1*H*,2*H*,2*H*-perfluorooctyl)silane. Chlorine gas can dissolve zinc, so this would have been less than ideal for a large ZnO-coated surface.

Three different techniques were investigated to perform this step: chemical vapor deposition, dip coating, and spray coating. Chemical vapor deposition (CVD) is the preferred method for silanization at lab scale. Utilizing a vacuum bell jar, 2–3 drops of silane are placed on a glass slide in the jar along with the samples. A pumpdown process to approximately 10^{-2} to 10^{-3} Torr is performed for 20 minutes, and the pump is turned off for an additional 40 minutes to allow vapor deposition of the evaporated silane molecule. 1H,1H,2H,2H-Perfluorooctyltriethoxysilane has a vapor pressure of around (.0102 Torr). For the bell jar process, enough of the molecule typically evaporates to sufficiently coat a lab-scale surface. For a full-scale coating, however, a much larger vessel would be needed to provide a sufficient vacuum chamber. A 55-gallon drum was obtained and converted into a vacuum chamber with a vacuum pump to perform the silane process (Figure 63).

Figure 63: Steel drum CVD test for silanization.

To ensure that the drum didn't buckle, it was pumped down to –8 to –10 psi gage pressure with –12 psi being the upper limit. The average pumpdown resulted in pressures of ~310 Torr which were significantly higher than the vapor pressure of the silane. It was found that if the drum was pumped down and the silane was left in the chamber with test pieces over a 24-hour period, there was successful surface functionalization in areas close to where the silane drops had been placed in the chamber. Due to proximity effects, molecular diffusion was able to occur to coat a given sample. However, relying on diffusion as a mechanism for surface coating would not be reliable for closely packed fins. The chamber was deemed useful but insufficient for scaling.

A dip-coating process was considered but not tested. Silane is typically dissolved at around 2 wt% in a hydrocarbon solvent such as ethanol or toluene, in order to ensure coating. For a 32-gallon bath similar to the hydrothermal process, those volumes of ethanol or toluene were not desired from a waste management and safety perspective. The same 2% solution with ethanol was thus made and tested as a spray coating instead. Samples of ZnO-coated aluminum were made and sprayed with silane and allowed to dry at room temperature. It was found that the silanization resulted in contact angles greater than 170° and low hysteresis values. A 2-liter solution of 2 wt% silane and ethanol was made[119,120]. By using a spray bottle capable of 45 psi pressure and adjustable nozzle, the fins were coated with several layers of silane from various angles to ensure that both sides of the fins were completely covered. After deposition, the silane was allowed to air

dry in the fume hood. Two coils used in the test fabrication here will soon be tested in a full testbed setup in Singapore to evaluate heat transfer properties.

7.4 Summary

The advantages to the process described above are numerous. A coil can be ‘retrofitted’ with a superhydrophobic, nanostructured coating, the chemical concentrations are low enough to facilitate waste disposal, the chemical quantities used are low cost compared with other coating processes, a ZnO and self-assembled monolayer silane coating are more thermally conductive than traditionally used polymer-based coatings, and the laboratory setup created for this would see even greater cost reductions if implemented at scale.

8 Chapter: Conclusions

8.1 Major Conclusions

The overarching motivation behind this work was and is to come up with a scalable and affordable process for improving air conditioner efficiency. In the earlier work related to the micropillar characterization, fabricated samples were investigated for improvement in static contact angle and hysteresis performance compared to the same structures with nanostructure growth on top as well as a baseline case with no additional morphology. It was found that the hierarchically structured pillar surfaces had higher average overall contact angles than the purely microstructured surfaces and that additional surface roughness did, indeed, improve wettability performance.

It was next investigated whether or not a curved microstructure as opposed to a straight-walled pillar structure would have even better wettability characteristics when tested statically and dynamically. From biomimetic inspiration, a surface pattern was developed that mimicked the lotus leaf geometry. In comparing these hierarchically structured dome surfaces with pillar counterparts, it was found that the static contact angles were similar for both. The contact angle hysteresis was higher for the pillars than the domes and the domes exhibited better roll-off characteristics as a result. Both the dome and pillar structures had higher contact angles and lower hysteresis values than the purely nanostructured baseline surface that was also tested. It is worth noting that the nanostructured samples in the dome and pillar project were notably worse than the nanostructured samples from the Chapter 2 work on the pillars. While the same synthesis process was utilized, the work in Chapter 2 utilized an aluminum-sputtered silicon wafer while the domes and pillars were based on aluminum-sputtered PDMS molds of the patterns. Although, the nanostructures looked the same in SEM images, the same hydrophobicity performance was never realized.

The theoretical, modified Cassie–Baxter model applied to predicting the static contact angle for the domes and pillars was off by a factor of 1.01 compared to the measured samples. Whether this is an arbitrary coefficient or can be attributed to surface geometry would need to be determined in future work. Instead, the Cassie–Baxter model gave a reasonable approximation of the advancing contact angle on the surfaces. In order to predict the receding contact angle, preliminary calculations were performed with a capillary bridge model that used capillary force and energy balance principles to determine a meniscus slope angle and receding angle as a function of the neck radius of the capillary bridge at the point of rupture. The contact radius at the base of the bridge was assumed to be half the nominal feature length for the pillar and half the wetted cap radius for the dome. This was sufficient for initial calculations and produced graphs for each geometry of receding contact angle versus neck radius that included the measured experimental values. However, to predict the receding angle based on this model, a rupture neck radius would need to be calculated for each geometry. Future work would

investigate and include the contributions of pattern density and contact line dynamics in order to refine the receding angle predictions.

This dissertation also reports on the design and implementation of a wind tunnel test bed for a simulated HVAC environment. The tunnel was used in condensation testing for all dome and pillar samples to compare condensation performance over time at a given set of input air conditions. Through testing, it was demonstrated that short term condensation and droplet growth was small and in dropwise mode for all samples. However, as the samples remained in the test conditions for a longer time period, filmwise condensation was observed for all pillar samples, the 'flat,' nanostructure case, and all dome samples except for the 30:15 and 30:30 cases. The two dome cases exhibited stable dropwise condensation behavior for long term wetting. The 30:15 pattern formed large, amorphous droplets but did not form a film. The 30:30 pattern, on the other hand, showed dropwise condensation at droplet sizes significantly smaller than the capillary length of water. These experimental results were successfully repeated. To further evaluate the performance of the 30:30 case and compare it both to the 30:30 pillar as well as the remainder of the 30 μm features with varied spacing, a MATLAB image analysis algorithm was developed to analyze condensation video footage. Condensate area fraction, droplet radius distribution, and accumulated volume plots over time were evaluated for comparison. The condensate area fraction was lower for the dome 30:30 case in the long-term behavior than the flat and pillar cases while the pillared surface experienced full flooding. Accumulated volume plots were not enough to determine the success of a surface — referring to ability to have dropwise condensation and shed droplets at smaller sizes than the capillary length. Indeed, a thin film has less volume than a varying radius droplet distribution. However, the film decreases the heat transfer ability of the surface more so than the droplets. Thus, a lower accumulated volume could mean smaller droplets or a film of water, and the plot would need to be compared to the actual video footage to determine the condensation mode.

After characterizing and evaluating pillars, domes versus pillars, and nanostructured samples, the dissertation next looked at the scalability of manufacturing a superhydrophobic surface for a full-scale coil. Since the individual fins were already integrated into a heat exchanger and so could not be embossed or altered to form morphological microstructures, it was decided that the ZnO nanostructures would be grown onto the aluminum and then silanized. A sweep for the ZnO hydrothermal growth synthesis was performed, looking at varying temperatures, solution concentrations, and growth times. The samples were then tested in the condensation testbed to compare their behavior. It was found that the 70 ℃ sample at 25 mM and 4.5-hour growth time had the best condensation and shedding performance. These conditions were used to coat a coil in a custom-designed synthesis setup. A second coil was coated with 70 ℃, 25 mM, and 1.5-hour growth time conditions based on the fabrication conditions used for growing ZnO nanostructures on the microdomes and micropillars.

8.2 Future Work

Future work for this project should aim to continue investigating and optimizing the patterns and processing for microstructure surface fabrication as well as testing those patterns. In addition, it would be valuable to perform tests on pure metal samples due to thermal conductivity. PDMS was used for ease of fabrication for multiple geometries but still presented some initial difficulties in condensation tests. In the surface characterization of the dome and pillar samples, heat transfer coefficients and overall heat flux values were never evaluated for comparison. Based on the literature review, it was accepted that dropwise condensation had better heat transfer performance than filmwise condensation. A full quantitative comparison of the heat transfer coefficients and heat flux of the specific structures here would have been illuminating in evaluating potential energy savings and performance improvements.

In addition, some preliminary wettability patterning experiments were performed but never fully investigated quantitatively. Wettability patterning, or patterning of surface energy for alternating hydrophobic and hydrophilic regions is a topic of great interest for controlling nucleation, condensation, and shedding events. Domes and pillars are purely morphological means of patterning, and it would have been interesting to perform the same types of static, dynamic, and condensation testing characterizations for patterned wettability surfaces.

Also, for the scaling project in particular, the future work is currently being planned and will be to take the coated coil and test its heat transfer performance in a full-scale testbed setup. Pressure drop, temperature change of the air and coolant, total heat flux, heat transfer coefficient, and relative humidity change across the coil are all values that will be evaluated to compare the coated coil's performance to that of a standard non-coated air conditioning coil.

Bibliography

[1] W. Goetzler, M. Guernsey, J. Young, J. Fujrman, A. Abdelaziz, *The Future of Air Conditioning for Buildings*, **2016**.
[2] T. Hoyt, E. Arens, H. Zhang, *Building and Environment* **2014**, DOI 10.1016/j.buildenv.2014.09.010.
[3] Lucas Davis, *Energy Institute Blog* **2015**.
[4] L. W. Davis, P. J. Gertler, *Proceedings of the National Academy of Sciences* **2015**, *112*, 5962.
[5] International Energy Agency, *IEA Newsroom* **2018**.
[6] W. Goetzler, *Energy Savings Potential and RD&D Opportunities for Commercial Building HVAC Systems*, U.S. Department of Energy Office of Energy Efficiency And Renewable Energy, **2017**.
[7] A. T. Paxson, Advanced Materials for Enhanced Condensation Heat Transfer, Thesis, Massachusetts Institute of Technology, **2014**.
[8] L. Yin, L. Zhu, Q. Wang, J. Ding, Q. Chen, *ACS Appl Mater Interfaces* **2011**, *3*, 1254.
[9] N. Miljkovic, E. N. Wang, *Nenad Miljkovic* **2013**.
[10] P. Olin, S. B. Lindström, T. Pettersson, L. Wågberg, *Langmuir* **2013**, *29*, 9079.
[11] A. Ghosh, S. Beaini, B. J. Zhang, R. Ganguly, C. M. Megaridis, *Langmuir* **2014**, *30*, 13103.
[12] B. Bhushan, Y. C. Jung, *Progress in Materials Science* **2011**, *56*, 1.
[13] H. Zhu, Z. Guo, W. Liu, *Chem. Commun.* **2016**, *52*, DOI 10.1039/C5CC09867J.
[14] M. Nosonovsky, *Langmuir* **2007**, *23*, 3157.
[15] R. Enright, N. Miljkovic, A. Al-Obeidi, C. V. Thompson, E. N. Wang, *Nenad Miljkovic* **2012**.
[16] R. Enright, N. Miljkovic, J. L. Alvarado, K. Kim, J. W. Rose, *Nanoscale and Microscale Thermophysical Engineering* **2014**, *18*, 223.
[17] Feng, L.; Li, S. H.; Li, Y. S.; Li, H. J.; Zhang, L. J.; Zhai, J.; Song, Y. L.; Liu, B. Q.; Jiang, L.; Zhu, D. B., *Advanced Materials* **2002**, *14*, 1857−1860.
[18] B. Bhushan, *Philosophical Transactions of the Royal Society of London A: Mathematical, Physical and Engineering Sciences* **2009**, *367*, 1445.
[19] Wang, Shutao, et al., *Chemical Reviews* **2015**, *115*, 8230.
[20] Autumn, K.; Sitti, M.; Liang, Y.C.A.; Peattie, A.M.; Hansen, W.R.; Sponberg, S.; Kenny, T.W.; Fearing, R.; Israelachvili, J. N.; Full, R. J., *Proc. Natl. Acad. Sci. U.S.A.* **2002**, *99*, 12252−12256.
[21] Gao, X. F.; Yan, X.; Yao, X.; Xu, L.; Zhang, K.; Zhang, J.H.; Yang, B.; Jiang, L., *Advanced Materials* **2007**, *19*, 2213−2217.
[22] J. Zhang, X. Sheng, L. Jiang, *Langmuir* **2009**, *25*, 1371.
[23] L. Feng, Y. Zhang, M. Li, Y. Zheng, W. Shen, L. Jiang, *Langmuir* **2010**, *26*, 14885.
[24] E. Celia, T. Darmanin, E. Taffin de Givenchy, S. Amigoni, F. Guittard, *Journal of Colloid and Interface Science* **2013**, *402*, 1.
[25] T. Young, *Phil. Trans. R. Soc. Lond.* **1805**, *95*, 65.
[26] S. Herminghaus, *EPL* **2000**, *52*, 165.
[27] J. C. Love, L. A. Estroff, J. K. Kriebel, R. G. Nuzzo, G. M. Whitesides, *Chem. Rev.* **2005**, *105*, 1103.
[28] S. Wang, K. Liu, X. Yao, L. Jiang, *Chem. Rev.* **2015**, *115*, 8230.
[29] J. W. J. Cheng, Hydrothermal Synthesis of Zinc Oxide Nanowire Arrays for Photovoltaic Applications, PhD, Massachusetts Institute of Technology, **2016**.

[30] O. E. Lopez, A. L. Tucker, K. R. Singh, S. B. Mamer, M. Sadoqi, H. Xu, *Superlattices and Microstructures* **2014**, *75*, 358.
[31] R. N. Wenzel, *Ind. Eng. Chem.* **1936**, *28*, 988.
[32] R. N. Wenzel, *J. Phys. Chem.* **1949**, *53*, 1466.
[33] A. B. D. Cassie, S. Baxter, *Trans. Faraday Soc.* **1944**, *40*, 546.
[34] D. Murakami, H. Jinnai, A. Takahara, *Langmuir* **2014**, *30*, 2061.
[35] P. Papadopoulos, L. Mammen, X. Deng, D. Vollmer, H.-J. Butt, *Proc Natl Acad Sci U S A* **2013**, *110*, 3254.
[36] K. K. Varanasi, M. Hsu, N. Bhate, W. Yang, T. Deng, *Applied Physics Letters* **2009**, *95*, 094101.
[37] N. Miljkovic, Development and Characterization of Micro/Nano Structured Surfaces for Enhanced Condensation, Thesis, Massachusetts Institute of Technology, **2013**.
[38] N. Miljkovic, R. Enright, J. Alvarado, K. Kwang, J. Rose, *Nenad Miljkovic* **2014**.
[39] K. K. Varanasi, T. Deng, M. F. Hsu, N. Bhate, *ResearchGate* **2008**, *13*, DOI 10.1115/IMECE2008-67808.
[40] K. K. Varanasi, T. Deng, M. Hsu, N. Bhate, *Hierarchical Superhydrophobic Surfaces Resist Water Droplet Impact*, Nano Science and Technology Institute, **2009**.
[41] B. Sobac, A. Rednikov, S. Dorbolo, P. Colinet, in *Droplet Wetting and Evaporation* (Ed.: D. Brutin), Academic Press, Oxford, **2015**, pp. 85–99.
[42] D. Brutin, B. Sobac, in *Droplet Wetting and Evaporation* (Ed.: D. Brutin), Academic Press, Oxford, **2015**, pp. 25–30.
[43] "Advancing angle," can be found under https://www.kruss-scientific.com/services/education-theory/glossary/advancing-angle/, **2018**.
[44] B. E. Rapp, in *Microfluidics: Modelling, Mechanics and Mathematics* (Ed.: B.E. Rapp), Elsevier, Oxford, **2017**, pp. 421–444.
[45] X. Yan, L. Zhang, S. Sett, L. Feng, C. Zhao, Z. Huang, H. Vahabi, A. K. Kota, F. Chen, N. Miljkovic, *ACS Nano* **2019**, DOI 10.1021/acsnano.8b06677.
[46] J. G. Buijnsters, R. Zhong, N. Tsyntsaru, J.-P. Celis, *ACS Appl. Mater. Interfaces* **2013**, *5*, 3224.
[47] M. Karlsson, P. Forsberg, F. Nikolajeff, *Langmuir* **2010**, *26*, 889.
[48] L. Feng, Y. Song, J. Zhai, B. Liu, J. Xu, L. Jiang, D. Zhu, *Angewandte Chemie International Edition* **2003**, *42*, 800.
[49] L. Cao, T. P. Price, M. Weiss, D. Gao, *Langmuir* **2008**, *24*, 1640.
[50] J. Wang, F. Liu, H. Chen, D. Chen, *Applied Physics Letters* **2009**, *95*, 084104.
[51] K. Koch, B. Bhushan, W. Barthlott, *Progress in Materials Science* **2009**, *54*, 137.
[52] K. Koch, B. Bhushan, W. Barthlott, *Soft Matter* **2008**, *4*, 1943.
[53] B. Bhushan, Y. C. Jung, K. Koch, *Philosophical Transactions of the Royal Society of London A: Mathematical, Physical and Engineering Sciences* **2009**, *367*, 1631.
[54] B. Bhushan, Y. Chae Jung, *Ultramicroscopy* **2007**, *107*, 1033.
[55] K. M. Smyth, A. T. Paxson, H. Kwon, T. Deng, K. K. Varanasi, *Dynamic Wetting on Superhydrophobic Surfaces: Droplet Impact and Wetting Hysteresis*, Institute of Electrical and Electronics Engineers, **2010**.
[56] L. Liu, A. M. Jacobi, D. Chvedov, *J. Micromech. Microeng.* **2009**, *19*, 035026.
[57] A. D. Sommers, A. M. Jacobi, *Using Anisotropic Micro-Scale Topography to Manipulate the Wettability of Aluminum and Reduce the Retention of Water*, Air Conditioning and Refrigeration Center. College of Engineering. University of Illinois At Urbana-Champaign., **2007**.
[58] A. D. Sommers, A. M. Jacobi, *J. Micromech. Microeng.* **2006**, *16*, 1571.

[59] S. S. Latthe, C. Terashima, K. Nakata, A. Fujishima, *Molecules* **2014**, *19*, 4256.
[60] N. Miljkovic, R. Enright, E. N. Wang, *Journal of Heat Transfer* **2013**, *135*, 111004.
[61] D. Seo, S. Oh, S. Shin, Y. Nam, *International Journal of Heat and Mass Transfer* **2017**, *114*, 934.
[62] J. Long, L. Pan, P. Fan, D. Gong, D. Jiang, H. Zhang, L. Li, M. Zhong, *Langmuir* **2016**, *32*, 1065.
[63] Z. Yoshimitsu, A. Nakajima, T. Watanabe, K. Hashimoto, *Langmuir* **2002**, *18*, 5818.
[64] F. Chen, D. Zhang, Q. Yang, J. Yong, G. Du, J. Si, F. Yun, X. Hou, *ACS Appl. Mater. Interfaces* **2013**, *5*, 6777.
[65] T. Sun, L. Feng, X. Gao, L. Jiang, *Acc. Chem. Res.* **2005**, *38*, 644.
[66] K. A. Wier, T. J. McCarthy, *Langmuir* **2006**, *22*, 2433.
[67] X. Wang, Md. A. Rahman, A. M. Jacobi, P. S. Hrnjak, *Heat Transfer Engineering* **2013**, *34*, 1088.
[68] Y. Wang, J. Xue, Q. Wang, Q. Chen, J. Ding, *ACS Appl. Mater. Interfaces* **2013**, *5*, 3370.
[69] M. Edalatpour, L. Liu, A. M. Jacobi, K. F. Eid, A. D. Sommers, *Applied Energy* **2018**, *222*, 967.
[70] K.-C. Park, P. Kim, A. Grinthal, N. He, D. Fox, J. C. Weaver, J. Aizenberg, *Nature* **2016**, *531*, 78.
[71] K. Kadala, S. Chung, H. Taylor, *Submission in review* **2019**.
[72] S. Zarei, H. R. Talesh Bahrami, H. Saffari, *Applied Thermal Engineering* **2018**, *137*, 440.
[73] L. Brockway, H. Taylor, *Materials Research Express* **2017**, *4*, 045003.
[74] Tiago Ferreira, Wayne Rasband, "ImageJ User Guide," can be found under https://imagej.nih.gov/ij/docs/guide/index.html, **2012**.
[75] L. Brockway, H. Taylor, *Materials Research Express* **2016**, *3*, 105039.
[76] A. Mohammad Karim, H. P. Kavehpour, *J Coat Technol Res* **2015**, *12*, 959.
[77] F. Zhu, J. Y. Jia, H. Z. Fu, Y. L. Chen, Z. Zeng, and D. L. Yu, *Mech. Sci.* **2015**, *6*, 211.
[78] J. W. van Honschoten, N. R. Tas, M. Elwenspoek, *American Journal of Physics* **2010**, *78*, 277.
[79] Plamen V.Petkov, Boryan P.Radoev, *Colloids and Surfaces A: Physicochemical and Engineering Aspects* **2014**, *460*, 18.
[80] L. Gao, T. J. McCarthy, *Langmuir* **2006**, *22*, 6234.
[81] R. H. Dettre, R. E. Johnson, *J. Phys. Chem.* **1965**, *69*, 1507.
[82] Rulon Johnson, Jr. and Robert H. Dettre, *The Journal of Physical Chemistry* **1963**.
[83] R. Tadmor, *Langmuir* **2004**, *20*, 7659.
[84] E. J. De Souza, L. Gao, T. J. McCarthy, E. Arzt, and A. J. Crosby, *Langmuir* **2008**, *24*, 1391.
[85] P.A. Kralchevsky and K. Nagayama, *Particles at Fluid Interfaces and Membranes*, Elsevier, Colloid Particles and Proteins to Interfaces and Formation of Two-Dimensional Arrays, **2001**.
[86] A. Mohammad Karim, J. P. Rothstein, H. P. Kavehpour, *Journal of Colloid and Interface Science* **2018**, *513*, 658.
[87] K. M. Smyth, *Superhydrophobic Surfaces* **n.d.**, 56.
[88] B. P. Radoev, P. V. Petkov, I. T. Ivanov, *Surface Energy* **2015**, DOI 10.5772/60684.
[89] C. W. Extrand, *Langmuir* **2002**, *18*, 7991.
[90] P. Bradshaw, R. C. Pankhurst, *Progress in Aerospace Sciences* **1964**, *5*, 1.
[91] W. T. L. Chow, M. Roth, *International Journal of Climatology* **2006**, *26*, 2243.
[92] P. Rajagopalan, W. Xuchao, L. Eang, *Energy and Buildings* **2009**, *41*, 1319.
[93] L. Pérez-Lombard, J. Ortiz, C. Pout, *Energy and Buildings* **2008**, *40*, 394.

[94] Gabriel Happle, Erik Wilhelm, Jimeno A. Fonseca, Arno Schlueter, *Energy Procedia* **2017**, *122*, 313.
[95] R. M. James Bell, *Joint Institute for Aeronautics and Acoustics* **1988**, 37.
[96] R. D. Mehta, P. Bradshaw, *The Aeronautical Journal* **1979**, *83*, 443.
[97] Marshall, Richard D, *National Bureau of Standards U.S. Department of Commerce* **1985**.
[98] Fluke Corporation, *How to Make a Duct Traversal Airflow Measurement*, **2007**.
[99] Engineering ToolBox, **2003**.
[100] Engineering ToolBox, **2004**.
[101] Engineering ToolBox, **2003**.
[102] Z. S. Spakovszky, *16.Unified: Thermodynamics and Propulsion*, **1993**.
[103] K. Rykaczewski, *Langmuir* **2012**, *28*, 7720.
[104] A. Tuteja, W. Choi, J. M. Mabry, G. H. McKinley, R. E. Cohen, *Proc. Natl. Acad. Sci. U.S.A.* **2008**, *105*, 18200.
[105] William C. Hinds, *Aerosol Technology: Properties, Behavior, and Measurement of Airborne Particles, 2nd Edition*, **1999**.
[106] William H. Brune, "Curvature Effect: Kelvin Effect," can be found under https://www.e-education.psu.edu/meteo300/node/676, **2018**.
[107] J. B. Boreyko, C.-H. Chen, *Phys. Rev. Lett.* **2009**, *103*, 184501.
[108] N. Miljkovic, R. Enright, Y. Nam, K. Lopez, N. Dou, J. Sack, E. N. Wang, *Nano Letters* **2013**, *13*, 179.
[109] C. Lv, P. Hao, Z. Yao, Y. Song, X. Zhang, F. He, *Appl. Phys. Lett.* **2013**, *103*, 14.
[110] H. Cha, C. Xu, J. Sotelo, J. M. Chun, Y. Yokoyama, R. Enright, N. Miljkovic, *Physical Review Fluids* **2016**, *1*, DOI 10.1103/PhysRevFluids.1.064102.
[111] N. Miljkovic, R. Enright, E. N. Wang, *ACS Nano* **2012**, *6*, 1776.
[112] K. L. Wilke, D. J. Preston, Z. Lu, E. N. Wang, *ACS Nano* **2018**, *12*, 11013.
[113] Mathworks, *MATLAB Documentation* **n.d.**
[114] Zuiderveld, Karel, *Graphic Gems IV. San Diego: Academic Press Professional* **1994**, 474.
[115] Mathworks, *MATLAB Documentation* **2006**.
[116] Steve Eddins, *Mathworks: Technical Articles and Newsletters* **2002**.
[117] A. Sommers, A. M. Jacobi, **2008**, 9.
[118] H. Jo, K. W. Hwang, D. Kim, M. Kiyofumi, H. S. Park, M. H. Kim, H. S. Ahn, *Scientific Reports* **2015**, *5*, 9901.
[119] Gelest Inc., **n.d.**
[120] Hitoshi Ogihara, *Langmuir* **2012**, *28*, 4605.